Numerical Solutions of Boundary Value Problems for Incompressible Internal Polar Viscous Fluids

By

Dipin Khadka

Submitted to the Department of Mechanical Engineering and the
Graduate Faculty of the University of Kansas
in partial fulfillment of the requirements for the degree of
Master of Science

Prof. Karan S. Surana, Chairperson

Committee members

Prof. Peter TenPas

Prof. Robert Sorem

Date defended: _____

The Thesis Committee for Dipin Khadka certifies
that this is the approved version of the following thesis :

Numerical Solutions of Boundary Value Problems for Incompressible Internal Polar Viscous Fluids

Prof. Karan S. Surana, Chairperson

Date approved: _____

Abstract

The work presented here considers conservation and balance laws and constitutive theories for internal polar non-classical isotropic, homogeneous incompressible thermofluids Surana et.al [1, 2] to present numerical studies and comparison with the results obtained using classical thermodynamic frame and standard constitutive theories.

The internal polar continuum theories are based on the fact that if the velocity gradient tensor is a fundamental measure of deformation physics in fluids then the thermodynamic framework for such fluids must incorporate the velocity gradient tensor in its entirety. Polar decomposition of the velocity gradient tensor into stretch rates and the rotation rates shows that only the stretch rates are incorporated in the currently used thermodynamic framework and the rotation rates are completely neglected. If the velocity gradient tensor varies from a material point to the neighboring material points, then so do the rates of rotations which, when resisted by the fluid result in conjugate moment tensor. Rates of rotations and conjugate moment tensor can result in additional resistance to fluid motion and additional dissipation i.e. entropy production. Due to the fact that the internal polar non-classical continuum theory incorporates internal rotations and conjugate moment tensor, the theory is called internal polar non-classical continuum theory.

The thermodynamic framework for internal polar thermofluids has been presented by Surana et.al [1,2]. The constitutive theory for internal polar incompressible thermofluids has also been presented by Surana et.al [2]. These are utilized in this work to present numerical studies for model problems. Boundary value problems consisting

of fully developed flow between parallel plates, square and rectangular lid driven cavities and asymmetric sudden expansion with three different expansion ratios are used as model problems. Numerical solutions are computed using least squares finite element processes based on residual functional in which p-version hierarchical local approximations are considered in $H^{k,p}(\overline{\Omega}^e)$ scalar product spaces that permit higher order global differentiability local approximations. Nonlinear algebraic equations resulting from the finite element formulation are solved using Newton's linear method with line search [3–6]. Numerical solutions obtained from internal polar mathematical models are compared with those obtained using classical continuum theory.

Acknowledgements

It is a great pleasure to express my heartiest regards and deepest sense of gratitude to my advisor, Dr. Karan Surana for his esteemed supervision, inspiring advice and enthusiastic encouragement during my time here. His willingness to give his valuable time has been genuinely appreciated. My thesis work could not have been accomplished without his proper guidance. My grateful thanks are also extended to Dr. Peter W. TenPas and Dr. Robert Sorem for serving on my committee.

Advice given by Dr. Peter W. TenPas has been a great help in my work. The financial support provided from Department of Mechanical Engineering is appreciated. I wish to thank all my colleagues in the Computational Mechanics program for their contributions in providing the valuable technical assistance and gave me support at critical junctures during the making to this research work.

Last but not the least, I would like to thank my family for their support and encouragement throughout my study.

Contents

List of Figures

List of Symbols

General (Eulerian Description)

$[\overline{D}]$: Symmetric part of velocity gradient tensor

$[^{\Theta}\overline{D}]$: Symmetric rotation rate gradient tensor

ER : Expansion Ratio

L_0 : Length in reference configuration

$\overline{m}$: Dimensionless moment tensor

m_0 : Moment tensor in reference configuration

$\overline{m}_{zx}$: Dimensionless moment tensor in $\overline{x}$-direction

$\overline{m}_{zy}$: Dimensionless moment tensor in $\overline{y}$-direction

$\overline{p}$: Dimensionless mechanical pressure

p_0 : Mechanical pressure in reference configuration

$\overline{Q}$: FLow rate

Re : Reynolds number

τ_0 : Stress in reference configuration

$\overline{u}$: Dimensionless velocity in $\overline{x}$-direction

u_0 : Velocity in reference configuration

$\overline{v}$: Dimensionless velocity in $\overline{y}$-direction

η : Dimensionless dynamic viscosity

η_0 : Dynamic viscosity in reference configuration

$^{m}\eta$: Dimensionless material coefficient

$\overline{\rho}$: Dimensionless density

ρ_0 : Density in reference configuration

$_{a}\overline{\sigma}_{yx}$: Antisymmetric shear stress

$_{d}(_{s}\overline{\sigma}_{yx})$: Deviatoric symmetric cauchy shear stress

$_{d}(\overline{\sigma}_{yx})$: Total shear stress

$_{d}(_{s}\overline{\sigma}_{xx})$: Deviatoric symmetric normal stress in x-direction

$_{d}(_{s}\overline{\sigma}_{yy})$: Deviatoric symmetric normal stress in y-direction

$^{t}\overline{\Theta}_{z}$: Rates of rotation

$\boldsymbol{I}$: Identity tensor

$\overline{\boldsymbol{m}}$: Cauchy moment tensor

$\overline{\boldsymbol{\sigma}}$: Cauchy stress tensor

$_{a}\overline{\boldsymbol{\sigma}}$: Antisymmetric part of cauchy stress tensor

$_{d}\overline{\boldsymbol{\sigma}}$: Deviatoric cauchy stress tensor

$_{e}\overline{\boldsymbol{\sigma}}$: Equilibrium cauchy stress tensor

$_{s}\overline{\boldsymbol{\sigma}}$: Symmetric part of cauchy stress tensor

Chapter 1

Introduction, Literature Review and Scope of Work

1.1 Introduction

The conservation and the balance laws for isotropic, homogeneous incompressible thermoviscous fluids are well establish [7]. Their derivation utilizes symmetric part of the velocity gradient tensor (i.e. stretch rates). The associated constitutive theories that provides closure to this mathematical model requires constitutive theory for Cauchy stress tensor and heat vector. Cauchy stress tensor is decomposed into equilibrium and deviatoric stress tensor. For incompressible thermoviscous fluids, the equilibrium stress tensor is mechanical pressure or Lagrange multiplier whereas for compressible fluids it is thermodynamic pressure as a function of density and temperature referred to as equation of state. The Newton's law of viscosity is often used as constitutive theory for deviatoric Cauchy stress tensor in which the Cauchy stress tensor is proportional to the symmetric part of velocity gradient tensor. For heat vector, the Fourier heat conduction law is used in which the heat vector is proportional to the temperature gradient. The constant of proportionality, the thermal conductivity can be a function of temperature, thus permitting power law, sutherland's law etc.

The classical thermodynamic framework based on classical continuum theories is currently used for incompressible fluids. A closer examination of the basis of derivation of this thermodynamic framework reveals that it only incorporates partial physics described by the velocity gradient tensor. The internal polar non-classical continuum theories and associated constitutive theories proposed by Surana et.al [1, 2, 8] for solid and fluent continua correct these weaknesses, hence provided more complete and consistent thermodynamic framework based on totality of Jacobian of deformation and velocity gradient tensors. Polar decomposition of velocity gradient tensor, a complete measure of deformation physics in fluids separate velocity gradient tensor into pure strain rates and rotation rates at a material point. The strain rates form the basis of current thermodynamic framework for fluids while the rotation rates are completely neglected. A simple observation shows that if the velocity gradient tensor varies between a material point and its neighbors then so does the rotation rate tensor. When the varying rotation rates between the material points are resisted by the fluid, they result in conjugate internal moment tensor, the Cauchy moment tensor. The rotation rates when resisted by fluid provide added resistance to fluid motion, hence may result in additional dissipation i.e. entropy production over and beyond that due to Cauchy stress tensor and the symmetric part of the velocity gradient tensor. A more complete thermodynamic framework must be based on velocity gradient tensor in its entirety i.e. stretch rate tensor as well as rotation rate tensor. The internal polar non-classical continuum theories accomplish this, hence provide a more consistent and more complete thermodynamic framework. The thermodynamic framework and the constitutive theories related to internal polar non-classical continuum theory obviously are different than the classical continuum framework for fluids. Details of the conservation and the balance laws and the constitutive theories are presented by Surana et.al [1, 2, 8].

1.2 Literature Review

For complete literature review of stress couple theories, micropolar theories, strain gradient theories etc. the readers can refer to the literature cited by Surana et.al [1,2,8]. It is now well estab-

lished that the internal polar non-classical continuum theories are initiated to correct a fundamental deficiency of ignoring the rotation rate tensor in the currently used theories in the derivation of the conservation and the balance laws and the associated constitutive theories; whereas the published works on the stress couple theories, micropolar theories, strain gradient theories etc are initiated with an assumption of "what if". The authors (Surana et.al [1,2,8]) have shown that these theories are not internal polar theories even though some expressions in the conservation and balance laws associated with these theories may have some resemblance.

Just like the classical continuum theories for fluids, the internal polar non-classical continuum theories for fluids also result in mathematical models that contain nonlinear partial differential equations. Finite difference, finite volume and finite element techniques have been used for obtaining their approximate numerical solutions [3,9,10]. Discussion of the details of various approaches within these method is not considered here. Interested reader can consult references [3, 9, 10]. Instead here we only describe some pertinent aspects of the computational technique used in the present work. Surana et.al [1, 2, 8] have shown that variationally consistent integral forms are essential for unconditional stability of the resulting computational process from the integral form. For nonlinear differential operator resulting from the mathematical models containing nonlinear partial differential equations only the least squares process derived using residual functional yields integral form that is variationally consistent. In the present work we use this method. Galerkin method with weak form and associated techniques such as SUPG DC/LS [11] and other approximation methods are precluded as viable approaches as all of these result in variationally inconsistent integral forms. Surana et.al [1, 2, 8] have shown that the order of approximation space k is an independent parameter in addition to h and p in all finite element computational process. Thus higher order Hilbert space $H^{k,p}(\overline{\Omega}^e)$ are meritorious for local approximations. Higher values of k permit higher order global differentiability local approximations which in term allow us to incorporate desired physics in the computational process. Thus, in the present work we use least squares finite element processes based on residual functional in which the local approximations are in $H^{k,p}(\overline{\Omega}^e)$ scalar product spaces. The nonlinear system of equations are solved using Newton's

linear method with line search.

1.3 Scope of Work

The purpose of the work contained here is to perform computational studies using mathematical models for the internal polar non-classical continuum physics [1, 2] for incompressible thermoviscous fluids using least squares finite element processes based on residual functional with local approximations in $H^{k,p}(\overline{\Omega}^e)$ spaces and compare these with the results obtained using the mathematical models based on classical continuum theory. The intent is to study the influence of new physics due to rotation rate in various applications.

Fully developed flow between parallel plates, square and rectangular lid driven cavities, and asymmetric sudden expansion with different expansion ratios are used as model problems.

Chapter 2

Mathematical Models

2.1 Introductions

In this chapter the mathematical models for internal polar non-classical incompressible viscous fluids (See Surana et.al [1,2]) and for classical incompressible viscous fluids are presented in $\mathbb{R}^2$. A simplified form of those models applicable to fully developed flow between parallel plates are also given. The mathematical models are non-dimensionalized using appropriate reference quantities. The dimensionless forms of the mathematical models are utilized to construct least squares finite element formulation for three model problems (boundary value problems) considered in the present work.

2.2 Mathematical model for internal polar incompressible viscous fluid in $\mathbb{R}^2$

Following Surana et.al [1, 2] we can write the following for complete mathematical model for such fluids in $\mathbb{R}^2$ in terms of velocities, mechanical pressure, deviatoric Cauchy stress tensor, deviatoric moment tensor, symmetric part of the velocity gradients and the symmetric part of the rotation rate gradient tensor. The over bar ($\bar{}$) signifies that the mathematical model is in Eulerian

description and hat (ˆ) indicates that all quantities have their usual dimensions.

$$\hat{\rho}\left(\frac{\partial\hat{\bar{u}}}{\partial\hat{\bar{x}}}+\frac{\partial\hat{\bar{v}}}{\partial\hat{\bar{y}}}\right)=0 \tag{2.1}$$

$$\left.\begin{aligned}\hat{\rho}\left(\hat{\bar{u}}\frac{\partial\hat{\bar{u}}}{\partial\hat{\bar{x}}}+\hat{\bar{v}}\frac{\partial\hat{\bar{u}}}{\partial\hat{\bar{y}}}\right)+\frac{\partial\hat{\bar{p}}}{\partial\hat{\bar{x}}}-\left(\frac{\partial({}_d({}_s\hat{\bar{\sigma}}_{xx}))}{\partial\hat{\bar{x}}}+\frac{\partial({}_d({}_s\hat{\bar{\sigma}}_{yx}))}{\partial\hat{\bar{y}}}+\frac{\partial({}_a\hat{\bar{\sigma}}_{yx})}{\partial\hat{\bar{y}}}\right)=0\\ \hat{\rho}\left(\hat{\bar{u}}\frac{\partial\hat{\bar{v}}}{\partial\hat{\bar{x}}}+\hat{\bar{v}}\frac{\partial\hat{\bar{v}}}{\partial\hat{\bar{y}}}\right)+\frac{\partial\hat{\bar{p}}}{\partial\hat{\bar{y}}}-\left(\frac{\partial({}_d({}_s\hat{\bar{\sigma}}_{yx}))}{\partial\hat{\bar{x}}}+\frac{\partial({}_d({}_s\hat{\bar{\sigma}}_{yy}))}{\partial\hat{\bar{y}}}-\frac{\partial({}_a\hat{\bar{\sigma}}_{yx})}{\partial\hat{\bar{x}}}\right)=0\end{aligned}\right\} \tag{2.2}$$

$$\frac{\partial\hat{\bar{m}}_{zx}}{\partial\hat{\bar{x}}}+\frac{\partial\hat{\bar{m}}_{zy}}{\partial\hat{\bar{y}}}+2({}_a\hat{\bar{\sigma}}_{yx})=0 \tag{2.3}$$

$$\in:\overline{\boldsymbol{m}}=0 \tag{2.4}$$

$$\left.\begin{aligned}{}_d({}_s\hat{\bar{\sigma}}_{xx})&=2\hat{\eta}|_{\underline{\Omega}}\left(\frac{\partial\hat{\bar{u}}}{\partial\hat{\bar{x}}}\right)\\ {}_d({}_s\hat{\bar{\sigma}}_{yy})&=2\hat{\eta}|_{\underline{\Omega}}\left(\frac{\partial\hat{\bar{v}}}{\partial\hat{\bar{y}}}\right)\\ {}_d({}_s\hat{\bar{\sigma}}_{yx})&=\hat{\eta}|_{\underline{\Omega}}\left(\frac{\partial\hat{\bar{u}}}{\partial\hat{\bar{y}}}+\frac{\partial\hat{\bar{v}}}{\partial\hat{\bar{x}}}\right)\end{aligned}\right\} \tag{2.5}$$

$$\left.\begin{aligned}\hat{\bar{m}}_{zx}&={}^m\hat{\eta}|_{\underline{\Omega}}\left(\frac{\partial{}^t\hat{\bar{\Theta}}_z}{\partial\hat{\bar{x}}}\right)\\ \hat{\bar{m}}_{zy}&={}^m\hat{\eta}|_{\underline{\Omega}}\left(\frac{\partial{}^t\hat{\bar{\Theta}}_z}{\partial\hat{\bar{y}}}\right)\end{aligned}\right\} \tag{2.6}$$

$${}^t\hat{\bar{\Theta}}_z=\frac{1}{2}\left(\frac{\partial\hat{\bar{u}}}{\partial\hat{\bar{y}}}-\frac{\partial\hat{\bar{v}}}{\partial\hat{\bar{x}}}\right) \tag{2.7}$$

Equation (2.1) is continuity equation due to conservation of mass, equations (2.2) are balance of linear momenta, equation (2.3) is due to balance of angular momenta, equation (2.4) defines additional balance law, balance of moment of moments, equations (2.5) are constitutive theory for the symmetric part of the deviatoric Cauchy stress tensor, equations (2.6) are the constitutive theories for Cauchy moment tensor and equation (2.7) defines the only nonzero rate of rotation. The non-symmetric stress tensor has been decomposed into symmetric and skew symmetric stress

tensors.

$$\overline{\boldsymbol{\sigma}} = {}_s\overline{\boldsymbol{\sigma}} + {}_a\overline{\boldsymbol{\sigma}} \tag{2.8}$$

Symmetric stress tensor ${}_s\overline{\boldsymbol{\sigma}}$ is decomposed into equilibrium stress tensor ${}_e\overline{\boldsymbol{\sigma}}$ and the deviatoric Cauchy stress tensor, ${}_d\overline{\boldsymbol{\sigma}}$.

$${}_s\overline{\boldsymbol{\sigma}} = {}_e\overline{\boldsymbol{\sigma}} + {}_d\overline{\boldsymbol{\sigma}} \tag{2.9}$$

Furthermore, ${}_e\overline{\boldsymbol{\sigma}} = -p\boldsymbol{I}$ ([7]) for incompressible fluid in which compressive p is positive.

Equations (2.1)-(2.7) are ten partial differential equations in ten variables: $\hat{\bar{u}},\ \hat{\bar{v}},\ \hat{\bar{p}},\ {}_d({}_s\hat{\bar{\sigma}}_{xx}),$ ${}_d({}_s\hat{\bar{\sigma}}_{yy}),\ {}_d({}_s\hat{\bar{\sigma}}_{yx}),\ ({}_a\hat{\bar{\sigma}}_{yx}),\ \hat{\bar{m}}_{zx},\ \hat{\bar{m}}_{zy},\ ({}^t\hat{\bar{\Theta}}_z)$, hence this mathematical model has closure. We choose following reference and dimensionless quantities

$$\begin{gathered}
\bar{x} = \frac{\hat{\bar{x}}}{L_0} \quad , \quad \bar{y} = \frac{\hat{\bar{y}}}{L_0} \quad , \quad \eta = \frac{\hat{\eta}|_{\Omega}}{\eta_0} \quad , \quad \overline{p} = \frac{\hat{\bar{p}}}{p_0} \quad , \quad {}^m\eta = \frac{{}^m\hat{\eta}|_{\Omega}}{\eta_0} \quad , \\
{}_d({}_s\overline{\sigma}_{ij}) = \frac{{}_d({}_s\hat{\bar{\sigma}}_{ij})}{\tau_0}; \quad i = 1,2 \quad j = 1,2 \quad , \\
({}_a\overline{\sigma}_{yx}) = \frac{({}_a\hat{\bar{\sigma}}_{yx})}{\tau_0} \quad , \quad \overline{\rho} = \frac{\hat{\bar{\rho}}}{\rho_0} \quad , \quad m_0 = \tau_0 L_0
\end{gathered} \tag{2.10}$$

in which $L_0,\ \rho_0,\ u_0,\ \tau_0,\ \eta_0,\ p_0$, are reference length, density, velocity, stress, viscosity and mechanical pressure, we choose $p_0 = \tau_0 = \rho_0 u_0^2$ (characteristic kinetic energy). Using (2.10) in (2.1)-(2.7) we obtain the following dimensionless mathematical model.

$$\overline{\rho}\left(\frac{\partial \overline{u}}{\partial \bar{x}} + \frac{\partial \overline{v}}{\partial \bar{y}}\right) = 0 \tag{2.11}$$

$$\left.\begin{aligned}
\overline{\rho}\left(\overline{u}\frac{\partial \overline{u}}{\partial \bar{x}} + \overline{v}\frac{\partial \overline{u}}{\partial \bar{y}}\right) + \frac{\partial \overline{p}}{\partial \bar{x}} - \left(\frac{\partial({}_d({}_s\overline{\sigma}_{xx}))}{\partial \bar{x}} + \frac{\partial({}_d({}_s\overline{\sigma}_{yx}))}{\partial \bar{y}} + \frac{\partial({}_a\overline{\sigma}_{yx})}{\partial \bar{y}}\right) = 0 \\
\overline{\rho}\left(\overline{u}\frac{\partial \overline{v}}{\partial \bar{x}} + \overline{v}\frac{\partial \overline{v}}{\partial \bar{y}}\right) + \frac{\partial \overline{p}}{\partial \bar{y}} - \left(\frac{\partial({}_d({}_s\overline{\sigma}_{yx}))}{\partial \bar{x}} + \frac{\partial({}_d({}_s\overline{\sigma}_{yy}))}{\partial \bar{y}} - \frac{\partial({}_a\overline{\sigma}_{yx})}{\partial \bar{x}}\right) = 0
\end{aligned}\right\} \tag{2.12}$$

$$\frac{\partial \overline{m}_{zx}}{\partial \bar{x}} + \frac{\partial \overline{m}_{zy}}{\partial \bar{y}} + 2({}_a\overline{\sigma}_{yx}) = 0 \tag{2.13}$$

$$\in : \overline{\boldsymbol{m}} = 0 \tag{2.14}$$

$$\left.\begin{aligned} {}_d({}_s\overline{\sigma}_{xx}) &= \frac{1}{Re}2\eta\left(\frac{\partial\overline{u}}{\partial\overline{x}}\right) \\ {}_d({}_s\overline{\sigma}_{yy}) &= \frac{1}{Re}2\eta\left(\frac{\partial\overline{v}}{\partial\overline{y}}\right) \\ {}_d({}_s\overline{\sigma}_{yx}) &= \frac{1}{Re}\eta\left(\frac{\partial\overline{u}}{\partial\overline{y}}+\frac{\partial\overline{v}}{\partial\overline{x}}\right) \end{aligned}\right\} \tag{2.15}$$

$$\left.\begin{aligned} \overline{m}_{zx} &= \frac{1}{ReL_0^2}{}^m\eta\left(\frac{\partial{}^t\overline{\Theta}_z}{\partial\overline{x}}\right) \\ \overline{m}_{zy} &= \frac{1}{ReL_0^2}{}^m\eta\left(\frac{\partial{}^t\overline{\Theta}_z}{\partial\overline{y}}\right) \end{aligned}\right\} \tag{2.16}$$

$${}^t\overline{\Theta}_z = \frac{1}{2}\left(\frac{\partial\overline{u}}{\partial\overline{y}}-\frac{\partial\overline{v}}{\partial\overline{x}}\right) \tag{2.17}$$

$$Re = \frac{\rho_0 L_0 u_0}{\eta_0} \tag{2.18}$$

Complete mathematical model for internal polar non-classical continuum theory described by (2.11)-(2.17) is used for computing numerical solutions.

2.3 Mathematical model for incompressible viscous fluid in $\mathbb{R}^2$ based on classical continuum theory

This mathematical model consists of standard Navier-Stokes equations [7]. Their dimensionless form can be written as (in the absence of body forces)

$$\overline{\rho}\left(\frac{\partial\overline{u}}{\partial\overline{x}}+\frac{\partial\overline{v}}{\partial\overline{y}}\right)=0 \tag{2.19}$$

$$\left.\begin{aligned} \overline{\rho}\left(\overline{u}\frac{\partial\overline{u}}{\partial\overline{x}}+\overline{v}\frac{\partial\overline{u}}{\partial\overline{y}}\right)+\frac{\partial\overline{p}}{\partial\overline{x}}-\left(\frac{\partial({}_d\overline{\sigma}_{xx})}{\partial\overline{x}}+\frac{\partial({}_d\overline{\sigma}_{yx})}{\partial\overline{y}}\right)=0 \\ \overline{\rho}\left(\overline{u}\frac{\partial\overline{v}}{\partial\overline{x}}+\overline{v}\frac{\partial\overline{v}}{\partial\overline{y}}\right)+\frac{\partial\overline{p}}{\partial\overline{y}}-\left(\frac{\partial({}_d\overline{\sigma}_{yx})}{\partial\overline{x}}+\frac{\partial({}_d\overline{\sigma}_{yy})}{\partial\overline{y}}\right)=0 \end{aligned}\right\} \tag{2.20}$$

$$\in:\overline{\boldsymbol{\sigma}}=0 \tag{2.21}$$

$$
\left.
\begin{aligned}
{}_d\overline{\sigma}_{xx} &= \frac{1}{Re} 2\eta \left(\frac{\partial \overline{u}}{\partial \overline{x}} \right) \\
{}_d\overline{\sigma}_{yy} &= \frac{1}{Re} 2\eta \left(\frac{\partial \overline{v}}{\partial \overline{y}} \right) \\
{}_d\overline{\sigma}_{yx} &= \frac{1}{Re} \eta \left(\frac{\partial \overline{u}}{\partial \overline{y}} + \frac{\partial \overline{v}}{\partial \overline{x}} \right)
\end{aligned}
\right\} \tag{2.22}
$$

Equation (2.19) is continuity equation, (2.20) are due to balance of linear momenta and equation (2.21) is due to balance of angular momenta which implies that Cauchy stress tensor $\overline{\boldsymbol{\sigma}}$ is symmetric and equations (2.22) are constitutive theory for deviatoric Cauchy stress tensor. In (2.19) - (2.22), the stress decomposition

$$
\overline{\boldsymbol{\sigma}} = {}_e\overline{\boldsymbol{\sigma}} + {}_d\overline{\boldsymbol{\sigma}} \tag{2.23}
$$

has been used in which ${}_e\overline{\boldsymbol{\sigma}}$ and ${}_d\overline{\boldsymbol{\sigma}}$ are equilibrium and deviatoric stress tensors. The constitutive theory for equilibrium stress tensor for compressible fluid is given by

$$
{}_e\overline{\boldsymbol{\sigma}} = -p\boldsymbol{I} \tag{2.24}
$$

in which p is mechanical pressure (assumed positive when compressive).

2.4 Mathematical model for internal polar incompressible viscous fluid in $\mathbb{R}^1$

For fully developed flow between parallel plates we assume $\bar{x}$ as the direction of flow and the origin of $\bar{x}\,\bar{y}$ coordinate system at the bottom of the plate and $\bar{z}$ normal to $\bar{x}\,\bar{y}$ plane. This model can be easily deduced from the mathematical model in $\mathbb{R}^2$

$$
\frac{\partial ({}_d({}_s\hat{\overline{\sigma}}_{yx}))}{\partial \hat{\bar{y}}} + \frac{\partial ({}_a\hat{\overline{\sigma}}_{yx})}{\partial \hat{\bar{y}}} - \frac{\partial \hat{\overline{p}}}{\partial \hat{\bar{x}}} = 0 \tag{2.25}
$$

$$\frac{\partial \hat{\overline{m}}_{zy}}{\partial \hat{\bar{y}}} + 2({}_a\hat{\overline{\sigma}}_{yx}) = 0 \tag{2.26}$$

$${}_d({}_s\hat{\overline{\sigma}}_{yx}) = \hat{\eta}|_{\underline{\Omega}} \frac{\partial \hat{\bar{u}}}{\partial \hat{\bar{y}}} \tag{2.27}$$

$$\hat{\overline{m}}_{zy} = 2^m\hat{\eta}|_{\underline{\Omega}}({}^t\hat{\overline{\Theta}}_{z,y}) \tag{2.28}$$

$$({}^t\hat{\overline{\Theta}}_{z,y}) = \frac{\partial^2 \hat{\bar{u}}}{\partial \hat{\bar{y}}^2} \tag{2.29}$$

Dimensionless form of (2.25)-(2.29) can be obtained using the following reference quantities and the dimensionless variables

$$\begin{gathered} \bar{y} = \frac{\hat{\bar{y}}}{L_0} \quad , \quad \eta = \frac{\hat{\eta}|_{\underline{\Omega}}}{\eta_0} \quad , \quad {}^m\eta = \frac{{}^m\hat{\eta}|_{\underline{\Omega}}}{\eta_0} \quad , \quad \overline{p} = \frac{\hat{\bar{p}}}{p_0} \quad , \quad {}_d({}_s\hat{\overline{\sigma}}_{yx}) = \frac{{}_d({}_s\hat{\overline{\sigma}}_{yx})}{\tau_0} \\ ({}_a\hat{\overline{\sigma}}_{yx}) = \frac{({}_a\hat{\overline{\sigma}}_{yx})}{\tau_0} \quad , \quad \overline{u} = \frac{\hat{\bar{u}}}{u_0} \quad , \quad \overline{\overline{m}}_{zy} = \frac{\hat{\overline{m}}_{zy}}{m_0} \end{gathered} \tag{2.30}$$

Using (2.30) we can obtain the following dimensionless equations

$$\frac{\partial({}_d({}_s\overline{\sigma}_{yx}))}{\partial \bar{y}} + \frac{\partial({}_a\overline{\sigma}_{yx})}{\partial \bar{y}} - \left(\frac{p_0}{\tau_0}\right)\frac{\partial \overline{p}}{\partial \bar{x}} = 0 \tag{2.31}$$

$$\frac{\partial \overline{m}_{zy}}{\partial \bar{y}} + \left(\frac{\tau_0 L_0}{m_0}\right) 2({}_a\overline{\sigma}_{yx}) = 0 \tag{2.32}$$

$${}_d({}_s\overline{\sigma}_{yx}) = \eta\left(\frac{\eta_0 u_0}{L_0\tau_0}\right)\left(\frac{\partial \overline{u}}{\partial \bar{y}}\right) \tag{2.33}$$

$$\overline{m}_{zy} = \frac{1}{2}{}^m\eta\left(\frac{\eta_0 u_0}{m_0 L_0^2}\right)\left(\frac{\partial^2 \overline{u}}{\partial \bar{y}^2}\right) \tag{2.34}$$

We choose physical quantities and reference quantities in such a way that all multipliers appearing in (2.31)-(2.34) due to non-dimensionalization become unity. These dimensionless form of the equations are sufficient to compare the solutions with and without internal polar physics.

Thus equations (2.31)-(2.34) reduces to

$$\frac{\partial({}_d({}_s\overline{\sigma}_{yx}))}{\partial\overline{y}} + \frac{\partial({}_a\overline{\sigma}_{yx})}{\partial\overline{y}} - \frac{\partial\overline{p}}{\partial\overline{x}} = 0 \tag{2.35}$$

$$\frac{\partial\overline{m}_{zy}}{\partial\overline{y}} + 2({}_a\overline{\sigma}_{yx}) = 0 \tag{2.36}$$

$${}_d({}_s\overline{\sigma}_{yx}) = \eta\left(\frac{\partial\overline{u}}{\partial\overline{y}}\right) \tag{2.37}$$

$$\overline{m}_{zy} = \frac{1}{2}{}^m\eta\left(\frac{\partial^2\overline{u}}{\partial\overline{y}^2}\right) \tag{2.38}$$

The first material coefficient η is dimensionless viscosity and has a value of one. The second material coefficient ${}^m\eta$ (dimensionless) appearing in the constitutive theory for Cauchy moment tensor is due to internal polar physics. For incompressible viscous fluid, we have the following mathematical model based on classical continuum theory for fully developed flow between parallel plates

$$\frac{\partial({}_d({}_s\overline{\sigma}_{yx}))}{\partial\overline{y}} - \frac{\partial\overline{p}}{\partial\overline{x}} = 0 \tag{2.39}$$

$${}_d({}_s\overline{\sigma}_{yx}) = \eta\left(\frac{\partial\overline{u}}{\partial\overline{y}}\right) \tag{2.40}$$

Chapter 3

Numerical Studies

3.1 Introduction

In this chapter we consider boundary value problems: fully developed flow between parallel plates, square and rectangular lid driven cavities, and asymmetric sudden expansion with expansion ratios of $2.75:2$, $3:2$, and $3.5:2$ and obtain numerical solutions of the mathematical models associated with internal polar non-classical incompressible viscous fluid and also the models obtained using classical continuum theory for incompressible viscous fluids. Finite element formulations of the nonlinear partial differential equations in the mathematical models are constructed using least squares finite element formulation based on residual functional. Surana et.al [1, 2, 8] have shown the resulting finite element formulations to be variationally consistent, thus resulting in unconditionally stable computational processes. The local approximations are considered in higher order scalar product Hilbert spaces $H^{k,p}(\overline{\Omega}^e)$. By choosing order k of the space (Surana et.al [1, 2, 8]), the global differentiability of the approximation can be controlled. When k is minimally conforming [1–3, 8] the integrals over $\overline{\Omega}^T$, discretization of domain $\overline{\Omega}$ of the BVP in the entire computation process can be maintained in Riemann sense. The importance of this aspect is that we can judge how accurately the partial differential equations in the mathematical model are satisfied.

3.2 Model problem I : Fully developed flow between parallel plates

We consider fully developed flow between parallel plates of internal polar non-classical incompressible viscous fluid (${}^m\eta \neq 0$) as well as classical incompressible viscous fluid (${}^m\eta = 0$). Figure 3.1 shows a schematic of the flow between parallel plates. The spatial domain $0 \leq \bar{y} \leq 2$ is discretized using six three node p-version $C^i(\overline{\Omega}_y^e)$ higher order continuity elements [3, 4, 12–17]. Numerical results are computed for uniform p-level of 9 with k equal to 2 i.e. using the local approximations of class $C^1(\overline{\Omega}_y^e)$. The finite element formulation used is least square method based on the residual functional. For these choices of h, p, and k the integrated sum of squares of the residual is $0(10^{-22})$ or lower confirming that the GDEs are satisfied accurately.

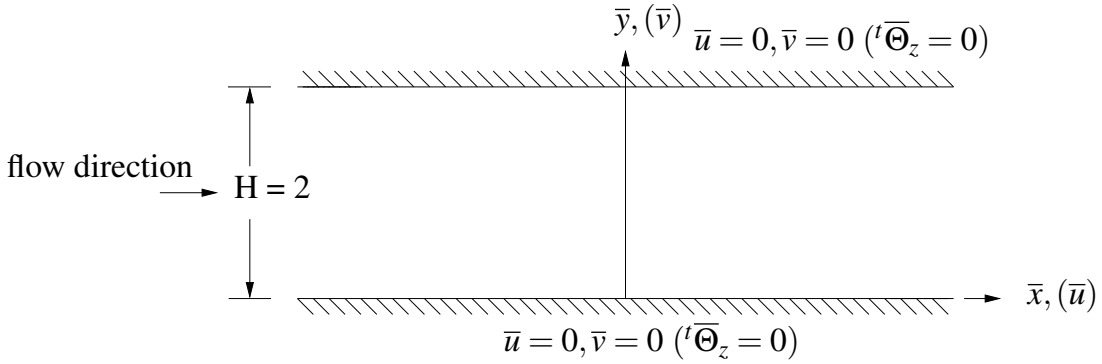

Figure 3.1: Schematic of fully developed flow of an incompressible internal polar viscous fluid

In all numerical calculations η = 1 (dimensionless Newtonian viscosity) and the dimensionless parameter ${}^m\eta$ controlling the influence of rotation rate and its gradients are varied from $0 \leq {}^m\eta \leq 2$. For ${}^m\eta$ = 0, we have purely Newtonian behavior. For progressively increasing values of ${}^m\eta$ (keeping η = 1) the fluid behavior progressively deviates from Newtonian behavior. The numerical solutions are computed for ${}^m\eta$ = 0.1, 0.25, 0.5, 1.0 and 2.0. All computations are performed for fixed $\dfrac{\partial \overline{p}}{\partial \overline{x}}$ = – 0.1 while ${}^m\eta$ is varied.

We consider the following properties and the reference quantities

$$\hat{\overline{\rho}} = 1\ kg/m^3 \quad , \quad \hat{\eta} = 1 \times 10^{-3}\ Pa$$

$$\rho_0 = 1\ kg/m^3 \quad , \quad \eta_0 = 1 \times 10^{-3}\ Pa$$

$$L_0 = 1\ m \quad , \quad u_0 = 1\ m/s$$

which results in

$$\overline{\rho} = 1 \quad , \quad \eta = 1 \quad , \quad Re = \frac{\rho_0 L_0 u_0}{\eta_0} = 1$$

Graphs of axial velocity $\overline{u}$, deviatoric symmetric Cauchy stress ${}_d({}_s\overline{\sigma}_{yx})$, antisymmetric stress ${}_a\overline{\sigma}_{yx}$, total stress $\overline{\sigma}_{yx}$ versus distance $\overline{y}$ are shown in figures 3.2 - 3.5 for chosen values of ${}^m\eta$. Plots of Cauchy moment tensor component and $\dfrac{\partial^2\overline{u}}{\partial\overline{y}^2}$ versus distance $\overline{y}$ are shown in figures 3.6-3.7 for different values of ${}^m\eta$. Figure 3.8 shows a plot of flow rate $\overline{Q} = \int_0^2 \overline{u}(\overline{y})d\overline{y}$ (for unit depth perpendicular to the plane of the paper) as a function of ${}^m\eta$. From the velocity graphs in figure 3.2 we observe that for progressively increasing values of ${}^m\eta$ results in progressively increasing resistance to flow due to progressively increasing rates of rotation gradients, hence the peak velocity value at the center of the flow domain diminishes with corresponding reduction in the axial velocity in the remaining flow domain. We observe that for ${}^m\eta$ values larger than 2.0 it is possible to completely choke the flow. This behavior exists regardless of the value of $\dfrac{\partial\overline{p}}{\partial\overline{x}}$. For ${}^m\eta = 0.0$, ${}_d({}_s\overline{\sigma}_{yx})$ is a linear function of $\overline{y}$ (figure 3.3) while ${}_a\overline{\sigma}_{yx}$ is exactly zero in the entire domain (figure 3.4) as they should be for Newtonian fluids. On the other hand for ${}^m\eta = 2.0$, ${}_a\overline{\sigma}_{yx}$ is close to being a linear function of $\overline{y}$ while ${}_d({}_s\overline{\sigma}_{yx})$ approaches zero (figures 3.3, 3.4). For this case the rate of rotation gradient behavior is the dominant physics. As expected $\overline{\sigma}_{yx}$ (figure 3.5) remains to be a linear function of $\overline{y}$ regardless of ${}^m\eta$ value as seen from the balance of linear momentum in $\overline{x}$ - direction. Plots of moment $\overline{m}_{zy}$ versus $\overline{y}$ in figure 3.6 show progressively increasing magnitude of Cauchy moment $\overline{m}_{zy}$ with progressively increasing ${}^m\eta$ whereas rate of rotation gradient $\dfrac{\partial^2\overline{u}}{\partial\overline{y}^2}$ decreases with progressively increasing ${}^m\eta$ due to increased resistance offered by the fluid (figure 3.7). Progressively reducing flow rate for progressively increasing values of ${}^m\eta$ due to progressively increasing resistance offered by the fluid in figure 3.8 are in agreement with the results presented in figure 3.2 and

others.

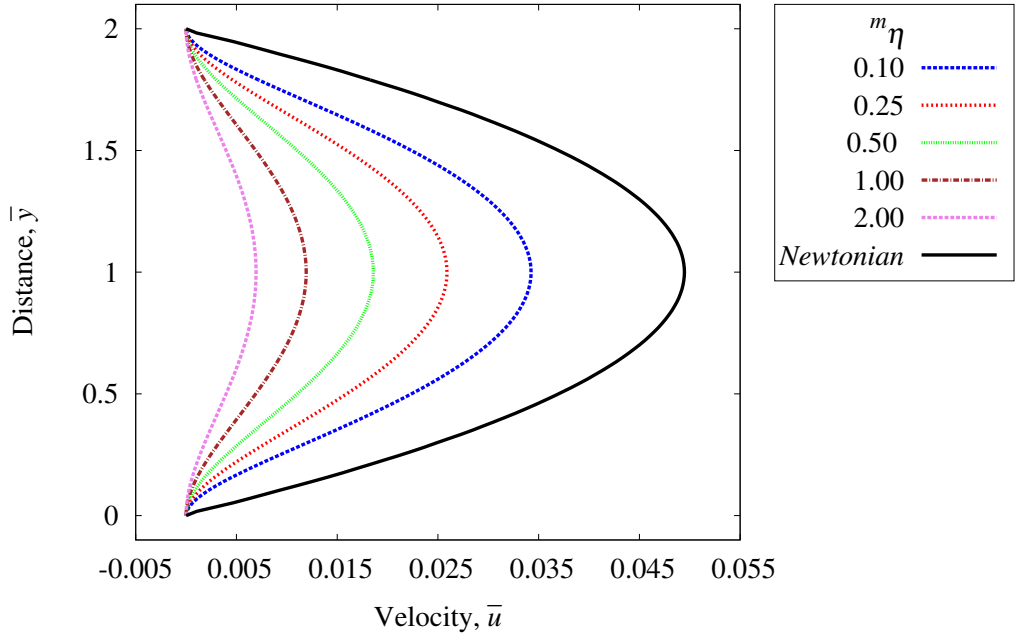

Figure 3.2: Axial velocity $\overline{u}$ versus distance $\overline{y}$

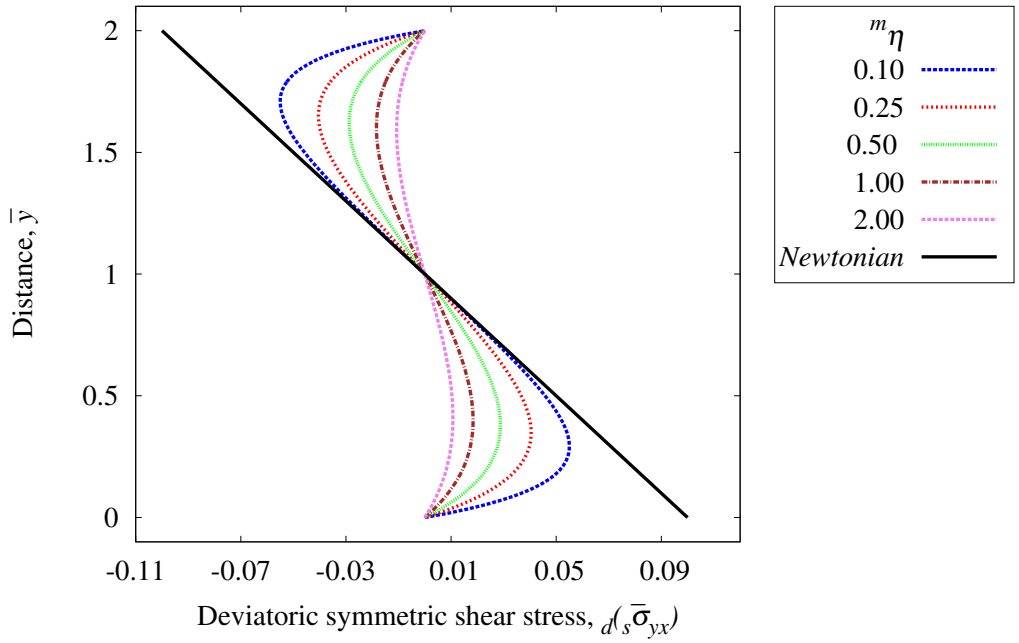

Figure 3.3: Deviatoric part of symmetric shear stress $_{d}(_{s}\overline{\sigma}_{yx})$ versus distance $\overline{y}$

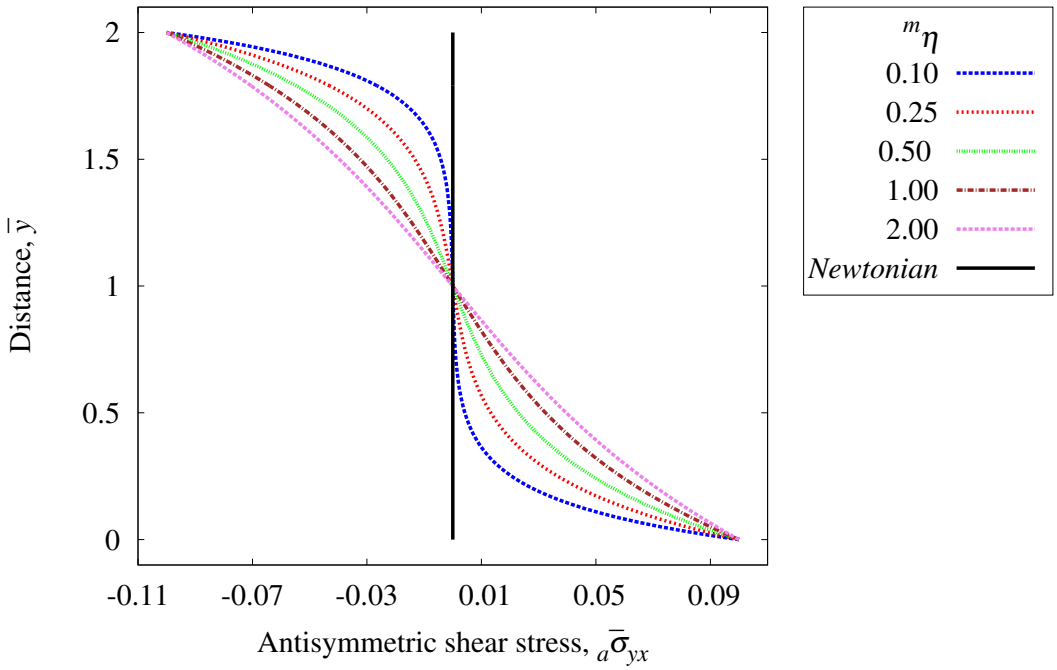

Figure 3.4: Antisymmetric shear stress ${}_a\bar{\sigma}_{yx}$ versus distance $\bar{y}$

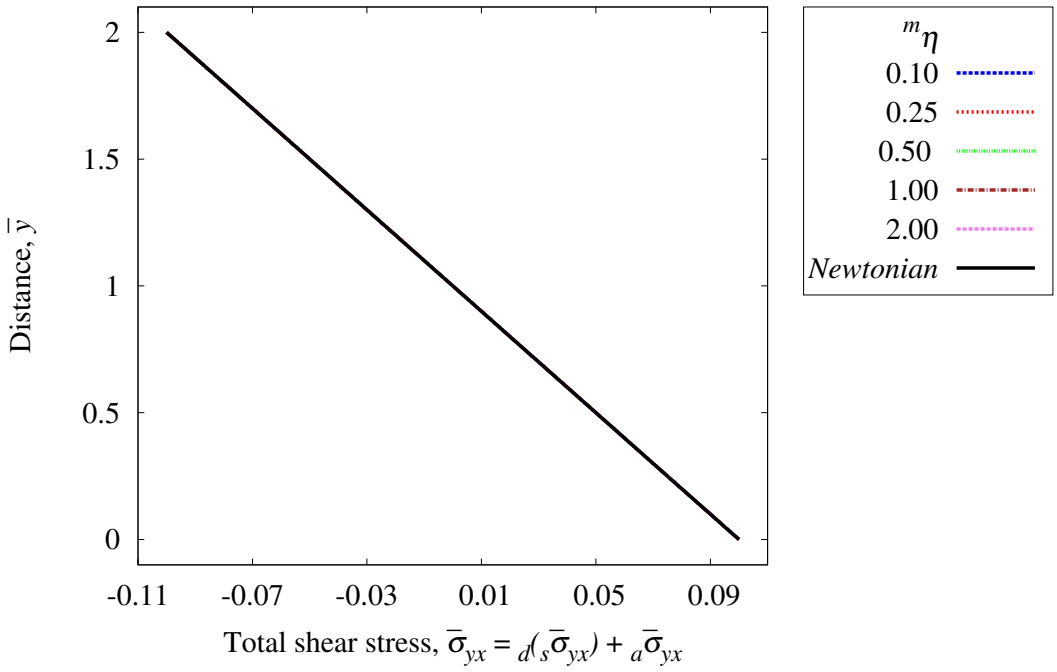

Figure 3.5: Total shear stress $\bar{\sigma}_{yx}$ versus distance $\bar{y}$

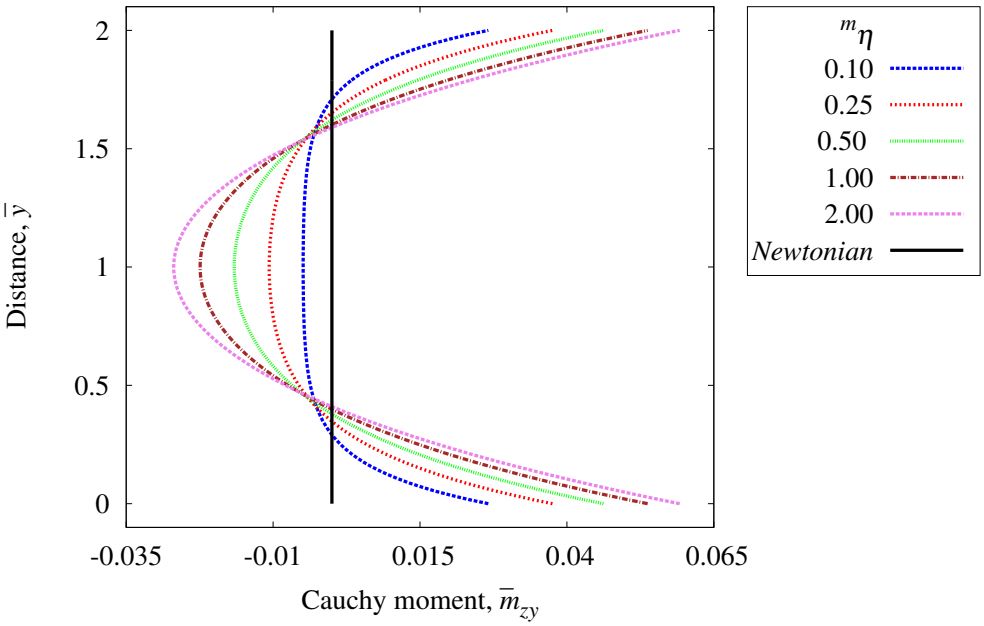

Figure 3.6: Cauchy moment $\overline{m}_{zy}$ versus distance $\overline{y}$

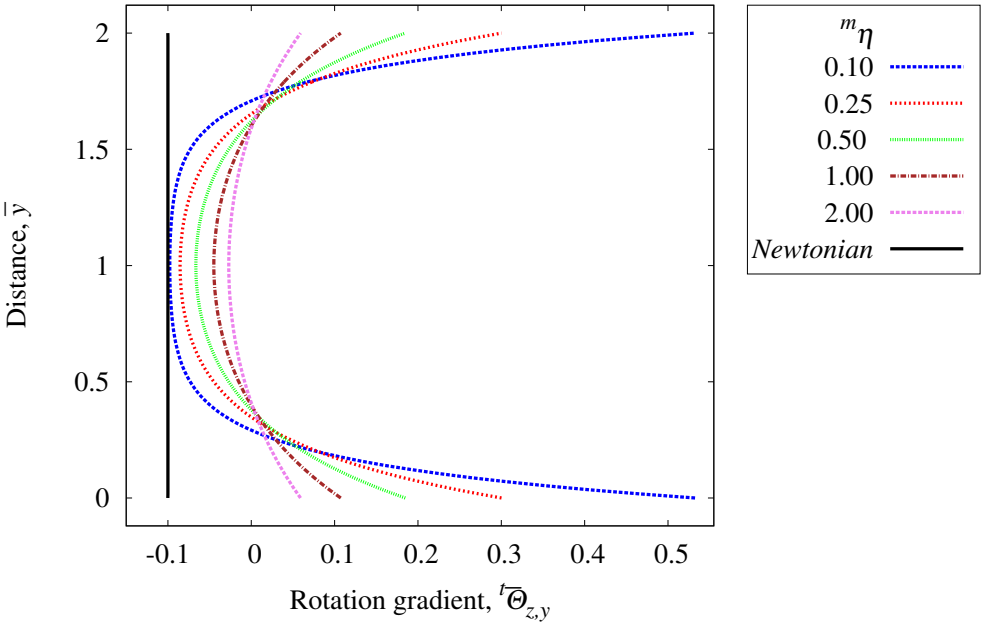

Figure 3.7: Rate of rotation gradient $\dfrac{\partial^2 \overline{u}}{\partial \overline{y}^2}$ versus distance $\overline{y}$

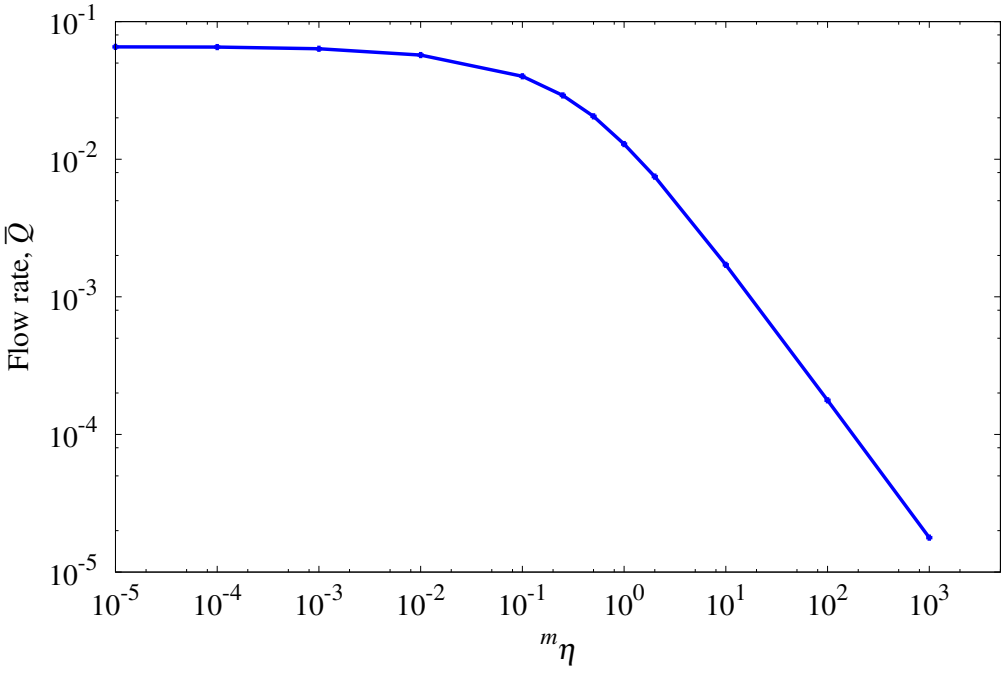

Figure 3.8: Flow rate versus $^{m}\eta$

3.3 Model problem II: Asymmetric sudden expansion

This model problem consists of asymmetric sudden expansion with expansion ratios (ER) of 2.75 : 2, 3 : 2 and 3.5 : 2. A schematic with dimensions and boundary conditions is shown in figure 3.9 (a). A 174 element graded discretization using *p*-version higher order continuity local approximations is shown in figure 3.9 (b). This mesh was arrived by starting with a coarse mesh of 64 element model and then systematically refining the mesh based on the values of the mean square error (MSE). At each stage, *p*-convergence of the mesh was examined and refinement was made in the areas containing elements with relatively high values of MSE. Accurate solutions were obtained using the 174 element mesh and increasing the number of elements beyond 174 did not significantly improve the results for any of the wide range of flow conditions examined here. The smallest element size is 0.1 units at the expansion point. The following fluid properties and reference quantities are used

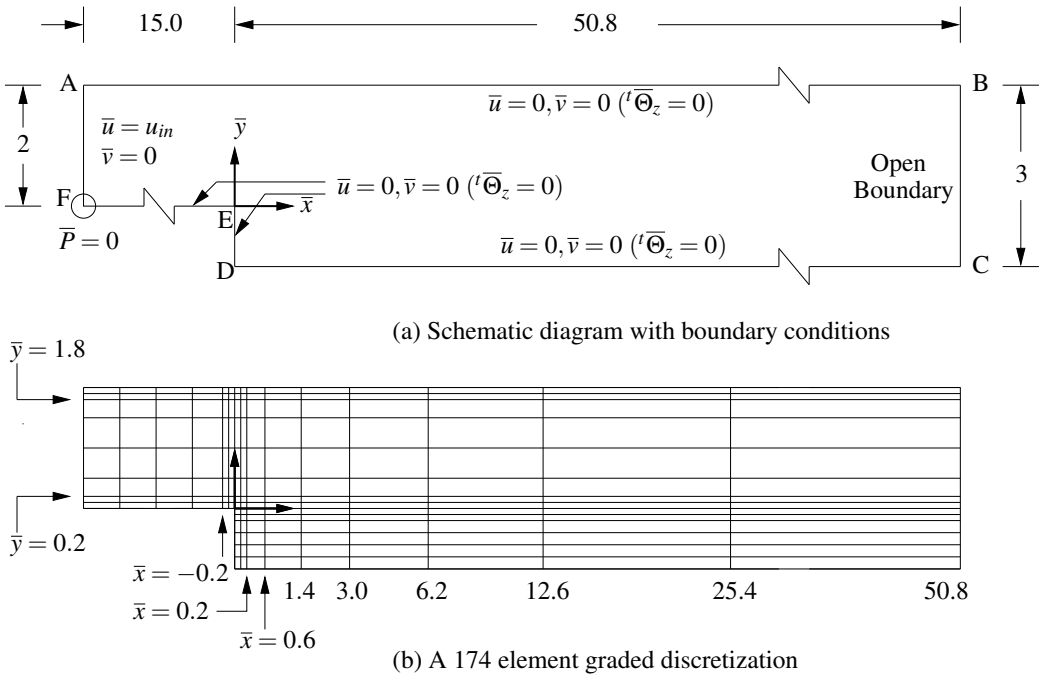

Figure 3.9: Schematic representation and finite element models for asymmetric expansion

$$\hat{\overline{\rho}} = 998.2\ kg/m^3 \quad , \quad \hat{\eta} = 1.002 \times 10^{-3}\ Pa$$

$$\rho_0 = 998.2\ kg/m^3 \quad , \quad \eta_0 = 1.002 \times 10^{-3}\ Pa$$

$$L_0 = 0.015\ m \quad , \quad u_0 = 0.0153247\ m/s$$

This results in

$$\overline{\rho} = 1 \quad , \quad \eta = 1 \quad , \quad Re = \frac{\rho_0 L_0 u_0}{\eta_0} = 229$$

In this model problem we study how the flow physics changes with varying ${}^m\eta$ and varying expansion ratios for a fixed flow rate. Thus for all values of ${}^m\eta$ and the three expansion ratios, we specify velocity $\overline{u}$ boundary condition at inlet that corresponds to fully developed flow of Newtonian fluid between parallel plates separated by a distance of two unit. The peak velocity is chosen so that the flow rate (for unit depth) is 2.02 unit that remains constant for all studies.

For dimensionless η = 1, the studies presented here consider ${}^m\eta$ in the range 0.00005 - 0.001 including ${}^m\eta$ = 0. The mathematical models for both internal polar fluid and classical fluid con-

sist of first order partial differential equations hence local approximations of class C^{11} $(\overline{\Omega}^e)$ in $H^{k,p}(\overline{\Omega}^e)$; $k = 2$ spaces ensure that the integrals over the discretization remains Riemann. All numerical studies are conducted at p-level of 9 for which residual function I for $\overline{\Omega}^T$ is of the order of $0(10^{-6})$ or lower ensuring good accuracy of the computed solutions.

Progressively increasing values of ${}^m\eta$ implies that the fluid progressively offers more resistance to flow. However, if the flow rate is kept constant for progressively increasing values of ${}^m\eta$ then the changes in flow physics is reflected in terms of velocity field, stress field, moment tensor and rotation rate tensor. Numerical solutions are computed for ${}^m\eta = 0$, 0.00005, 0.0001, 0.0005, and 0.001.

Figures 3.10 - 3.12 show velocity $\overline{u}$ versus $\overline{y}$ at $\overline{x} = 0$ (expansion point) for ER = 2.75 : 2, 3 : 2 and 3.5 : 2. We observe that peak value of $\overline{u}$ progressively increases with increasing ${}^m\eta$ for each ER with while the flow rate in each case remains 2.02.

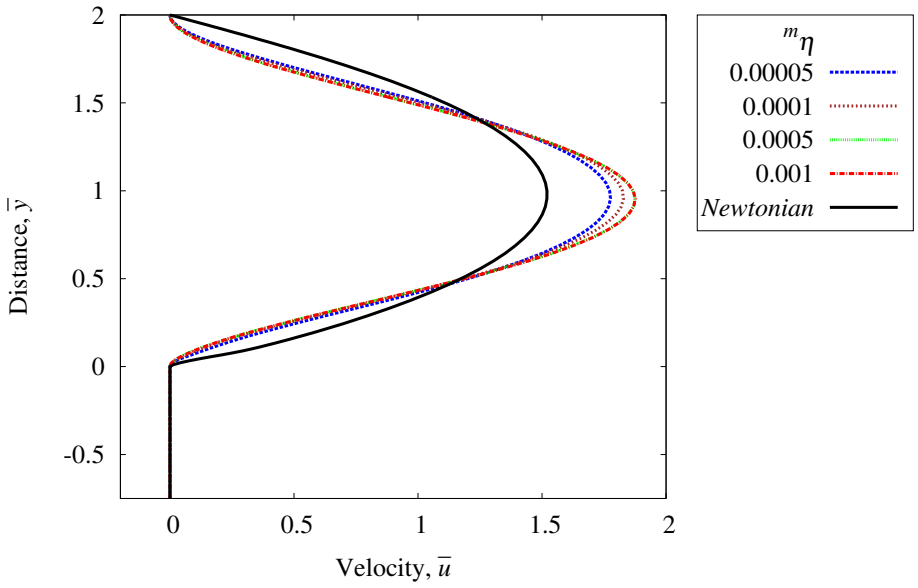

Figure 3.10: Velocity $\overline{u}$ versus distance $\overline{y}$ at $\overline{x} = 0.0$; ER = 2.75 : 2

Similar plots of $\overline{u}$ versus $\overline{y}$ at $\overline{x} = 5.0$, and 50.8 (outlet) are shown in figures 3.13 - 3.15 and 3.16 - 3.18. At outlet the $\overline{u}$ versus $\overline{y}$ plots exhibit similar behavior as at $\overline{x} = 0.0$ i.e. progressively increasing peak value of $\overline{u}$ with progressively increasing values of ${}^m\eta$. However at $\overline{x} = 5.0$ the

$\overline{u}$ versus $\overline{y}$ graphs change radically with increasing ${}^{m}\eta$ due to drastic change in the physics of recirculation region i.e. its size and shape, but in all cases flow rate of 2.02 is achieved.

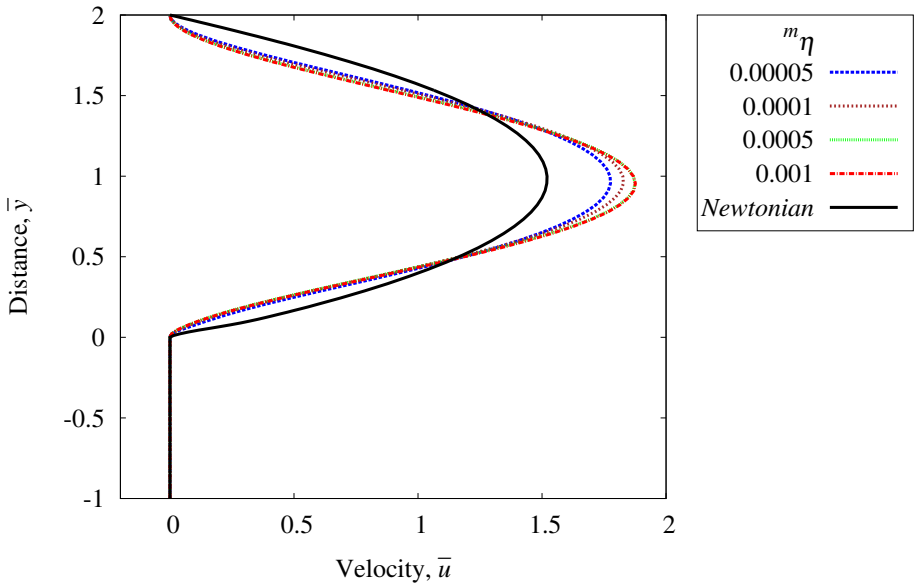

Figure 3.11: Velocity $\overline{u}$ versus distance $\overline{y}$ at $\overline{x} = 0.0$; ER = 3 : 2

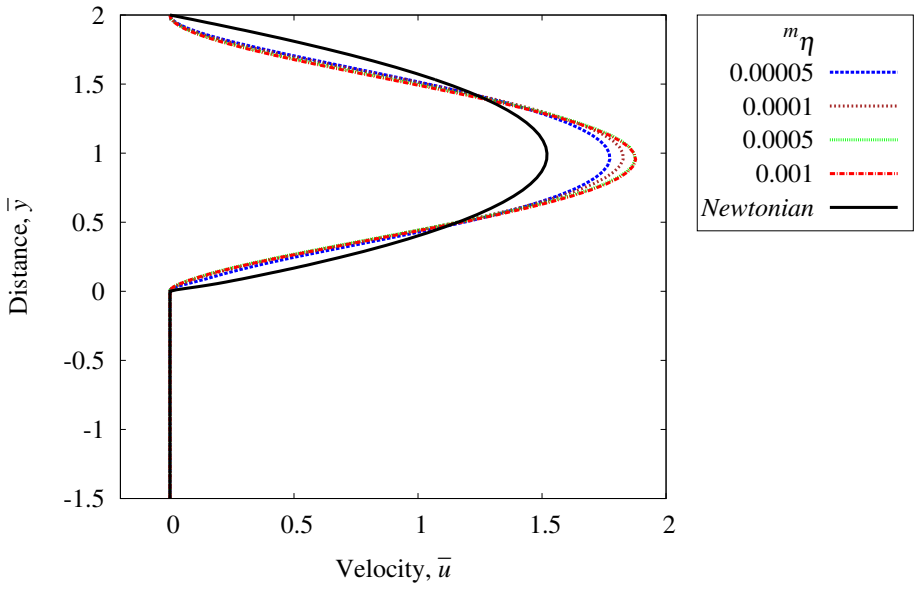

Figure 3.12: Velocity $\overline{u}$ versus distance $\overline{y}$at $\overline{x} = 0.0$; ER = 3.5 : 2

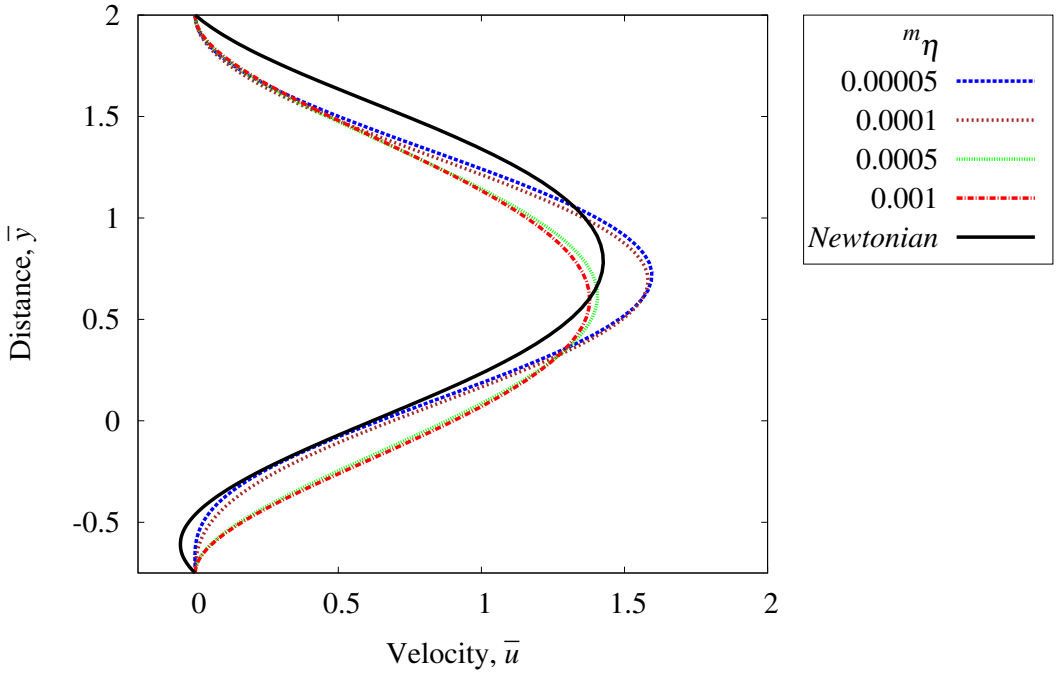

Figure 3.13: Velocity $\bar{u}$ versus distance $\bar{y}$ at $\bar{x}$ = 5.0 ; ER = 2.75 : 2

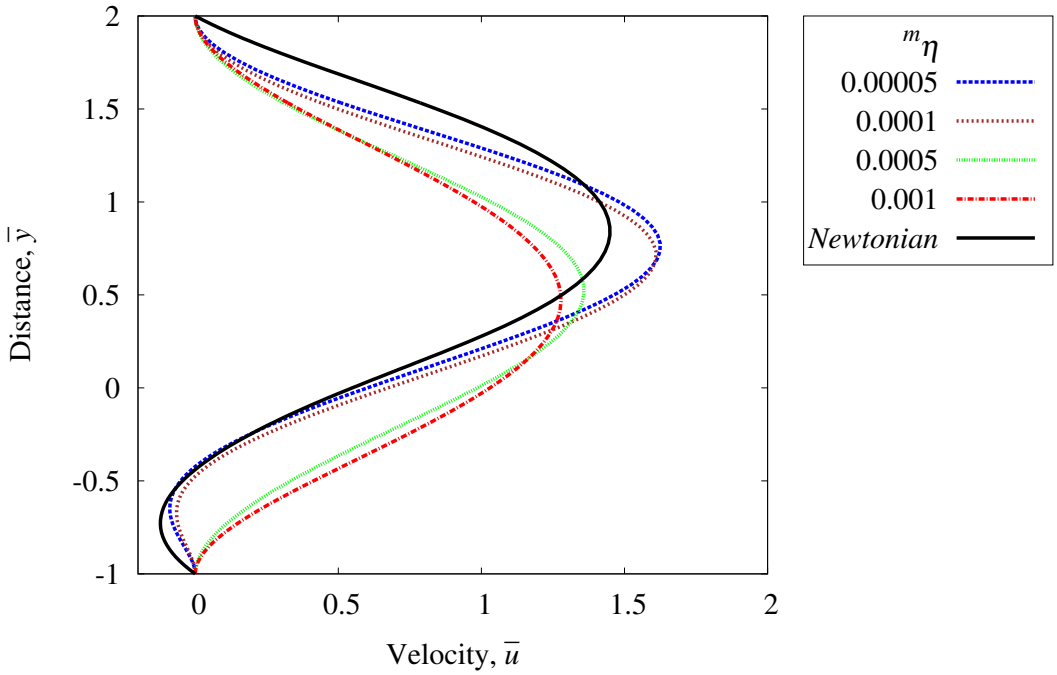

Figure 3.14: Velocity $\bar{u}$ versus distance $\bar{y}$ at $\bar{x}$ = 5.0 ; ER = 3 : 2

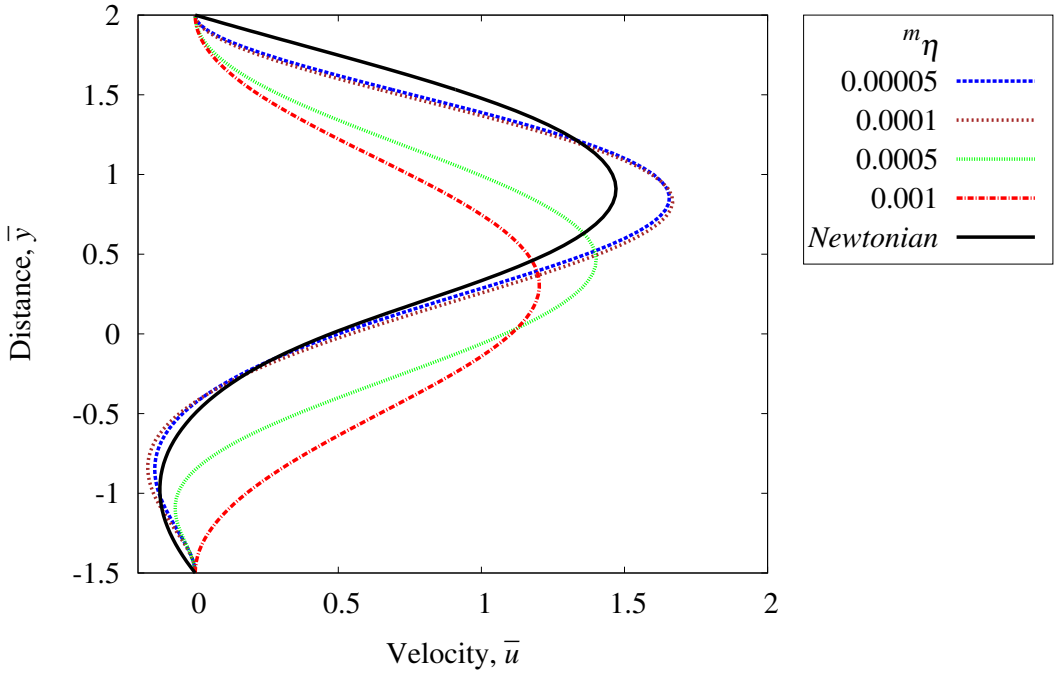

Figure 3.15: Velocity $\bar{u}$ versus distance $\bar{y}$ at $\bar{x}$ = 5.0 ; ER = 3.5 : 2

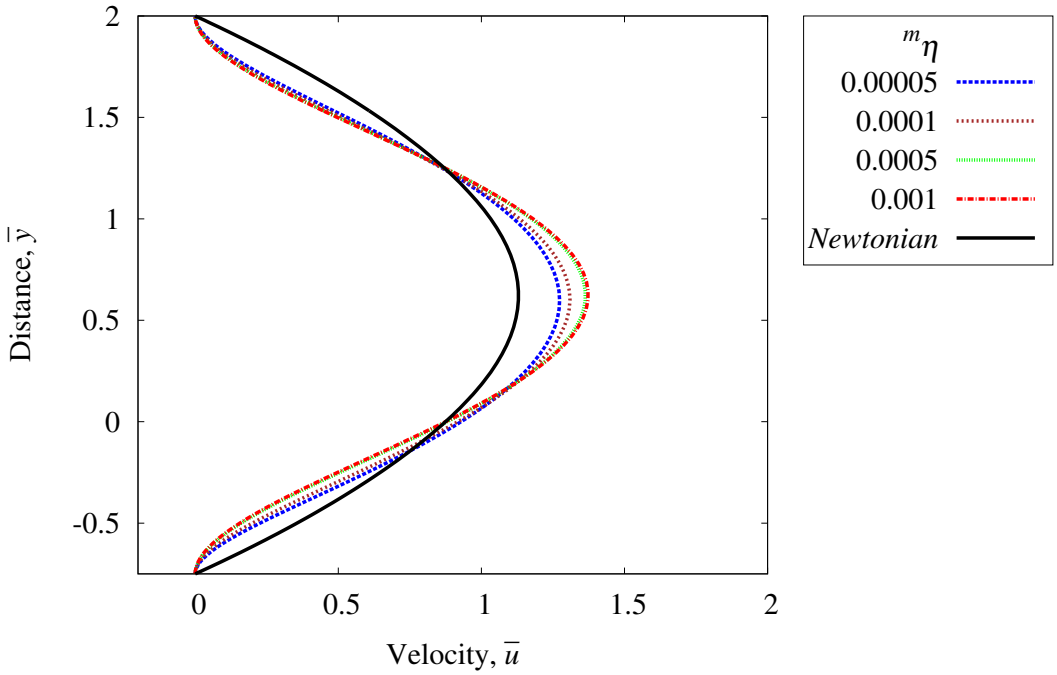

Figure 3.16: Velocity $\bar{u}$ versus distance $\bar{y}$ at $\bar{x}$ = 50.8 ; ER = 2.75 : 2

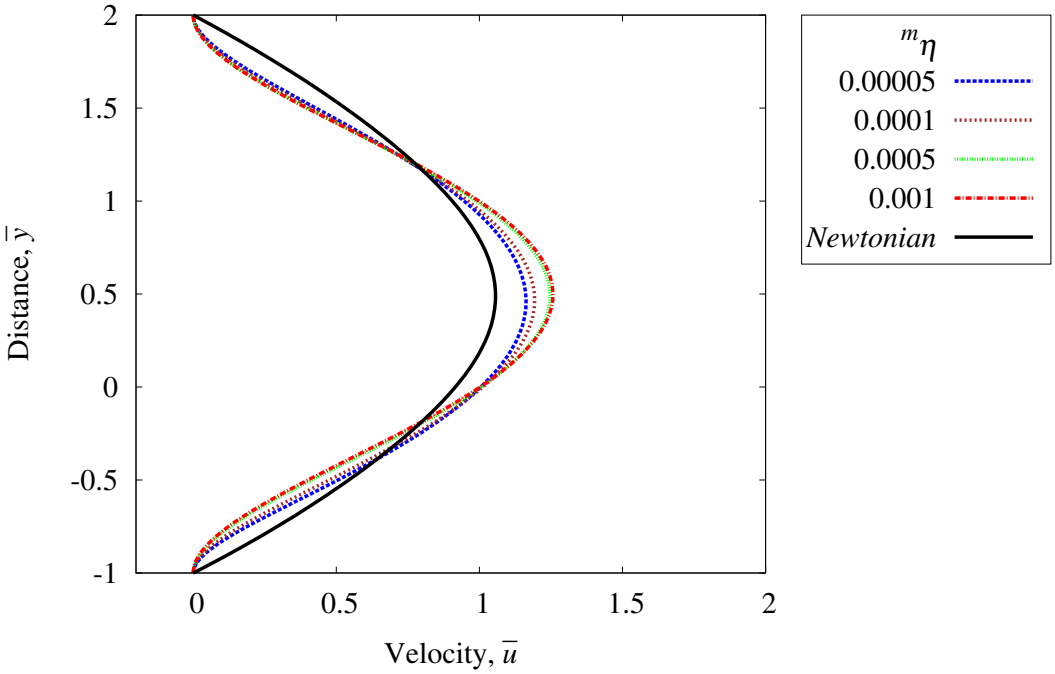

Figure 3.17: Velocity $\bar{u}$ versus distance $\bar{y}$ at $\bar{x}$ = 50.8 ; ER = 3 : 2

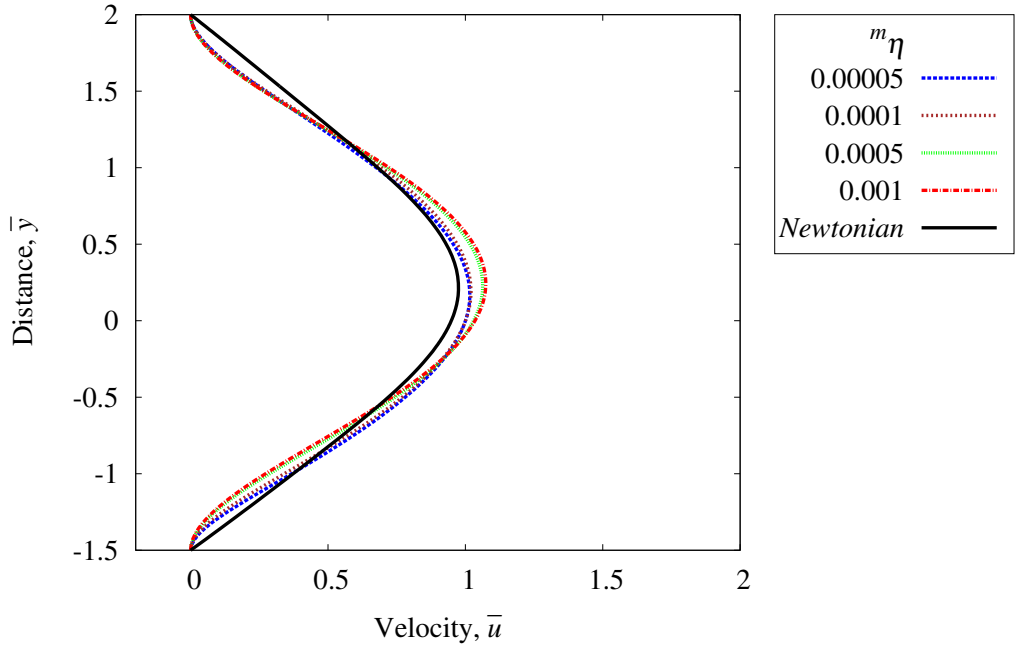

Figure 3.18: Velocity $\bar{u}$ versus distance $\bar{y}$ at $\bar{x}$ = 50.8 ; ER = 3.5 : 2

Graphs of $\overline{\sigma}_{yx} = {}_d({}_s\overline{\sigma}_{yx}) + {}_a\overline{\sigma}_{yx}$ versus $\bar{y}$ at $\bar{x} = 0.0$ (expansion point) are shown in figures 3.19 - 3.21 for the three expansion ratios for same values of ${}^m\eta$. At and in the vicinity of $\bar{y} = 0$, the stress field is not resolved due to singularity at the expansion point, however the oscillation remain isolated and do not disturb the solution away from the immediate neighborhood of $\bar{y} = 0.0$. Similar graphs of $\overline{\sigma}_{yx}$ versus $\bar{y}$ are shown in figures 3.22 - 3.24, 3.25 - 3.27 and 3.28 - 3.30 that correspond to $\bar{x} = 0.2$, $\bar{x} = 5.0$ and $\bar{x} = 50.8$. Progressively higher peak values of $\overline{\sigma}_{yx}$ are observed with increasing ${}^m\eta > 0$ compared to ${}^m\eta = 0.0$. At outlet $\overline{\sigma}_{yx}$ for ${}^m\eta = 0.0$ (Newtonian) is almost negligible compared to $\overline{\sigma}_{yx}$ for ${}^m\eta \neq 0$ illustrating the added resistance offered by the internal polar physics.

Plot of moment $\overline{m}_{zx}$ versus $\bar{y}$ at $\bar{x} = 0.0$ for ER of $2.75 : 2$ is shown in figure 3.31. Once again oscillations are observed in the near vicinity of $\bar{y} = 0.0$ due to singularity at $\bar{x} = \bar{y} = 0$. Similar behavior of $\overline{m}_{zx}$ is observed for the other two expansion ratios in figures 3.32 - 3.33 . Graphs of $\overline{m}_{zx}$ versus $\bar{y}$ at $\bar{x} = 0.2$ and $\bar{x} = 5.0$ for the three expansion ratios are shown in figures 3.34 - 3.36, 3.37 - 3.39. Progressively increasing values of $\overline{m}_{zx}$ are observed with increasing values of ${}^m\eta$. Figure 3.40 shows a plot of $\overline{m}_{zx}$ versus $\bar{y}$ at $\bar{x} = 50.8$ for ER of $2.75 : 2$. Due to flow being almost fully developed at $\bar{x} = 50.8$, $\overline{m}_{zx}$ is practically zero. Similar behaviors are observed for the other two expansion ratios in figures 3.41 - 3.42.

Figure 3.43 shows a plot of $\overline{m}_{zy}$ versus $\bar{y}$ at $\bar{x} = 0.0$ for ER of $2.75 : 2$. Except at the immediate vicinity of $\bar{x} = \bar{y} = 0$, the behavior is smooth with progressively increasing values for progressively increasing ${}^m\eta$ are observed. Similar behavior is also observed for other expansion ratios in figures 3.44 - 3.45. Graphs of $\overline{m}_{zy}$ versus $\bar{y}$ at $\bar{x} = 0.2$, 5.0 and 50.8 for the three expansion ratios are shown in figures 3.46 - 3.48, 3.49 - 3.51 and 3.52 - 3.54. We clearly observed the increasing values of $\overline{m}_{zy}$ with increasing ${}^m\eta$.

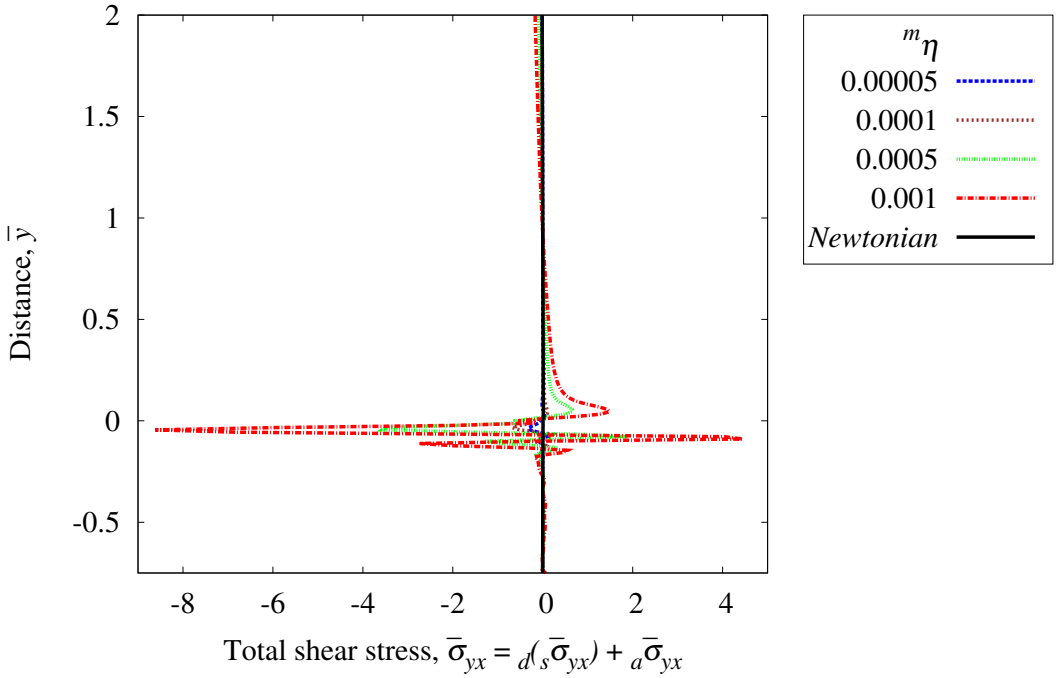

Figure 3.19: Total shear stress $\bar{\sigma}_{yx}$ versus distance $\bar{y}$ at $\bar{x} = 0.0$; ER = 2.75 : 2

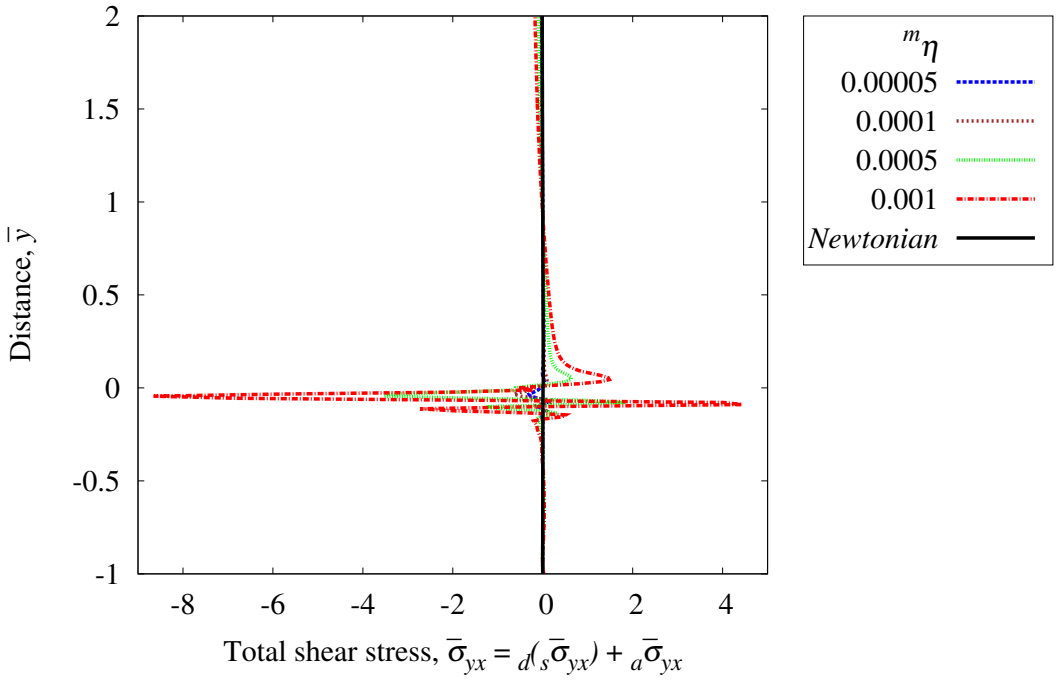

Figure 3.20: Total shear stress $\bar{\sigma}_{yx}$ versus distance $\bar{y}$ at $\bar{x} = 0.0$; ER = 3 : 2

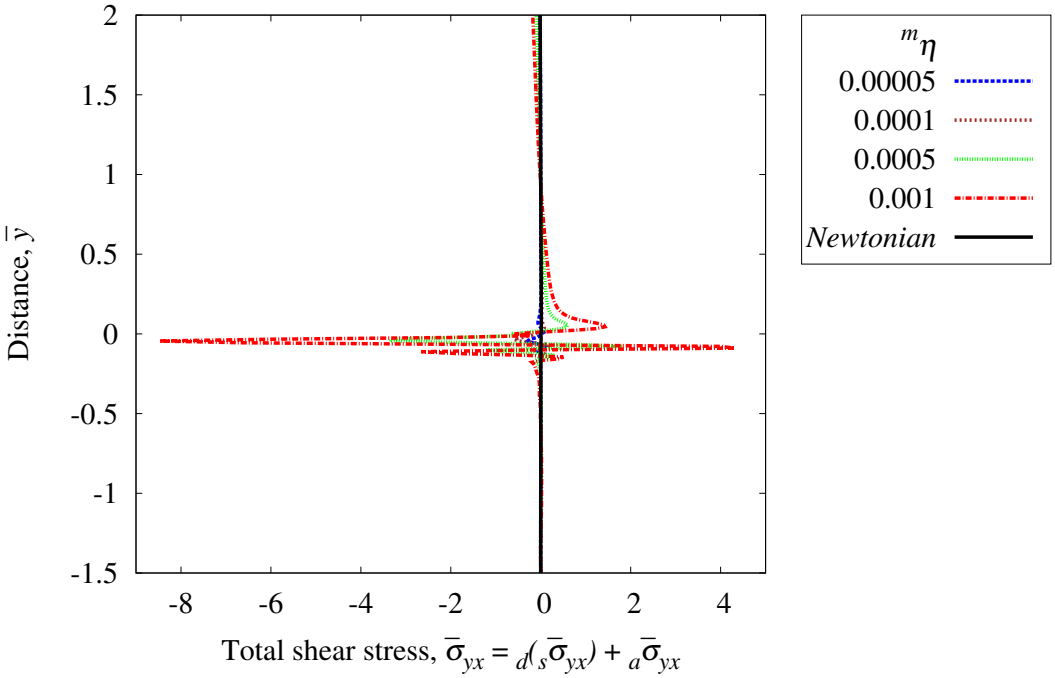

Figure 3.21: Total shear stress $\bar{\sigma}_{yx}$ versus distance $\bar{y}$ at $\bar{x} = 0.0$; ER = 3.5 : 2

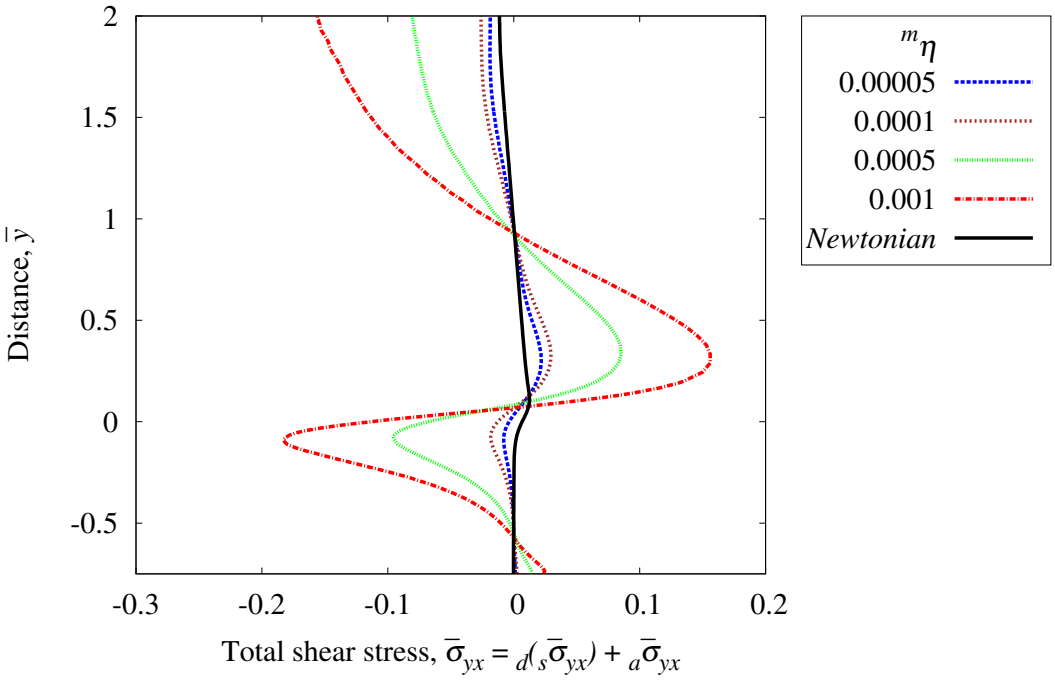

Figure 3.22: Total shear stress $\bar{\sigma}_{yx}$ versus distance $\bar{y}$ at $\bar{x} = 0.2$; ER = 2.75 : 2

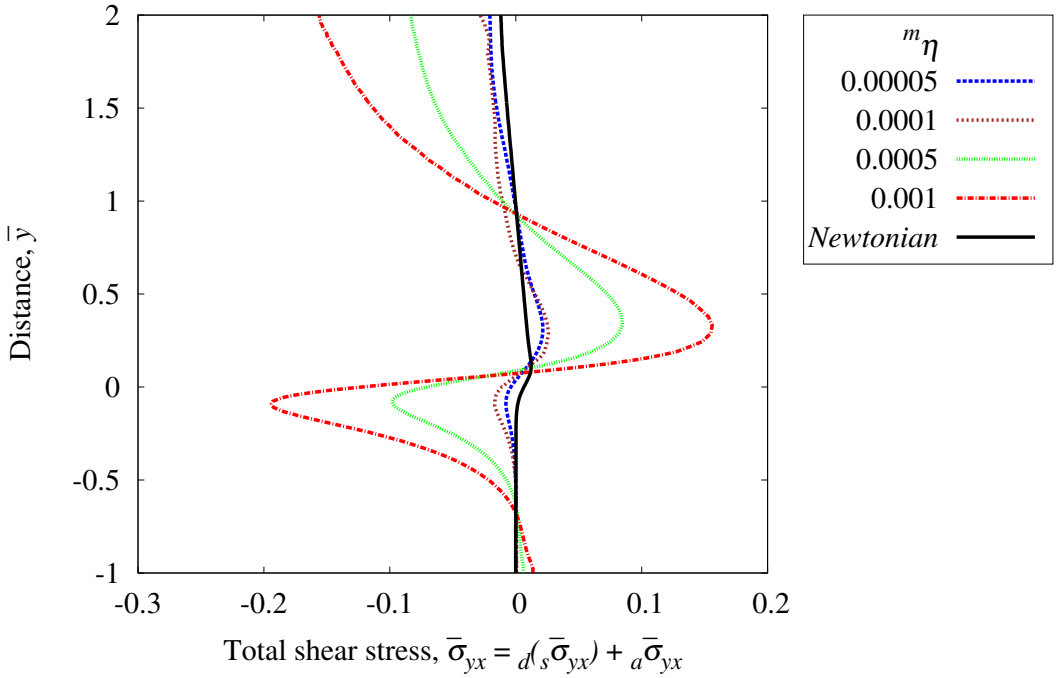

Figure 3.23: Total shear stress $\bar{\sigma}_{yx}$ versus distance $\bar{y}$ at $\bar{x} = 0.2$; ER = 3 : 2

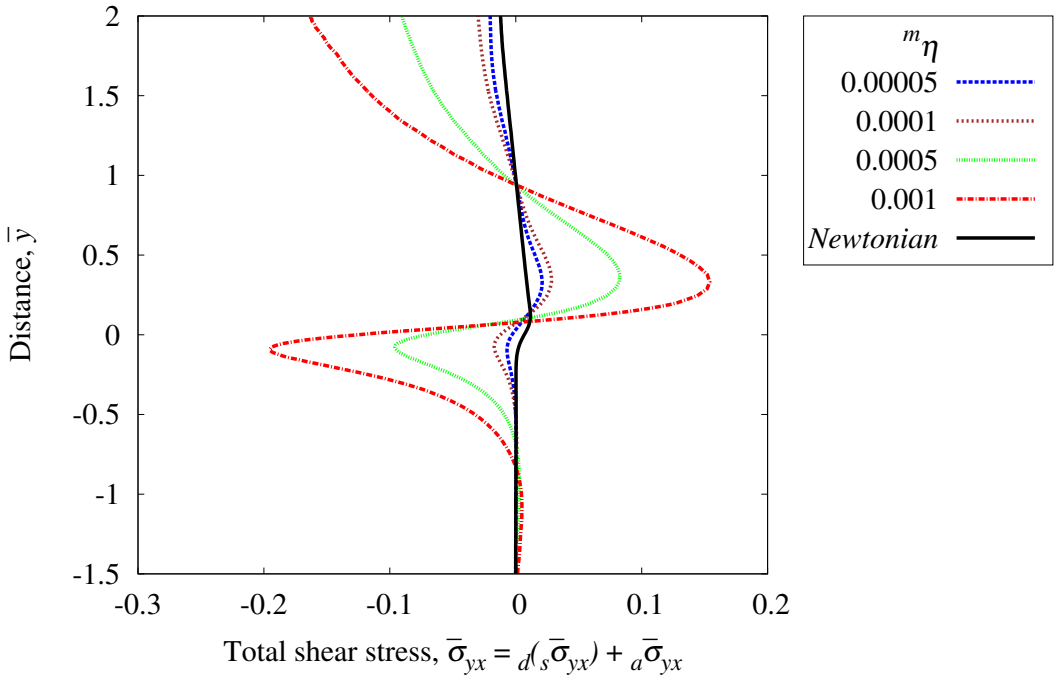

Figure 3.24: Total shear stress $\bar{\sigma}_{yx}$ versus distance $\bar{y}$ at $\bar{x} = 0.2$; ER = 3.5 : 2

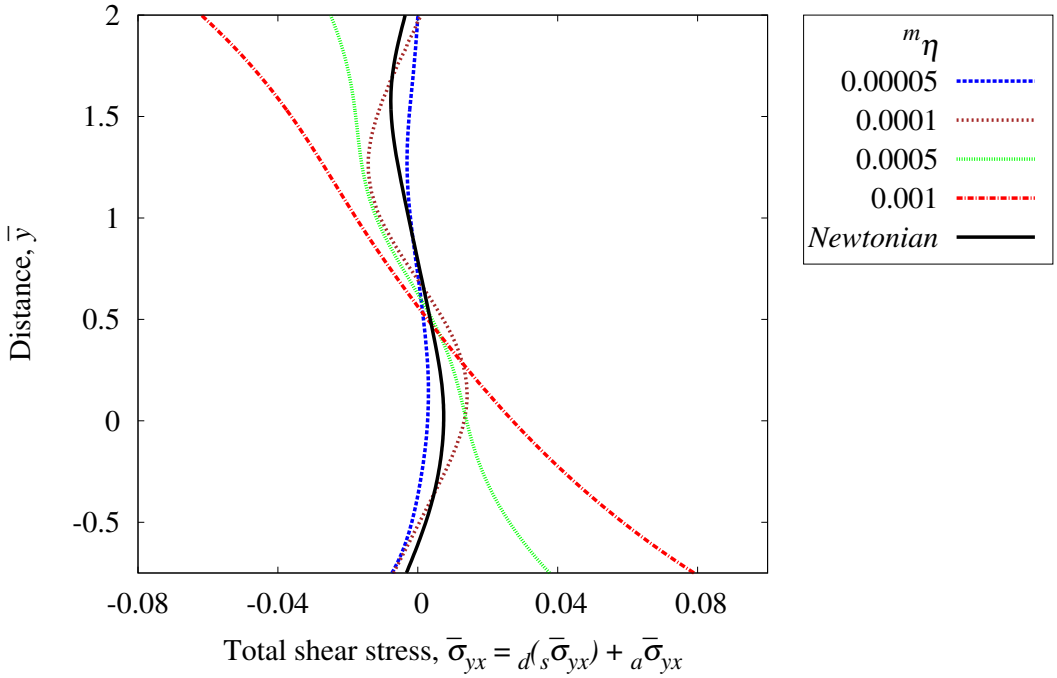

Figure 3.25: Total shear stress $\bar{\sigma}_{yx}$ versus distance $\bar{y}$ at $\bar{x} = 5.0$; ER = 2.75 : 2

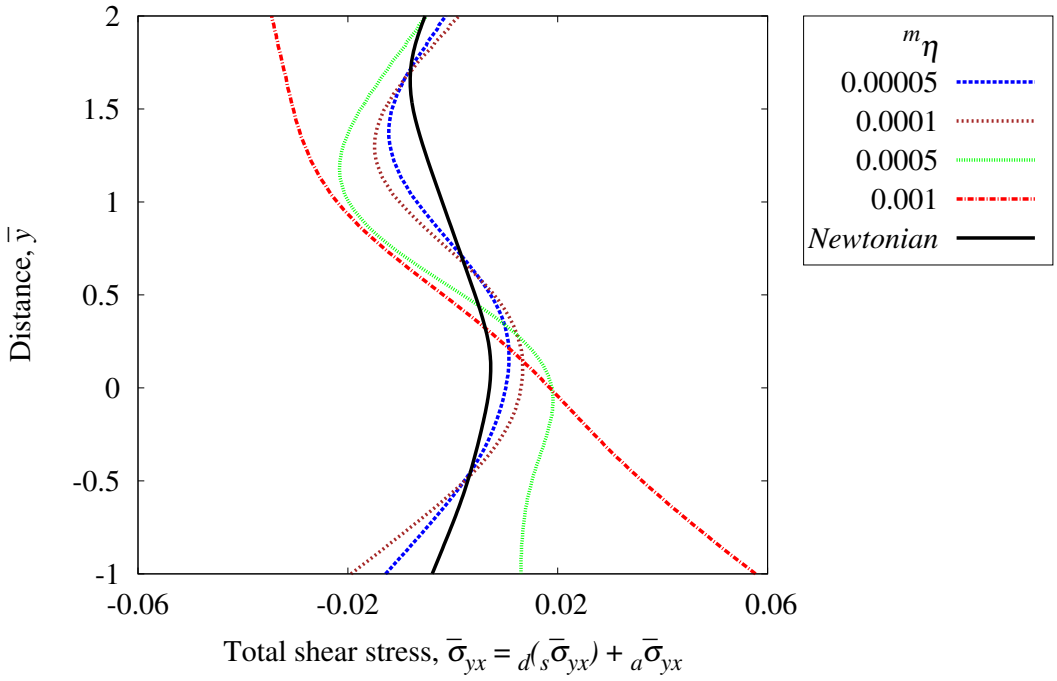

Figure 3.26: Total shear stress $\bar{\sigma}_{yx}$ versus distance $\bar{y}$ at $\bar{x} = 5.0$; ER = 3 : 2

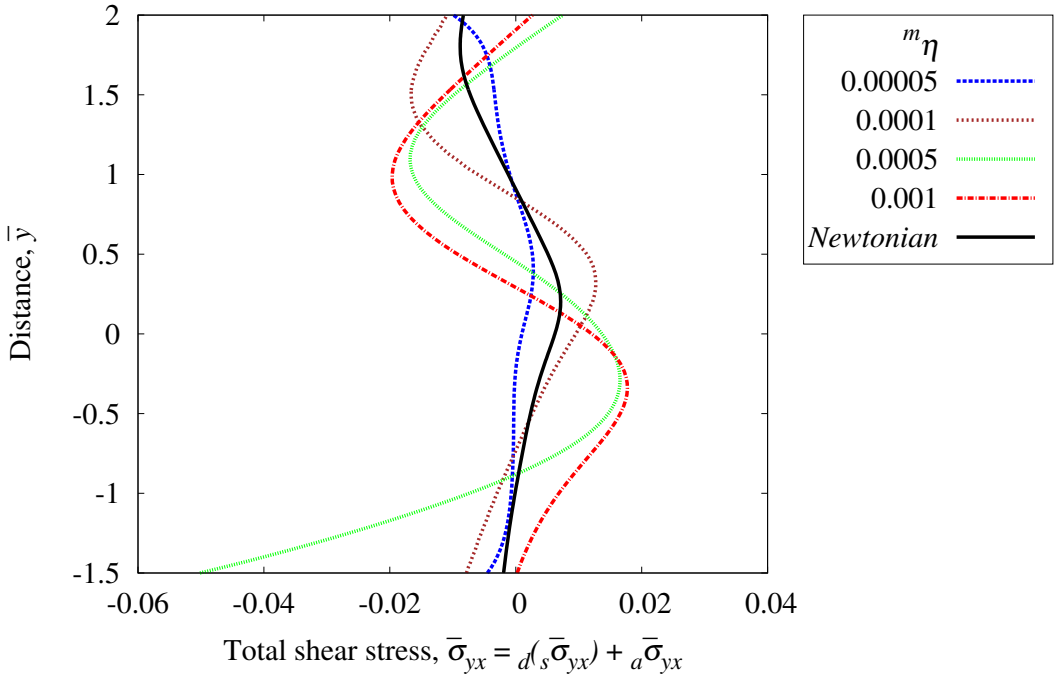

Figure 3.27: Total shear stress $\bar{\sigma}_{yx}$ versus distance $\bar{y}$ at $\bar{x} = 5.0$; ER = 3.5 : 2

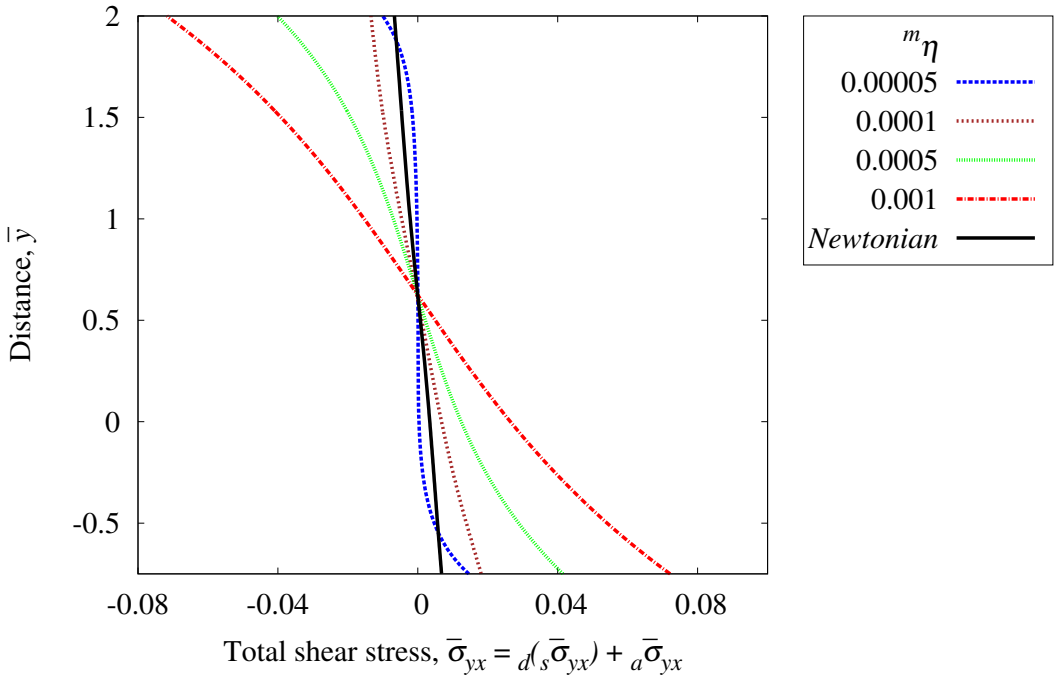

Figure 3.28: Total shear stress $\bar{\sigma}_{yx}$ versus distance $\bar{y}$ at $\bar{x} = 50.8$; ER = 2.75 : 2

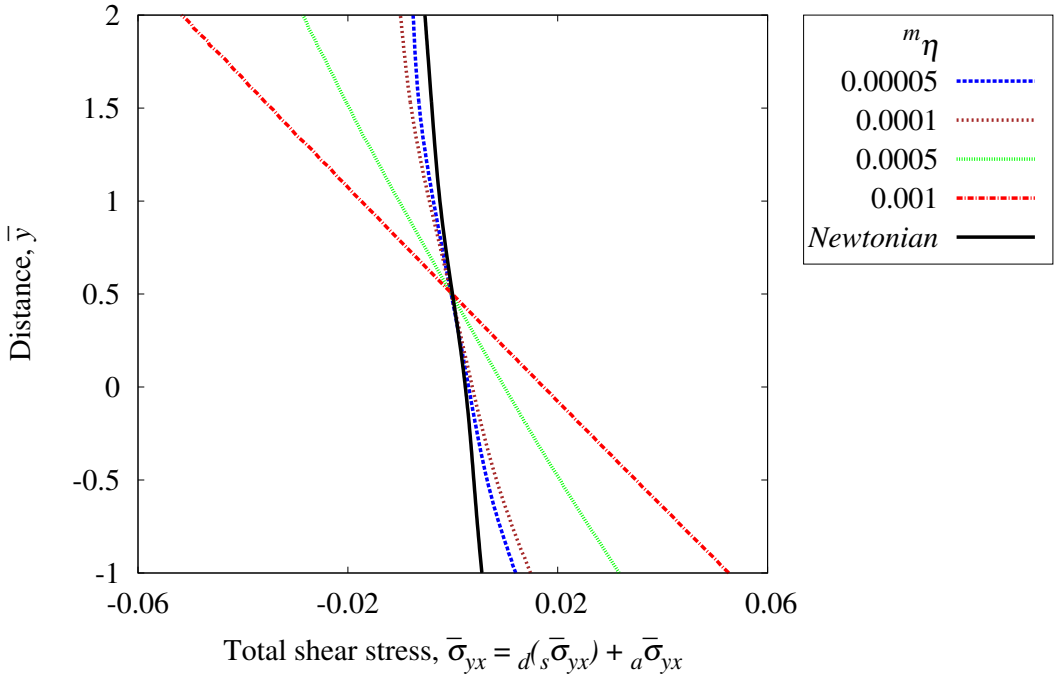

Figure 3.29: Total shear stress $\bar{\sigma}_{yx}$ versus distance $\bar{y}$ at $\bar{x} = 50.8$; ER = 3 : 2

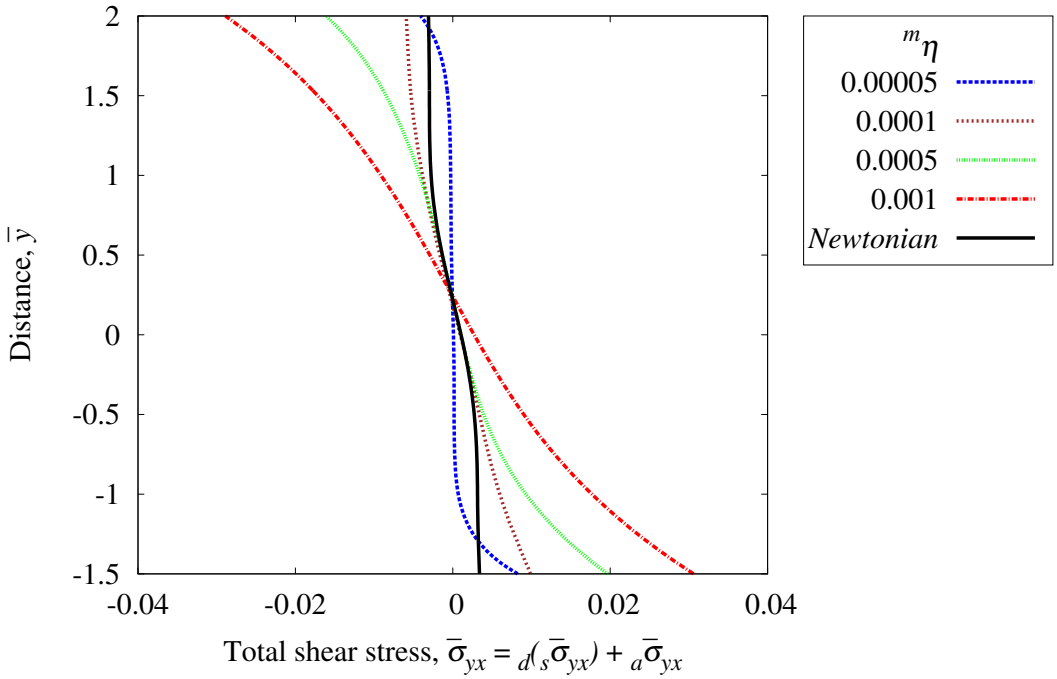

Figure 3.30: Total shear stress $\bar{\sigma}_{yx}$ versus distance $\bar{y}$ at $\bar{x} = 50.8$; ER = 3.5 : 2

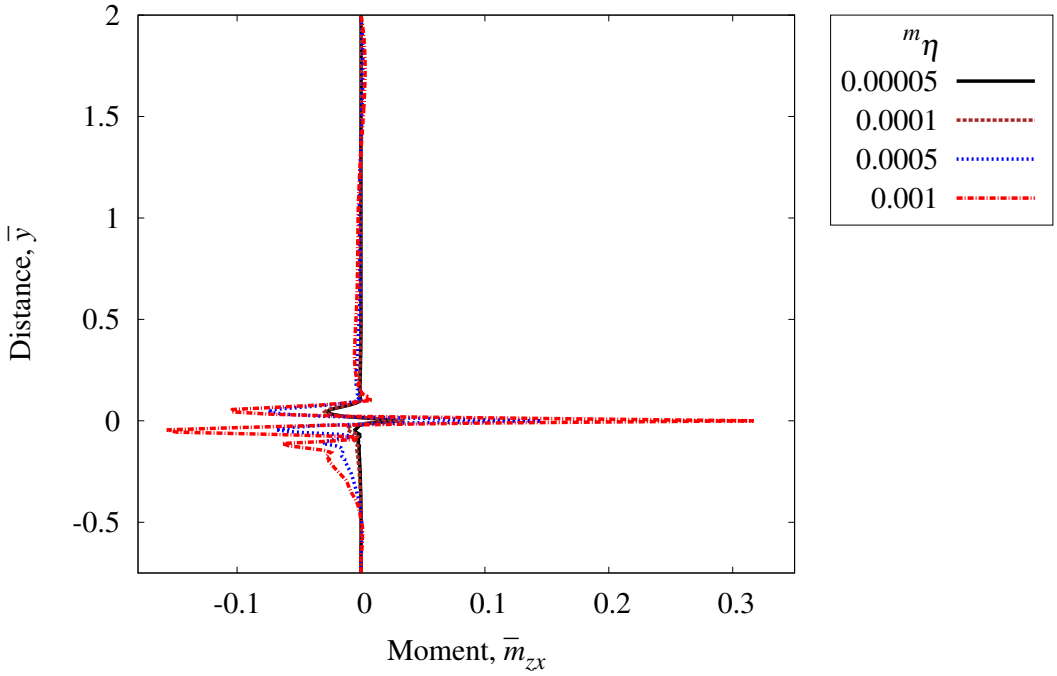

Figure 3.31: Cauchy moment $\bar{m}_{zx}$ versus distance $\bar{y}$ at $\bar{x} = 0.0$; ER = 2.75 : 2

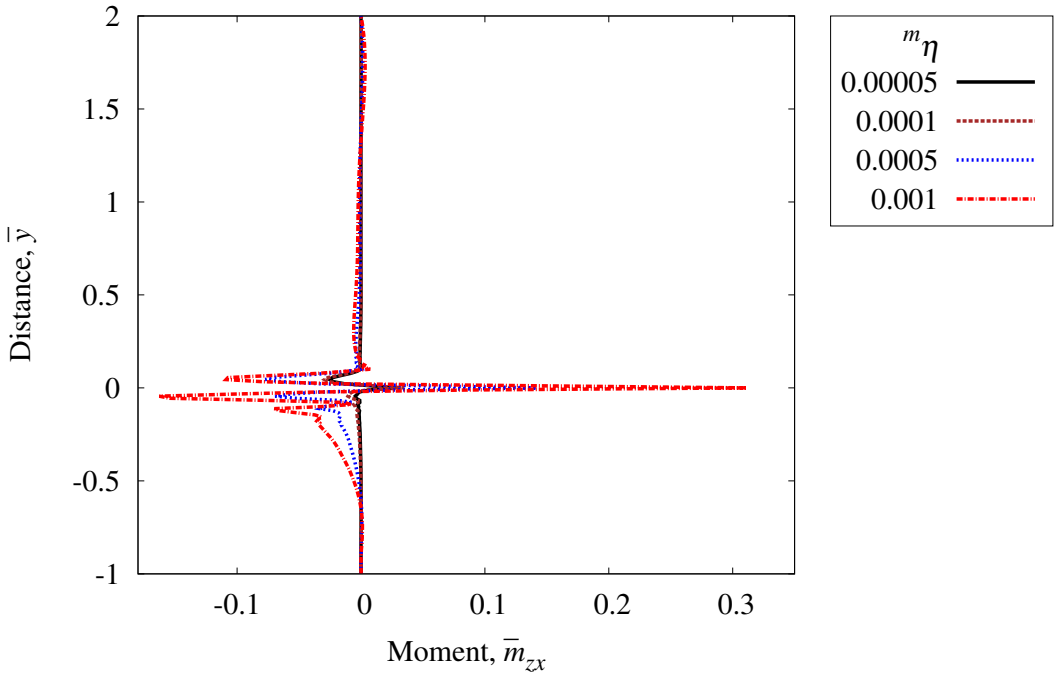

Figure 3.32: Cauchy moment $\bar{m}_{zx}$ versus distance $\bar{y}$ at $\bar{x} = 0.0$; ER = 3 : 2

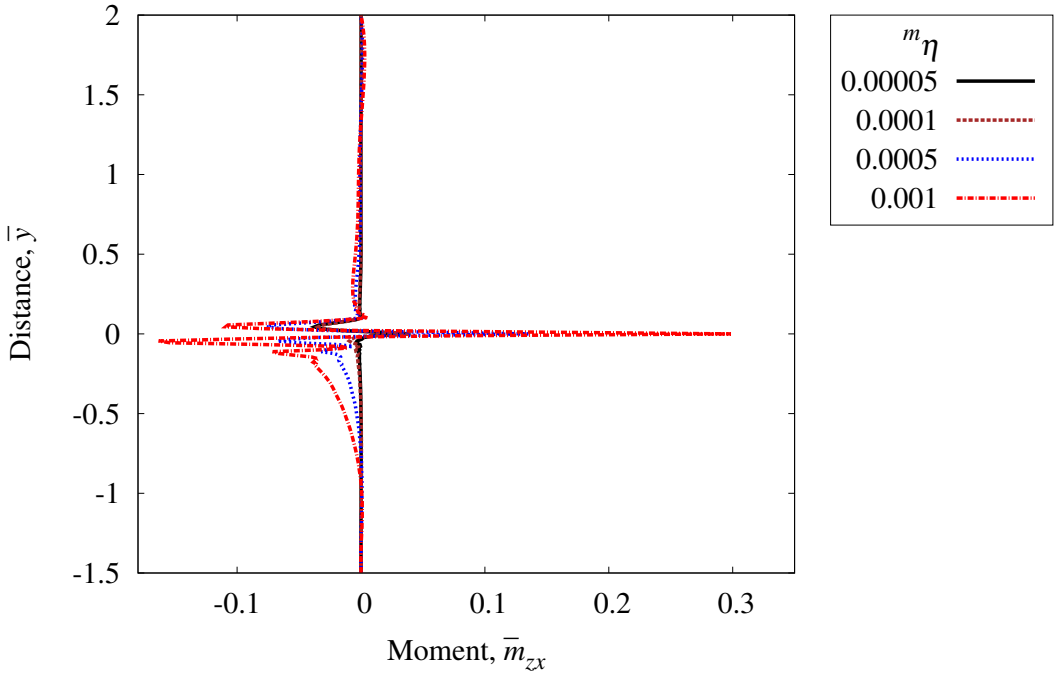

Figure 3.33: Cauchy moment $\bar{m}_{zx}$ versus distance $\bar{y}$ at $\bar{x} = 0.0$; ER = 3.5 : 2

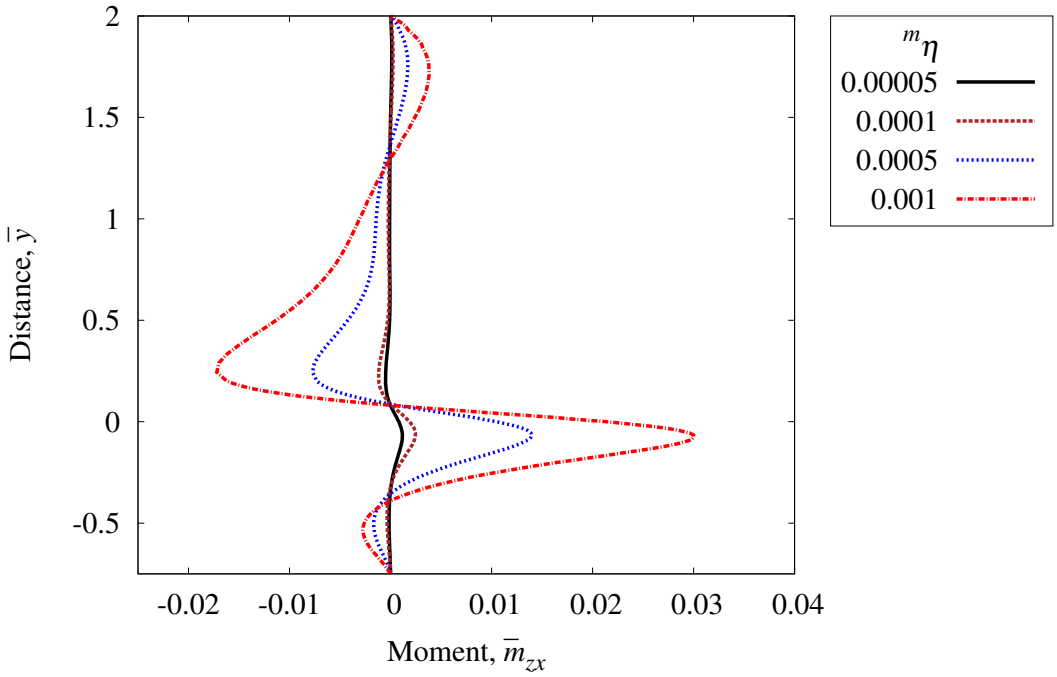

Figure 3.34: Cauchy moment $\bar{m}_{zx}$ versus distance $\bar{y}$ at $\bar{x} = 0.2$; ER = 2.75 : 2

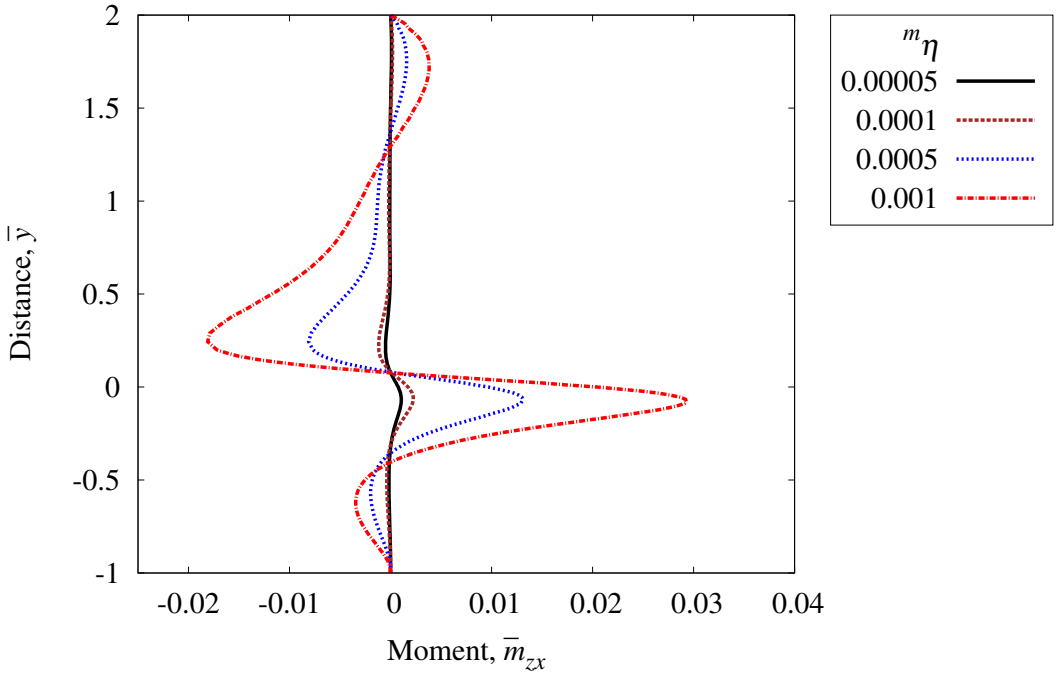

Figure 3.35: Cauchy moment $\overline{m}_{zx}$ versus distance $\bar{y}$ at $\bar{x} = 0.2$; ER = 3 : 2

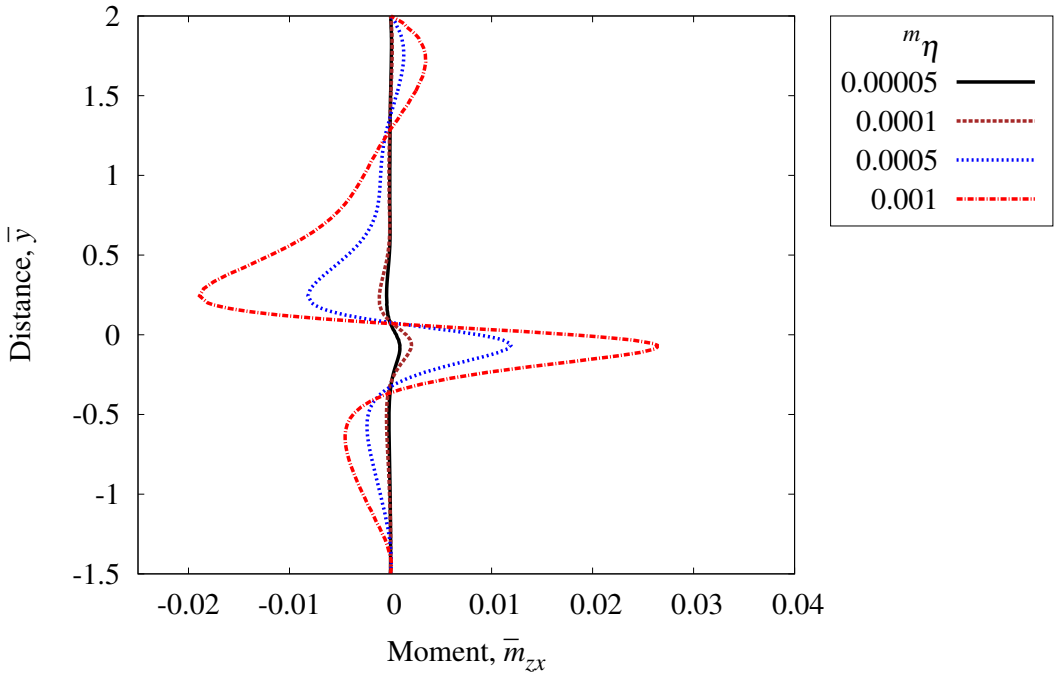

Figure 3.36: Cauchy moment $\overline{m}_{zx}$ versus distance $\bar{y}$ at $\bar{x} = 0.2$; ER = 3.5 : 2

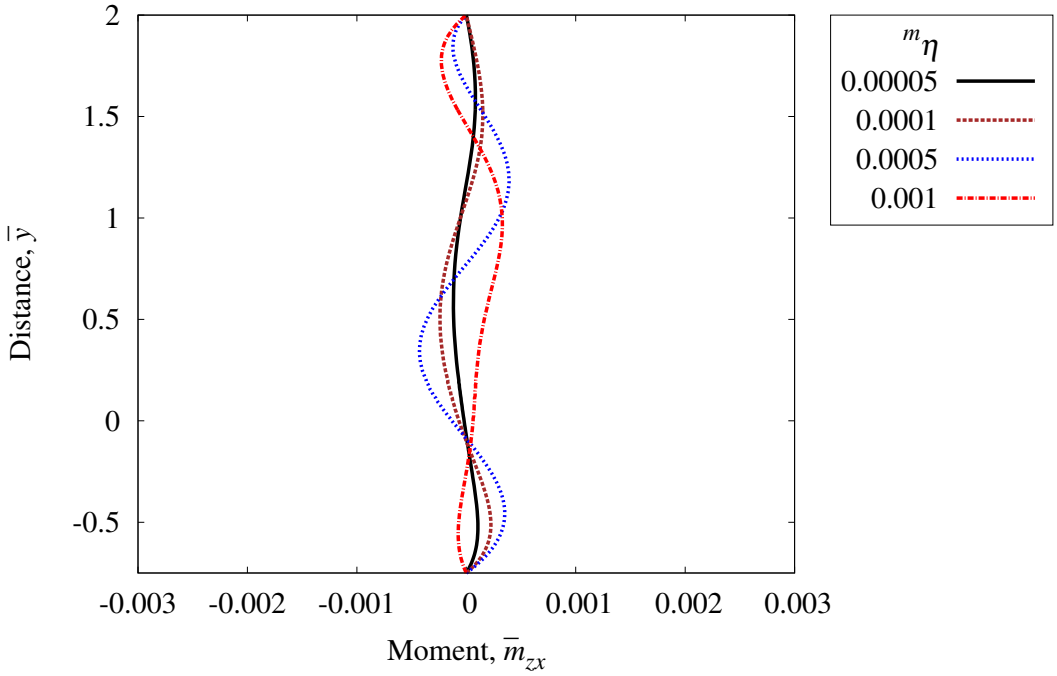

Figure 3.37: Cauchy moment $\bar{m}_{zx}$ versus distance $\bar{y}$ at $\bar{x} = 5.0$; ER = 2.75 : 2

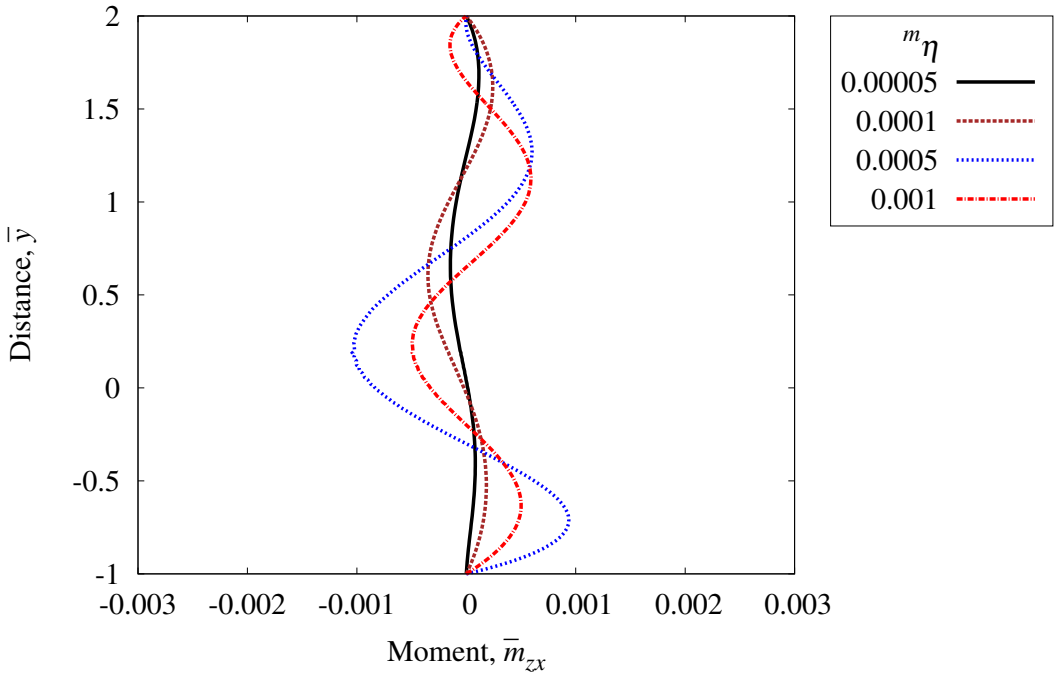

Figure 3.38: Cauchy moment $\bar{m}_{zx}$ versus distance $\bar{y}$ at $\bar{x} = 5.0$; ER = 3 : 2

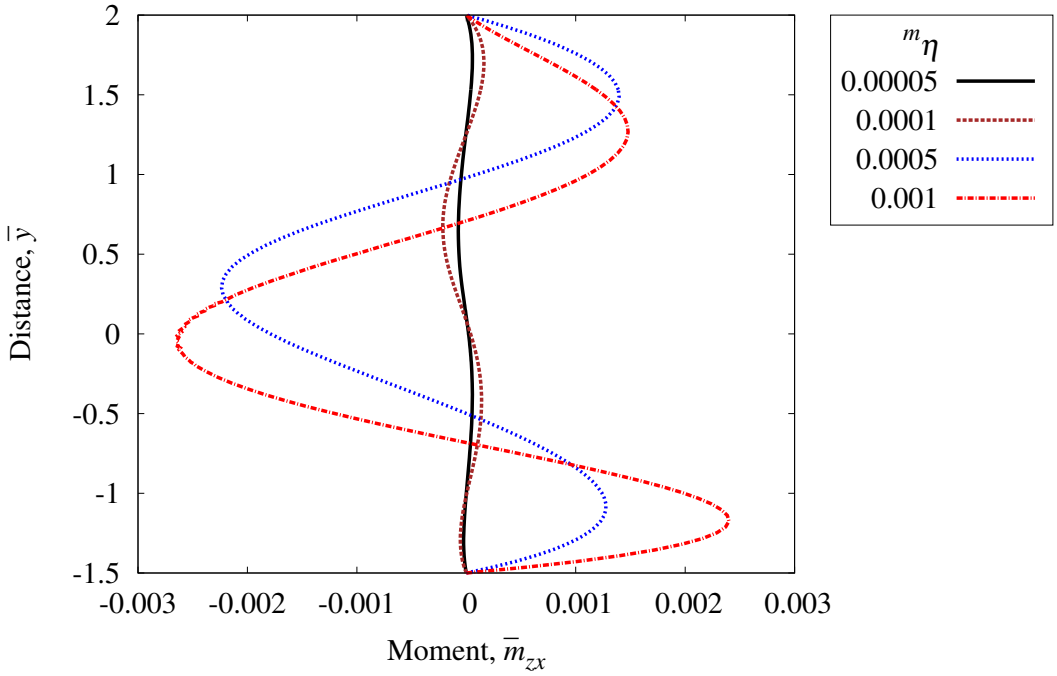

Figure 3.39: Cauchy moment $\bar{m}_{zx}$ versus distance $\bar{y}$ at $\bar{x}$ = 5.0 ; ER = 3.5 : 2

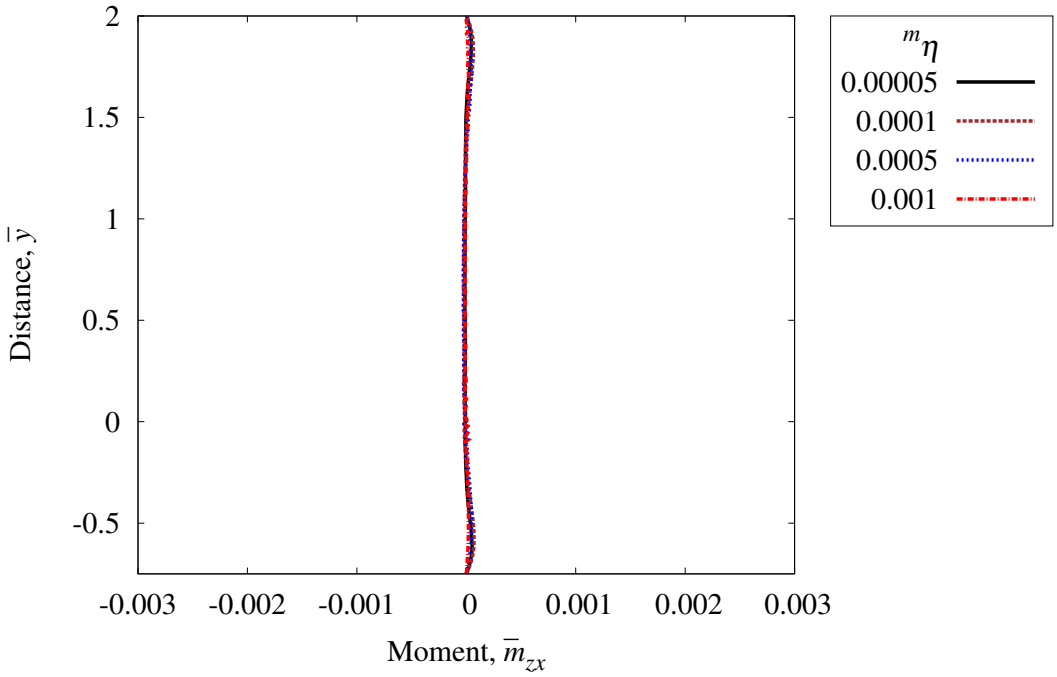

Figure 3.40: Cauchy moment $\bar{m}_{zx}$ versus distance $\bar{y}$ at $\bar{x}$ = 50.8 ; ER = 2.75 : 2

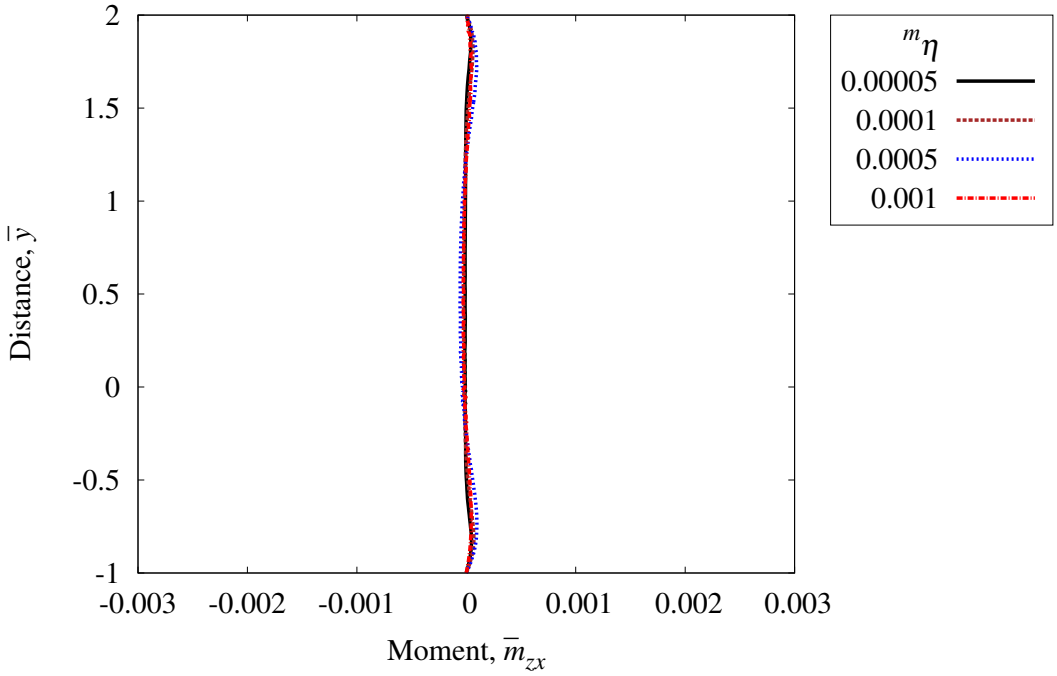

Figure 3.41: Cauchy moment $\bar{m}_{zx}$ versus distance $\bar{y}$ at $\bar{x} = 50.8$; ER = 3 : 2

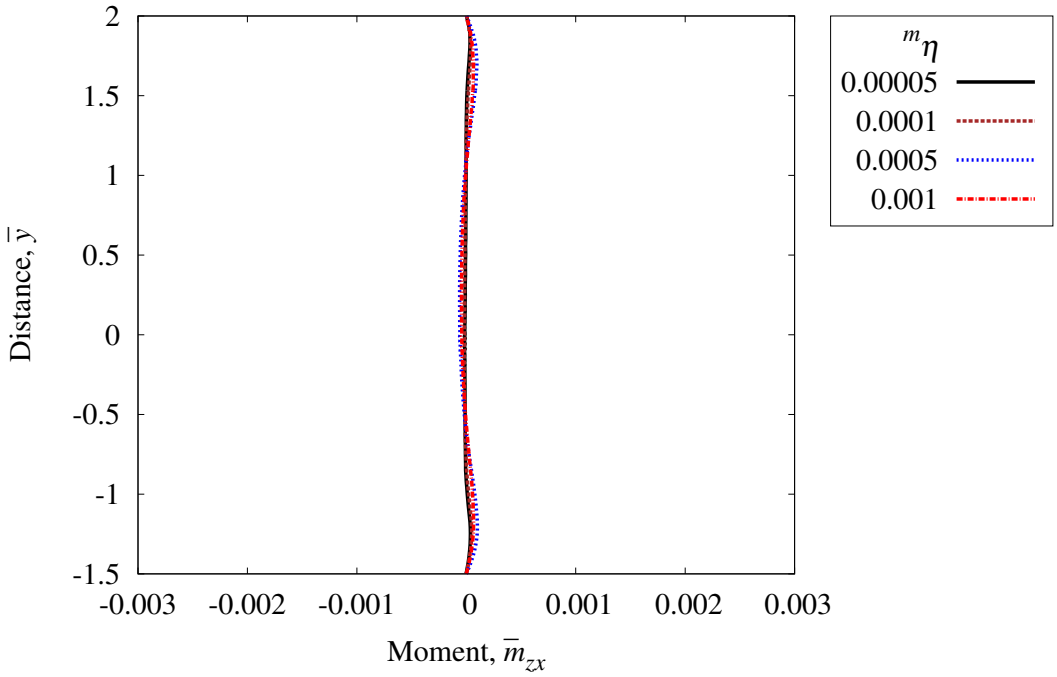

Figure 3.42: Cauchy moment $\bar{m}_{zx}$ versus distance $\bar{y}$ at $\bar{x} = 50.8$; ER = 3.5 : 2

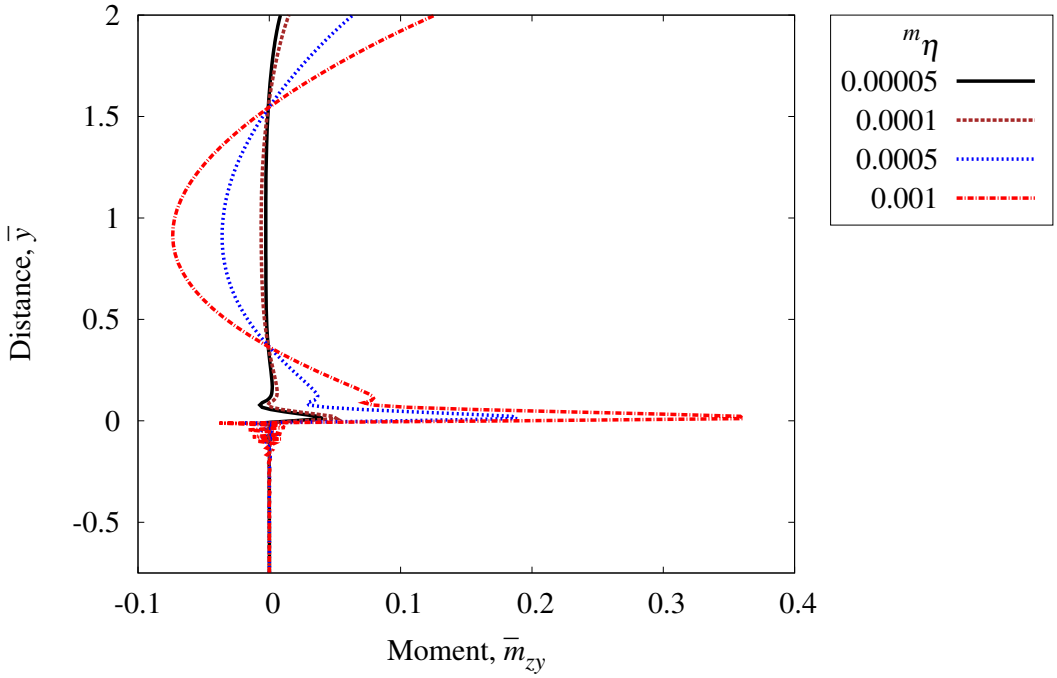

Figure 3.43: Cauchy moment $\bar{m}_{zy}$ versus distance $\bar{y}$ at $\bar{x} = 0.0$; ER = 2.75 : 2

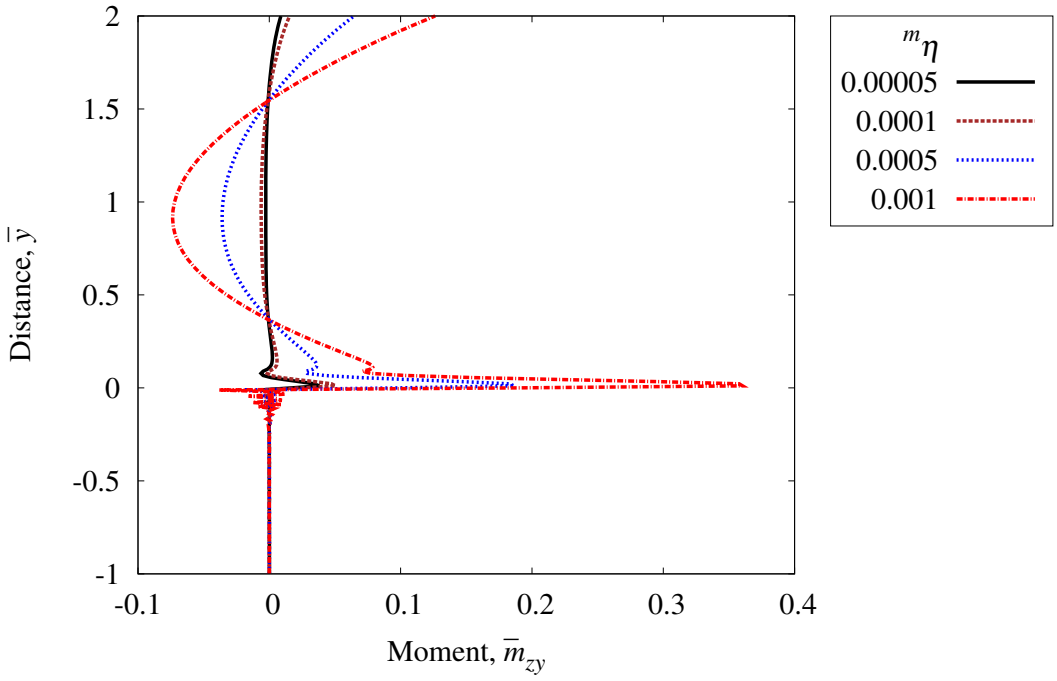

Figure 3.44: Cauchy moment $\bar{m}_{zy}$ versus distance $\bar{y}$ at $\bar{x} = 0.0$; ER = 3 : 2

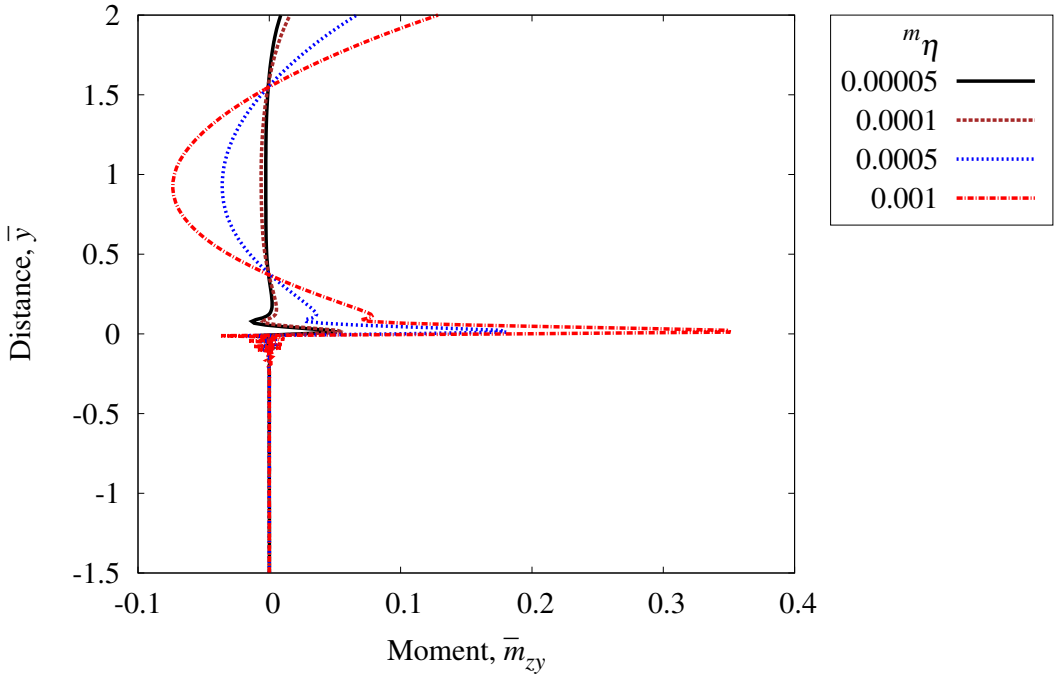

Figure 3.45: Cauchy moment $\bar{m}_{zy}$ versus distance $\bar{y}$ at $\bar{x} = 0.0$; ER = 3.5 : 2

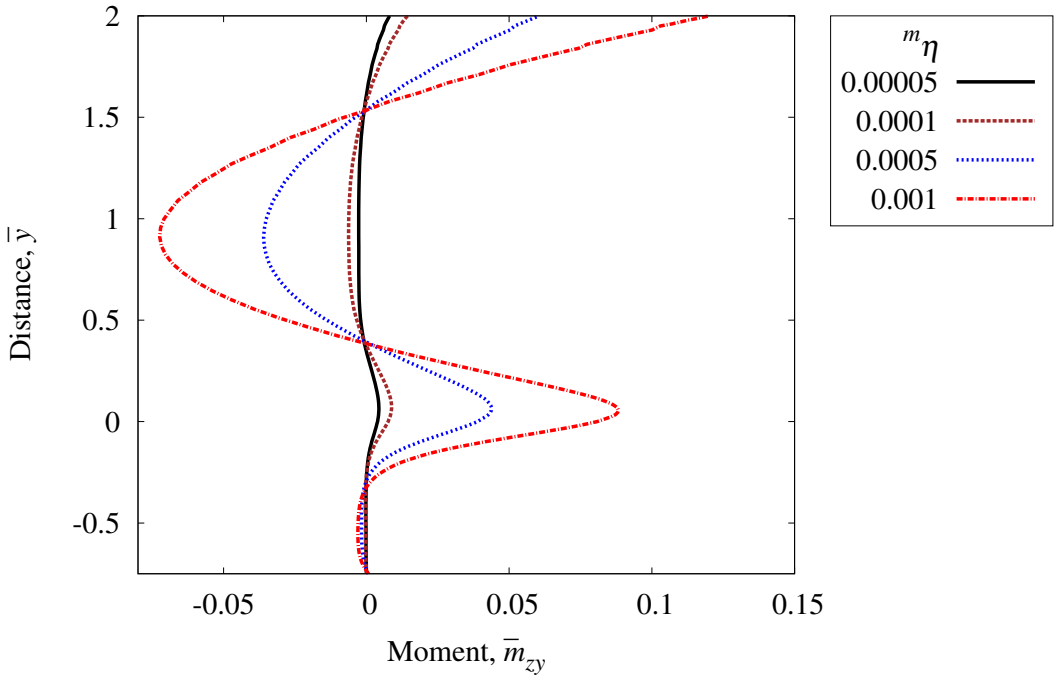

Figure 3.46: Cauchy moment $\bar{m}_{zy}$ versus distance $\bar{y}$ at $\bar{x} = 0.2$; ER = 2.75 : 2

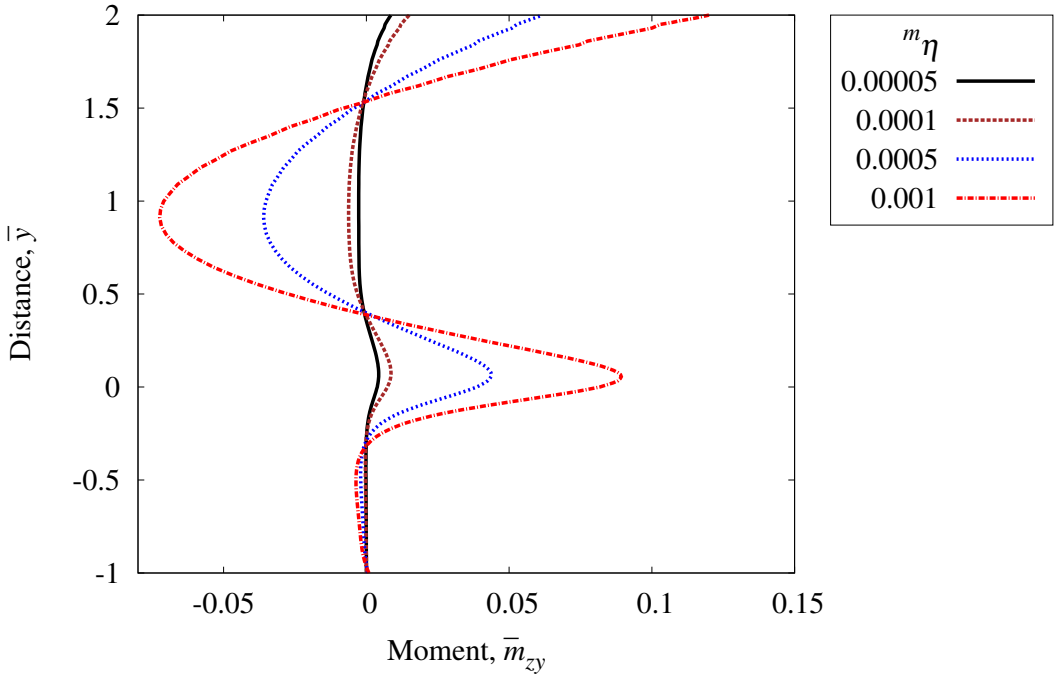

Figure 3.47: Cauchy moment $\bar{m}_{zy}$ versus distance $\bar{y}$ at $\bar{x} = 0.2$; ER = 3 : 2

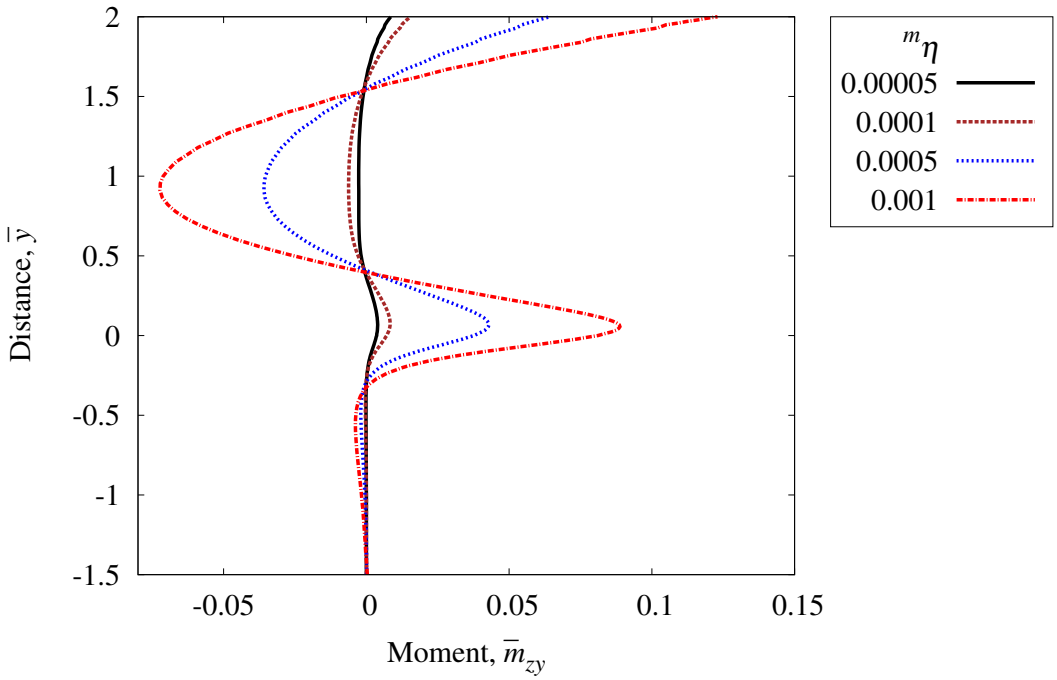

Figure 3.48: Cauchy moment $\bar{m}_{zy}$ versus distance $\bar{y}$ at $\bar{x} = 0.2$; ER = 3.5 : 2

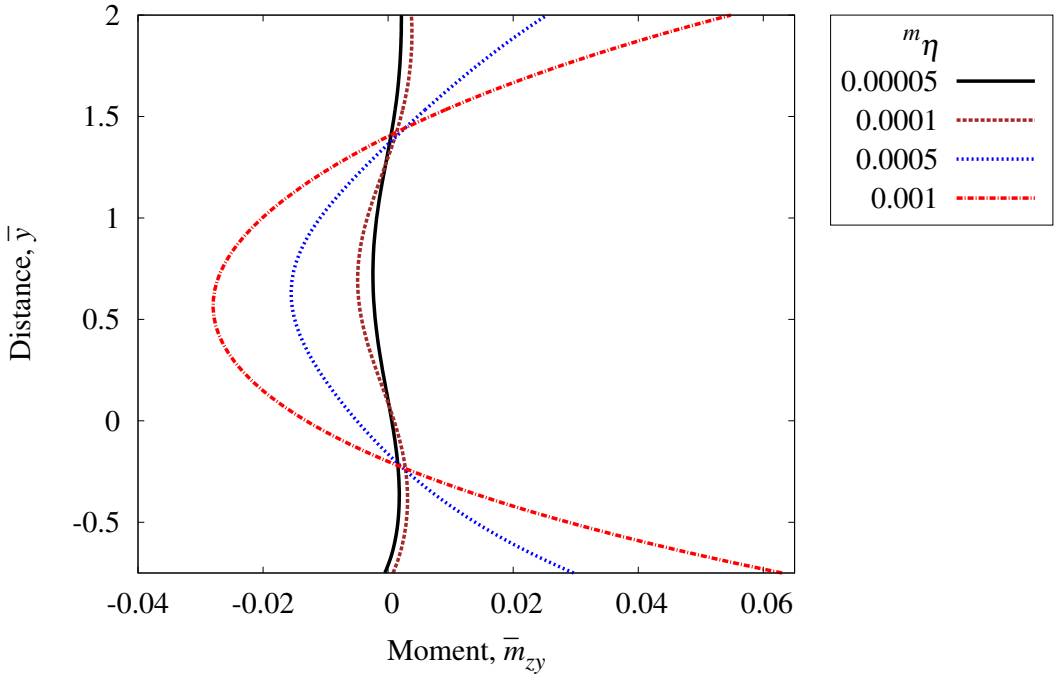

Figure 3.49: Cauchy moment $\bar{m}_{zy}$ versus distance $\bar{y}$ at $\bar{x} = 5.0$; ER = 2.75 : 2

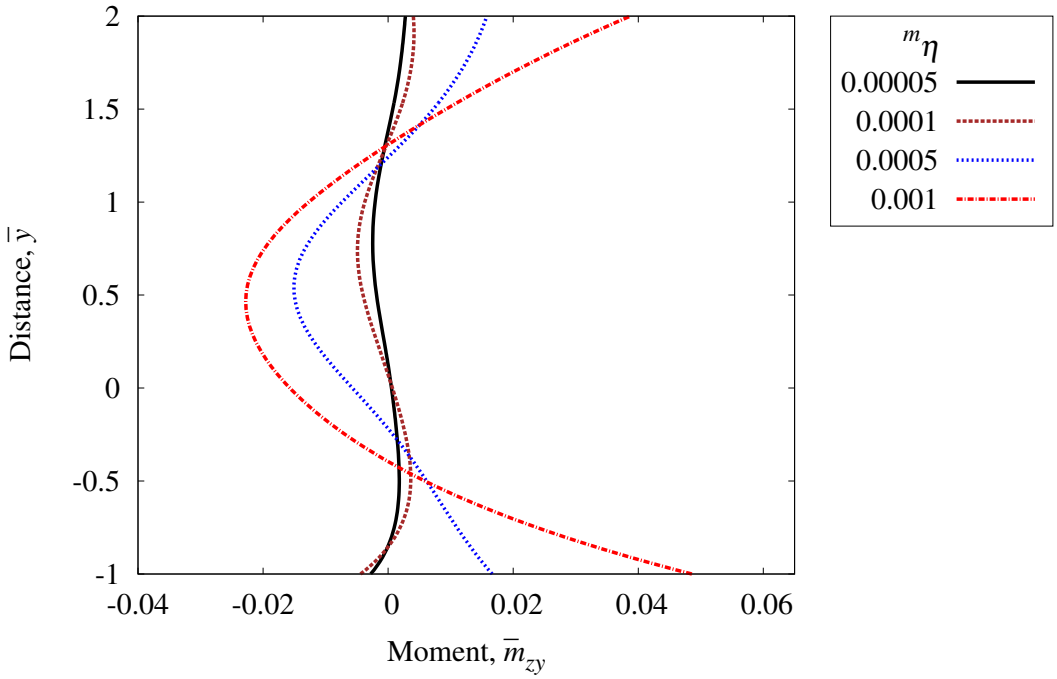

Figure 3.50: Cauchy moment $\bar{m}_{zy}$ versus distance $\bar{y}$ at $\bar{x} = 5.0$; ER = 3 : 2

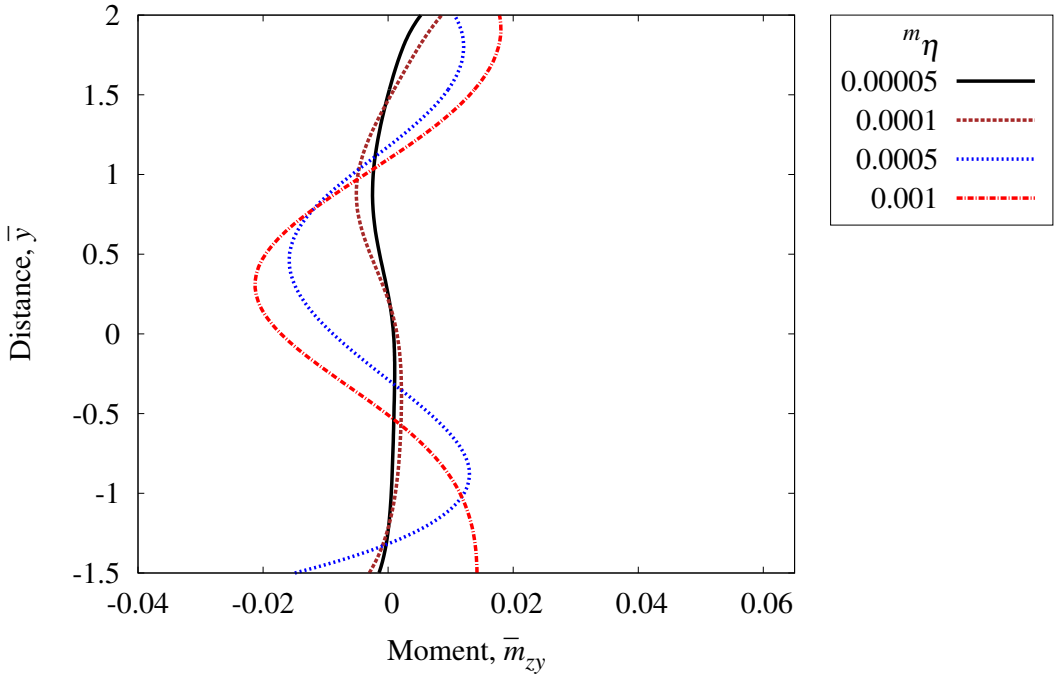

Figure 3.51: Cauchy moment $\bar{m}_{zy}$ versus distance $\bar{y}$ at $\bar{x}$ = 5.0 ; ER = 3.5 : 2

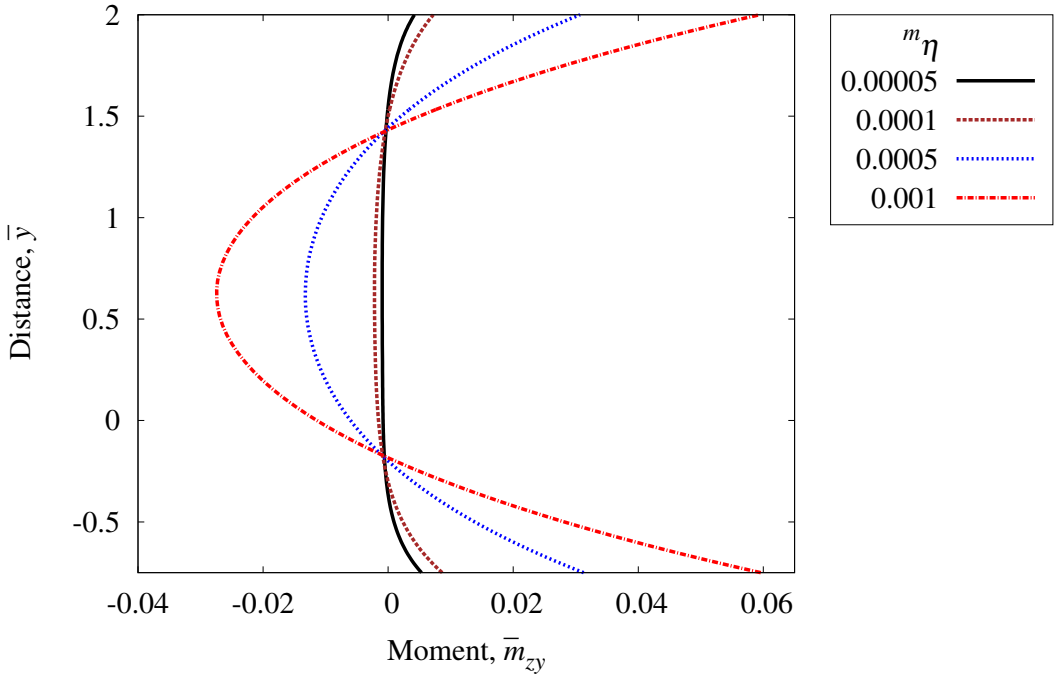

Figure 3.52: Cauchy moment $\bar{m}_{zy}$ versus distance $\bar{y}$ at $\bar{x}$ = 50.8 ; ER = 2.75 : 2

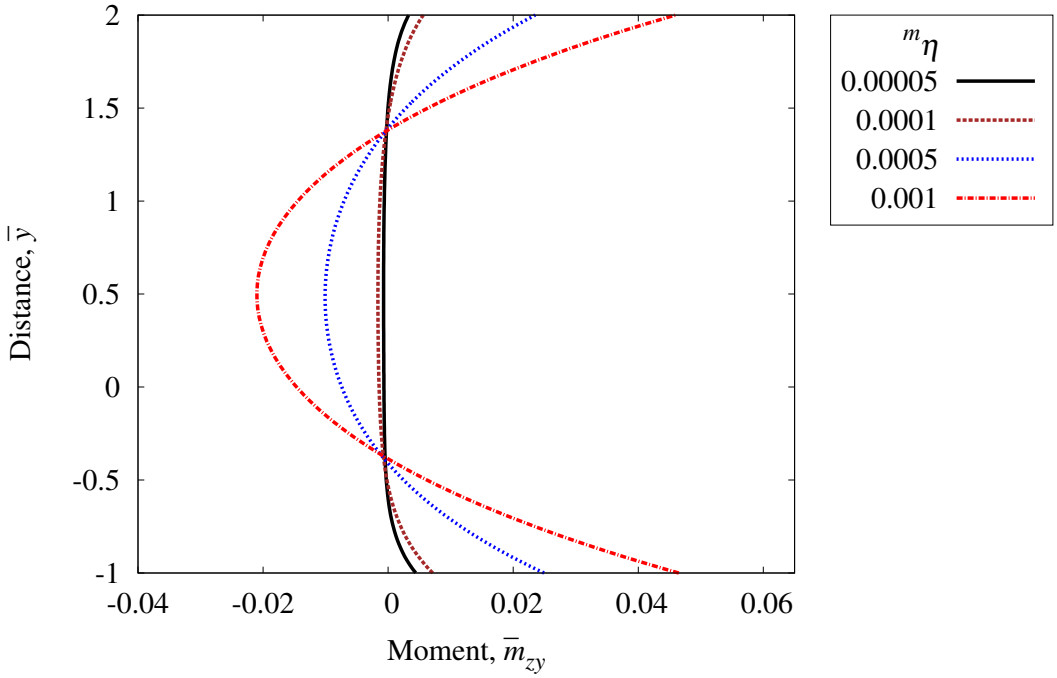

Figure 3.53: Cauchy moment $\bar{m}_{zy}$ versus distance $\bar{y}$ at $\bar{x} = 50.8$; ER = 3 : 2

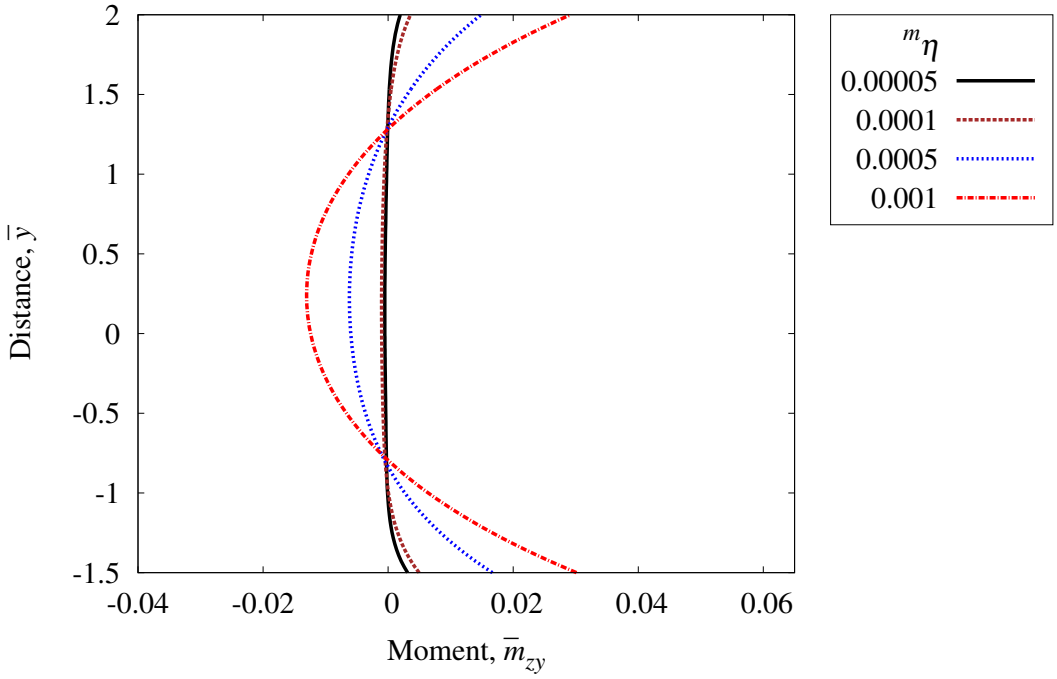

Figure 3.54: Cauchy moment $\bar{m}_{zy}$ versus distance $\bar{y}$ at $\bar{x} = 50.8$; ER = 3.5 : 2

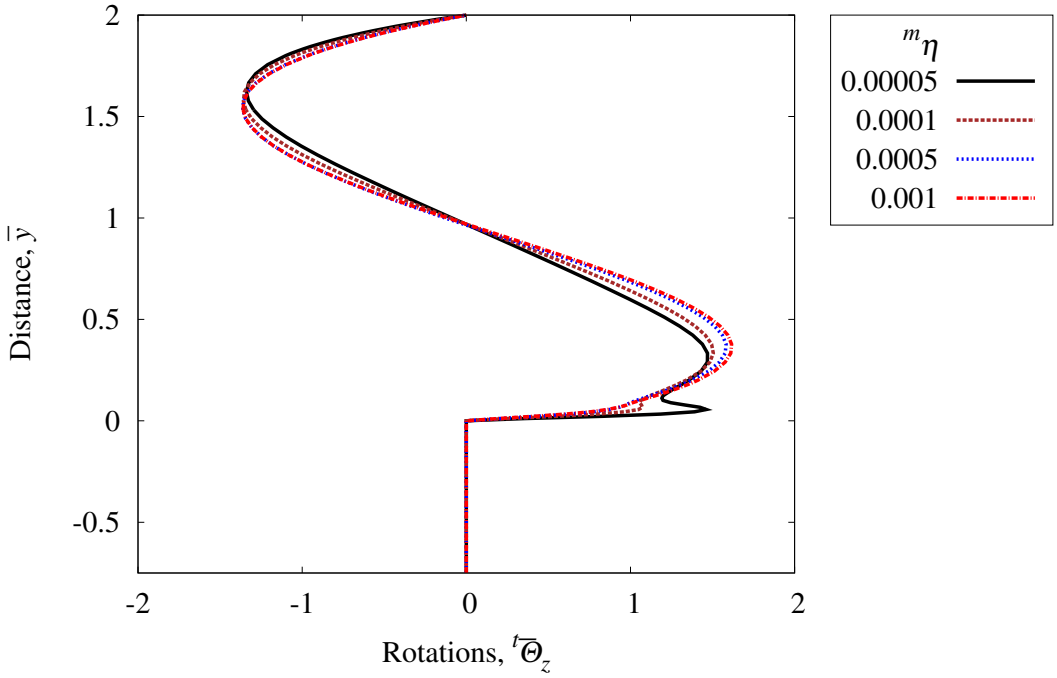

Figure 3.55: Rotation rate ${}^{t}\overline{\Theta}_{z}$ versus distance $\overline{y}$ at $\overline{x} = 0.0$; ER = 2.75 : 2

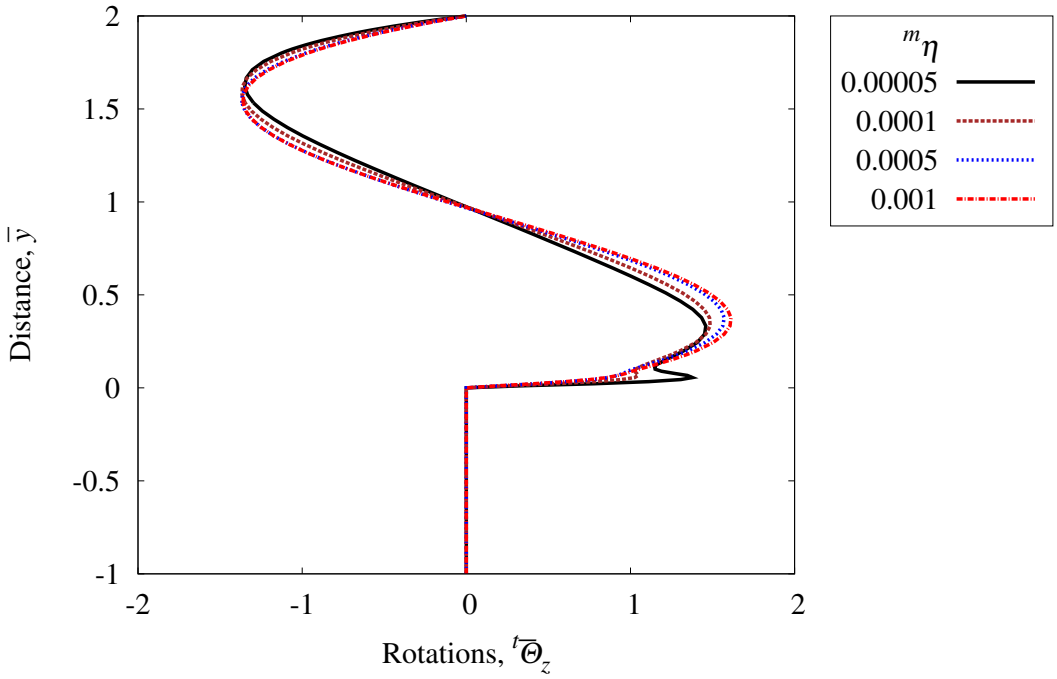

Figure 3.56: Rotation rate ${}^{t}\overline{\Theta}_{z}$ versus distance $\overline{y}$ at $\overline{x} = 0.0$; ER = 3 : 2

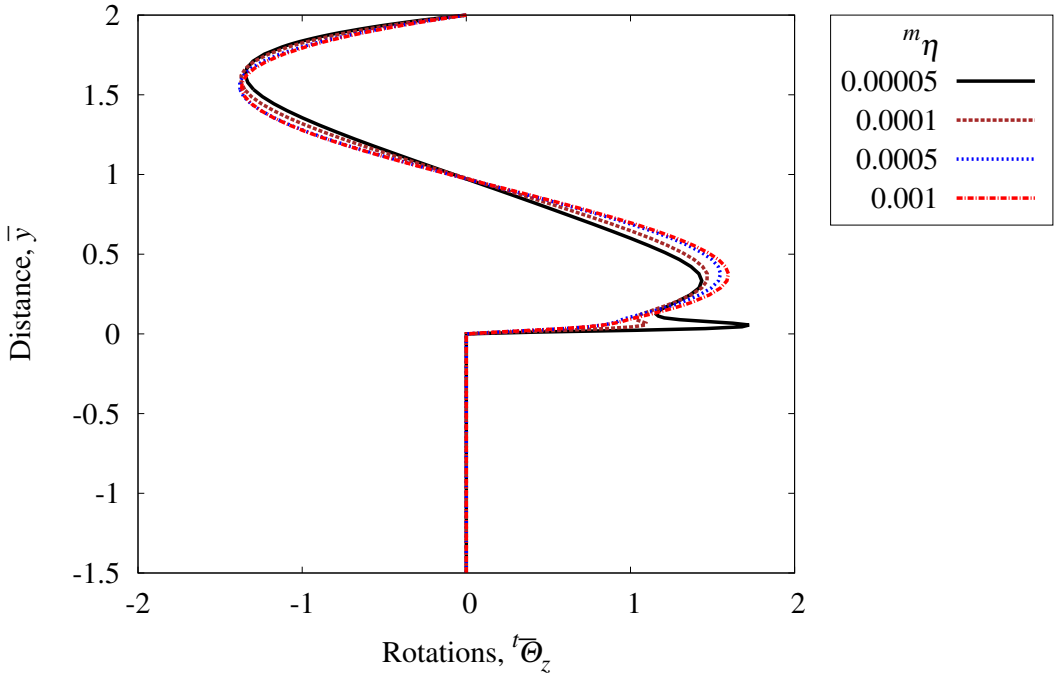

Figure 3.57: Rotation rate ${}^{t}\overline{\Theta}_{z}$ versus distance $\overline{y}$ at $\overline{x} = 0.0$; ER = 3.5 : 2

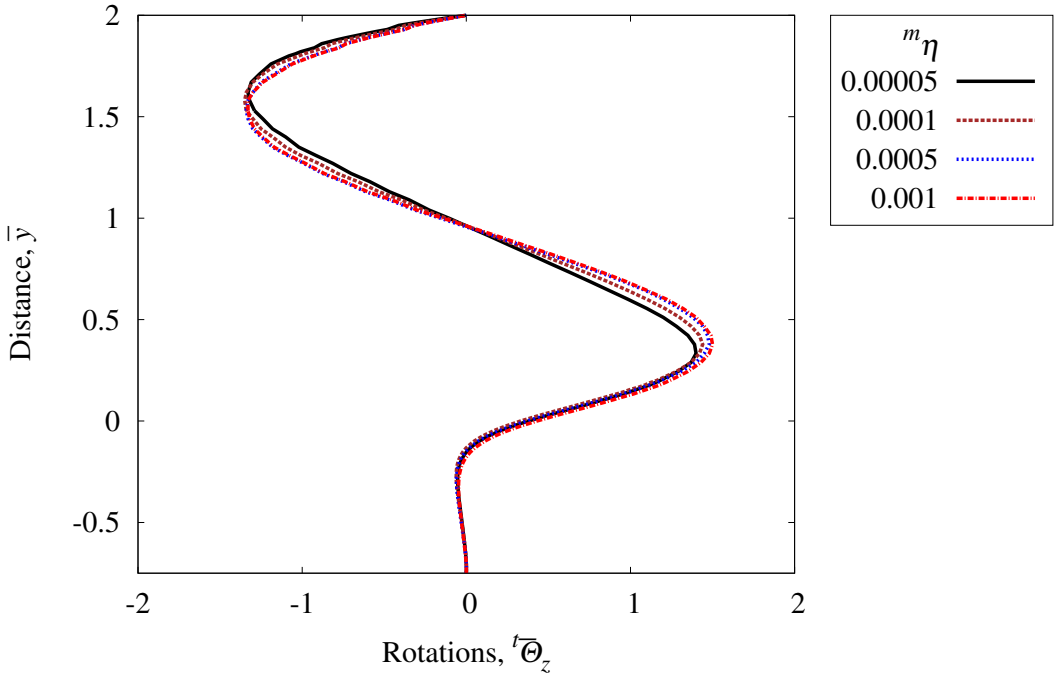

Figure 3.58: Rotation rate ${}^{t}\overline{\Theta}_{z}$ versus distance $\overline{y}$ at $\overline{x} = 0.2$; ER = 2.75 : 2

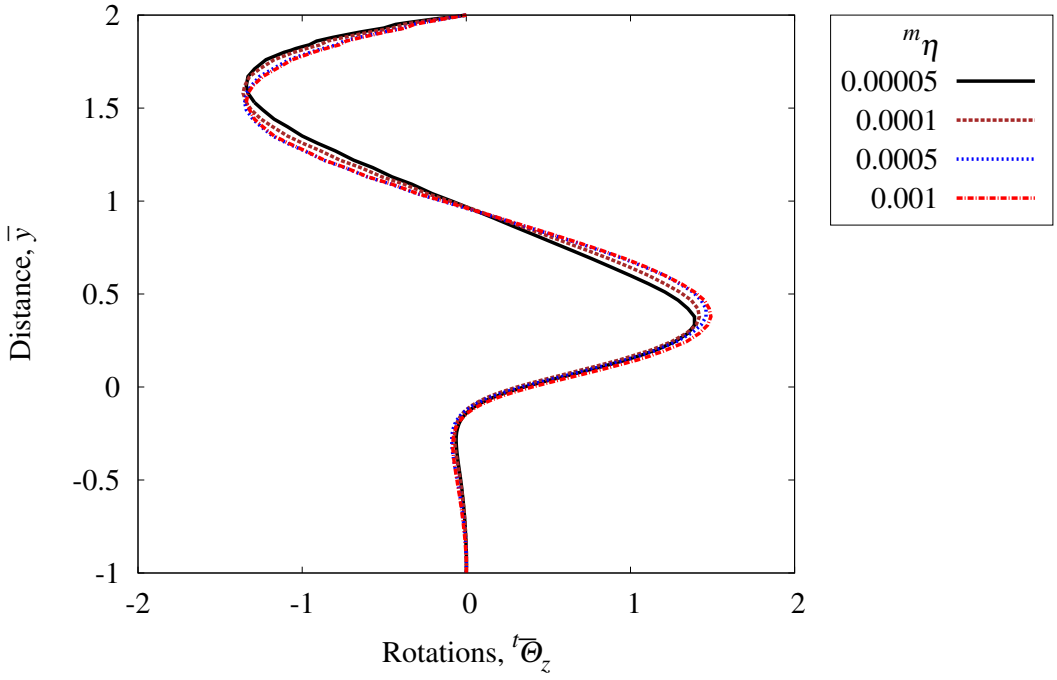

Figure 3.59: Rotation rate ${}^{t}\overline{\Theta}_{z}$ versus distance $\bar{y}$ at $\bar{x} = 0.2$; ER = 3 : 2

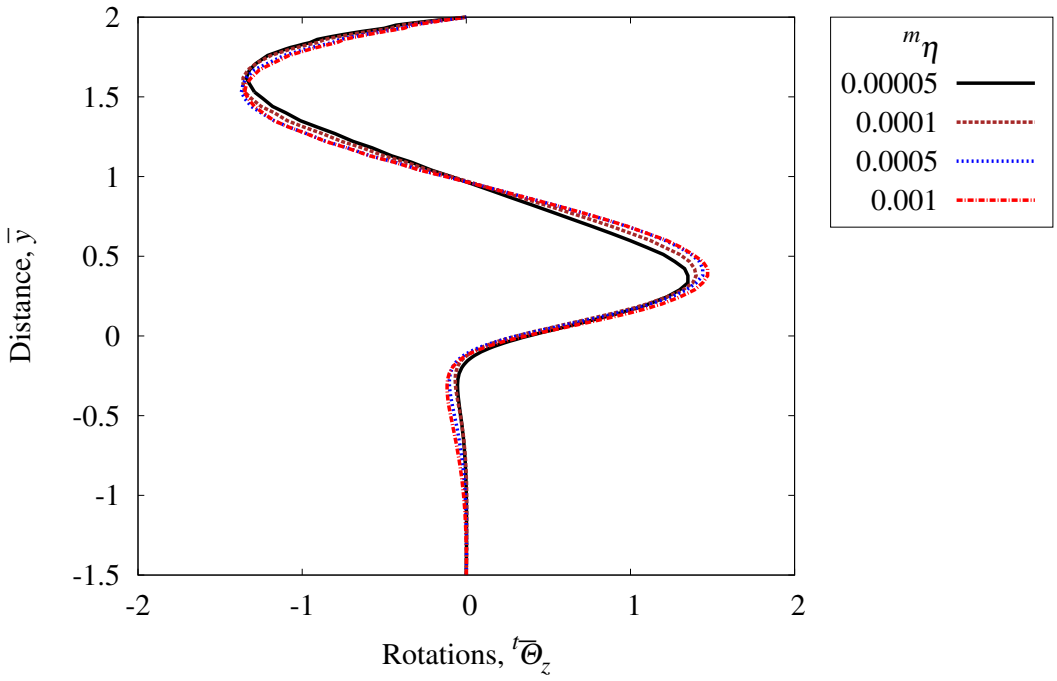

Figure 3.60: Rotation rate ${}^{t}\overline{\Theta}_{z}$ versus distance $\bar{y}$ at $\bar{x} = 0.2$; ER = 3.5 : 2

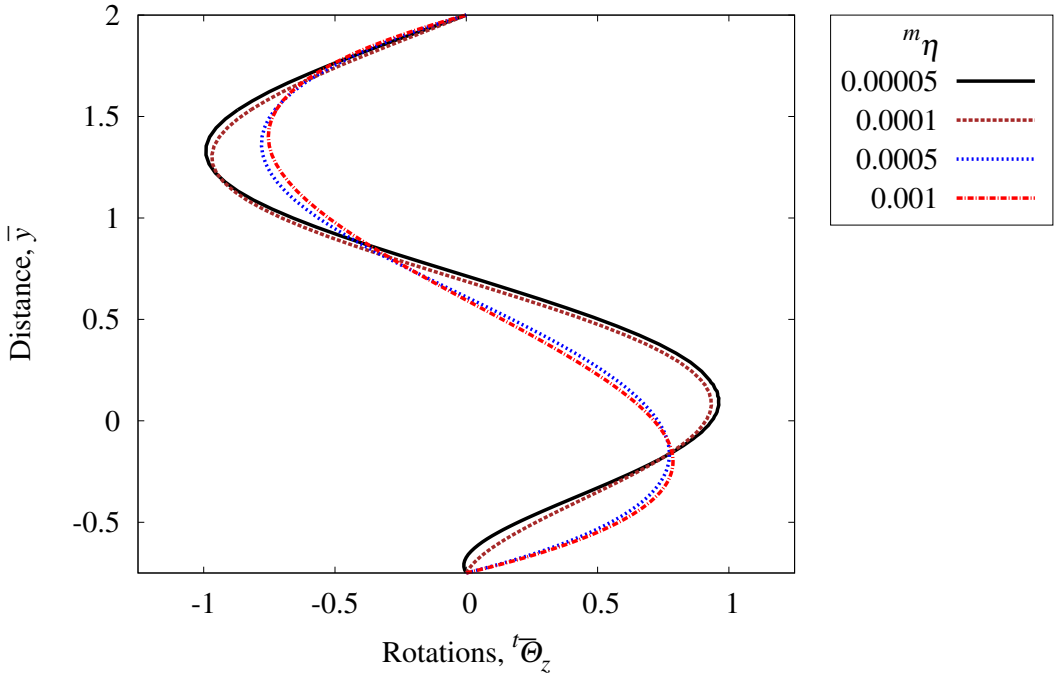

Figure 3.61: Rotation rate ${}^{t}\overline{\Theta}_z$ versus distance $\bar{y}$ at $\bar{x}$ = 5.0 ; ER = 2.75 : 2

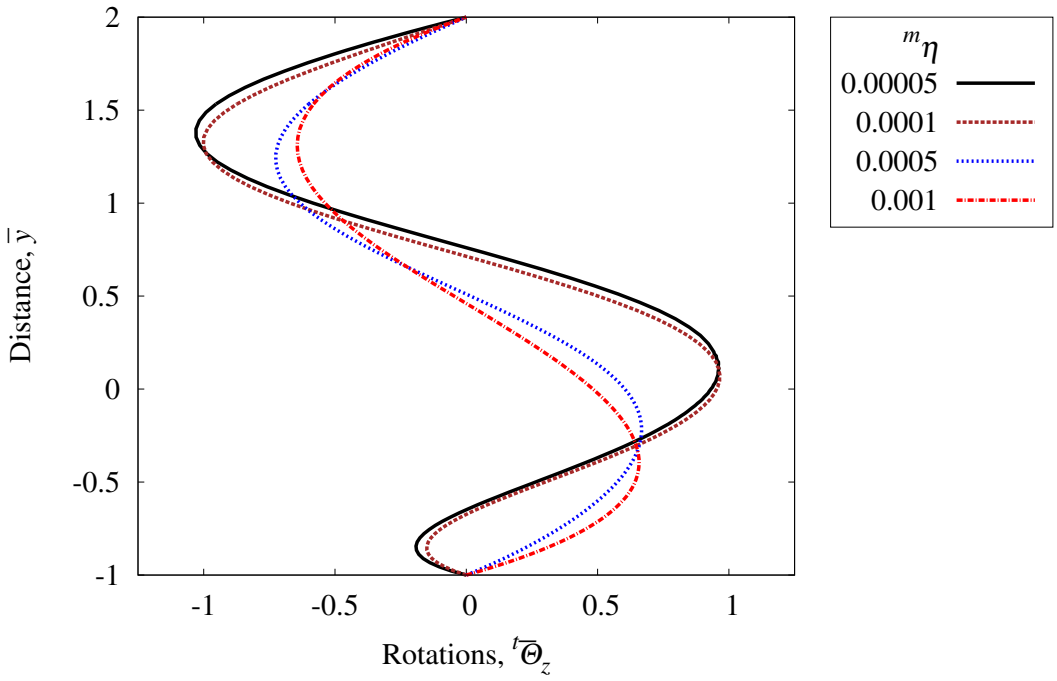

Figure 3.62: Rotation rate ${}^{t}\overline{\Theta}_z$ versus distance $\bar{y}$ at $\bar{x}$ = 5.0 ; ER = 3 : 2

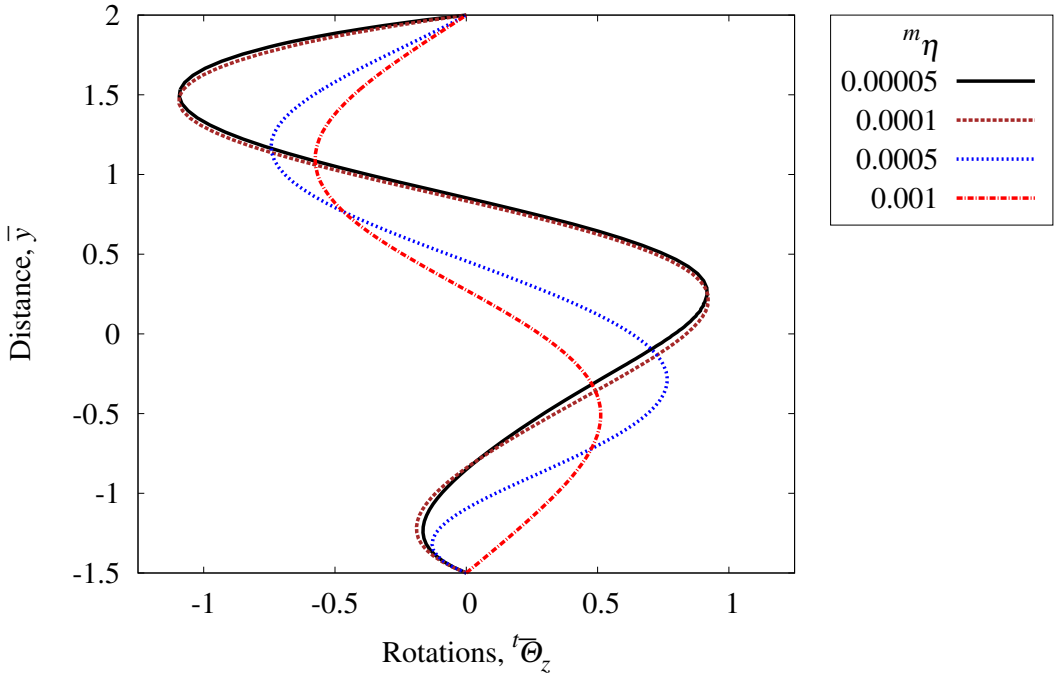

Figure 3.63: Rotation rate ${}^{t}\bar{\Theta}_z$ versus distance $\bar{y}$ at $\bar{x}$ = 5.0 ; ER = 3.5 : 2

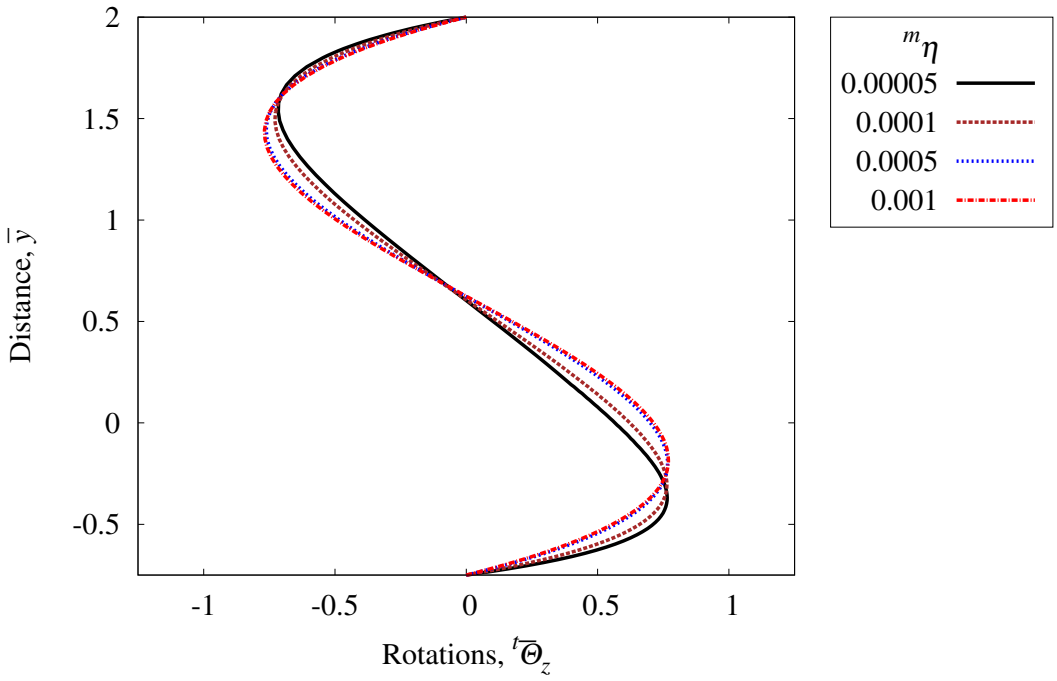

Figure 3.64: Rotation rate ${}^{t}\bar{\Theta}_z$ versus distance $\bar{y}$ at $\bar{x}$ = 50.8 ; ER = 2.75 : 2

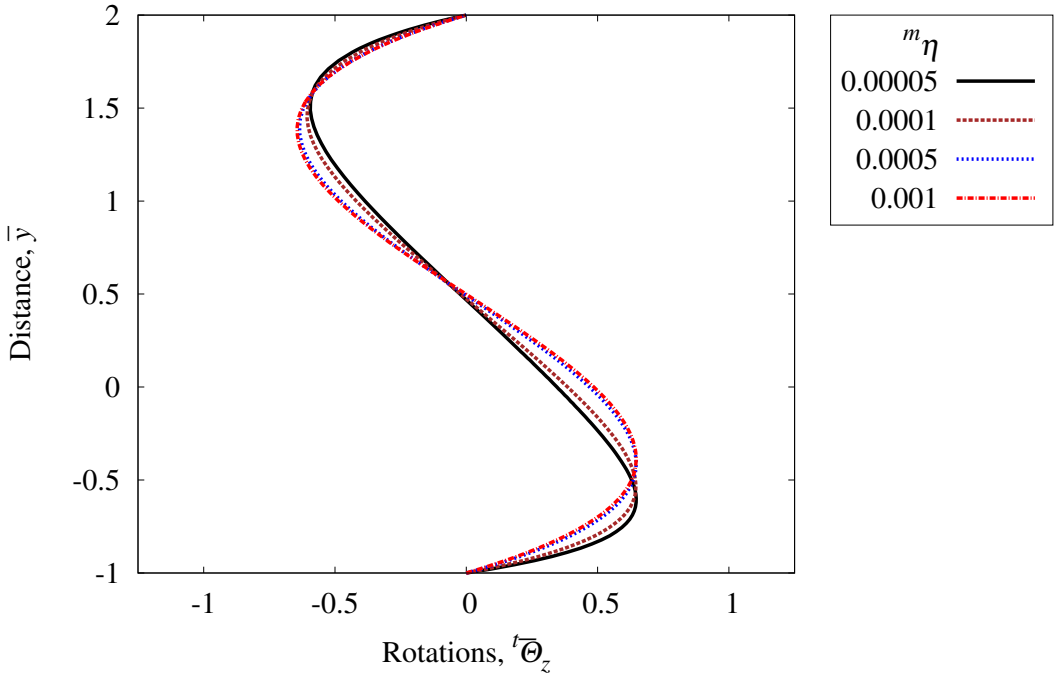

Figure 3.65: Rotation rate ${}^{t}\overline{\Theta}_z$ versus distance $\bar{y}$ at $\bar{x}$ = 50.8 ; ER = 3 : 2

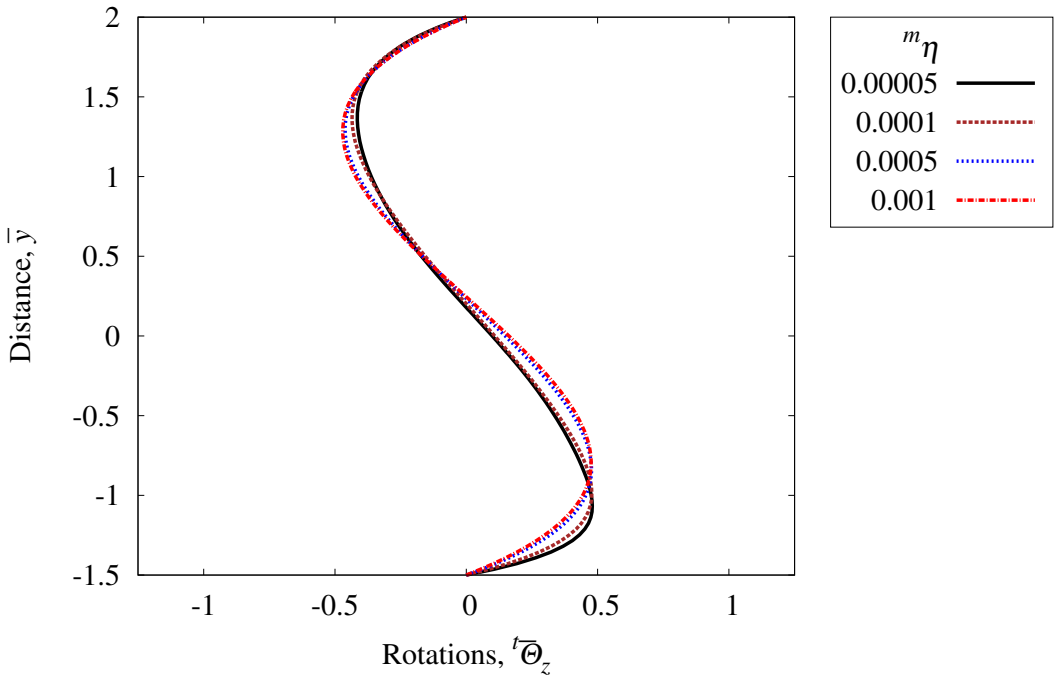

Figure 3.66: Rotation rate ${}^{t}\overline{\Theta}_z$ versus distance $\bar{y}$ at $\bar{x}$ = 50.8 ; ER = 3.5 : 2

Graphs of ${}^{t}\overline{\Theta}_z$ versus $\bar{y}$ at $\bar{x} = 0.0$ and 0.2 for expansion ratio of 2.75 : 2 are shown in figures 3.55 and 3.58. We note nonzero ${}^{t}\overline{\Theta}_z$ for Newtonian fluid but is not considered in the derivation of the conservation and balance laws based on classical continuum mechanics. Increasing ${}^{m}\eta$ values have very little effect on ${}^{t}\overline{\Theta}_z$ at $\bar{x} = 0.0$ and $\bar{x} = 0.2$ due to the insignificant change in the recirculation zone near the expansion point. Similar behavior is observed for the other two expansion ratios in figures 3.56 - 3.57 and 3.59 - 3.60. Plots of ${}^{t}\overline{\Theta}_z$ versus $\bar{y}$ at $\bar{x} = 5.0$ and 50.8 for the three expansion ratios are shown in figures 3.61 - 3.63 and 3.64 - 3.66. At $\bar{x} = 5.0$ we notice pronounced ${}^{t}\overline{\Theta}_z$ even for ${}^{m}\eta = 0$ (Newtonian fluid) that varies significantly for increasing ${}^{m}\eta$ values. At outlet the influence of ${}^{m}\eta$ on ${}^{t}\overline{\Theta}_z$ is not as significant as at $\bar{x} = 5.0$.

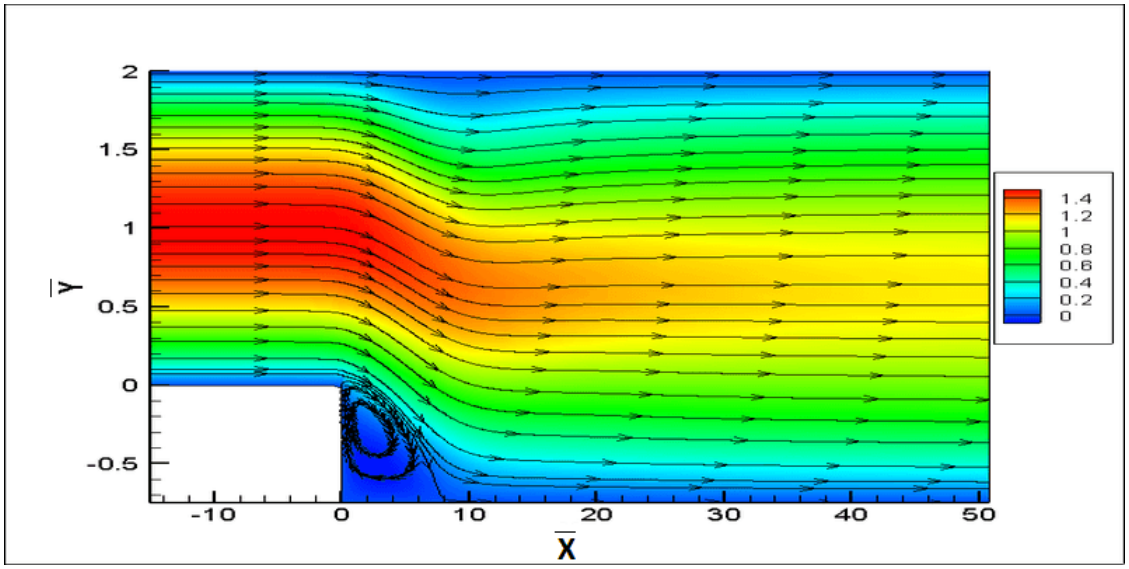

Figure 3.67: Streamline contour plots for ${}^{m}\eta = 0.0$; ER = 2.75 : 2

Figures 3.67 - 3.70 show plots of streamlines for ER of 2.75 : 2 for ${}^{m}\eta = 0$, 0.00005, 0.0005 and 0.001. With progressively increasing ${}^{m}\eta$ the size of recirculation region diminishes at ${}^{m}\eta = 0.001$ the recirculation region barely exists. Similar streamline plots for expansion ratios of 3 : 2 and 3.5 : 2 are shown in figures 3.71 - 3.74 and 3.75 - 3.78. We observe similar behavior as in case of ER of 2.75 : 2. In these studies with ER of 3 : 2 and 3.5 : 2 the recirculation size also diminishes with increasing ${}^{m}\eta$ and at ${}^{m}\eta = 0.001$, the recirculation zone is quite significant compared to ER of 2.75 : 2. With increasing ER, the recirculation zone size obviously increases. This holds for every value of ${}^{m}\eta$ considered in this study.

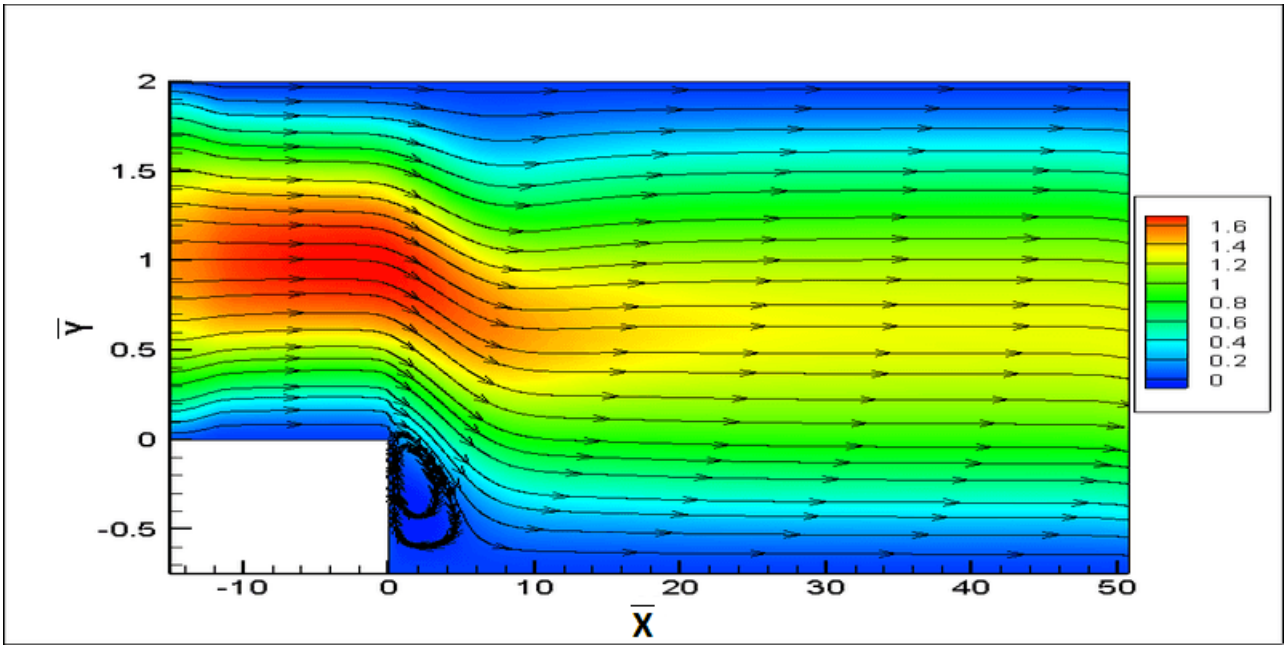

Figure 3.68: Streamline contour plots for ${}^{m}\eta$ = 0.00005 ; ER = 2.75 : 2

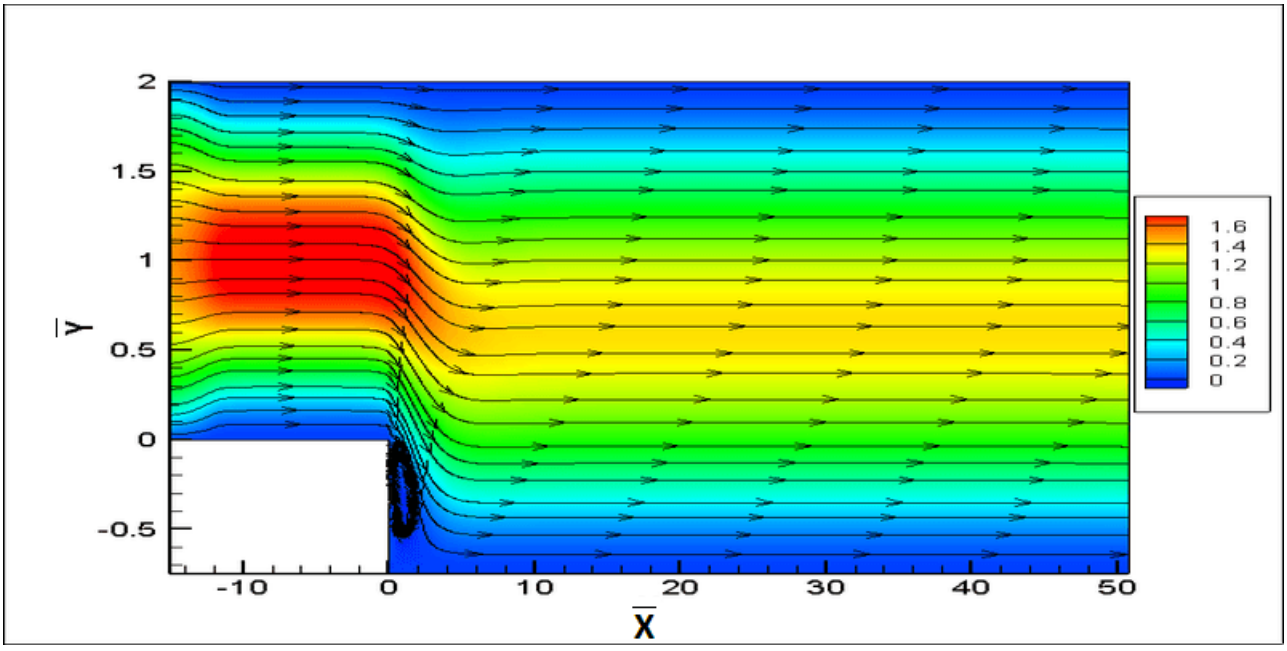

Figure 3.69: Streamline contour plots for ${}^{m}\eta$ = 0.0005 ; ER = 2.75 : 2

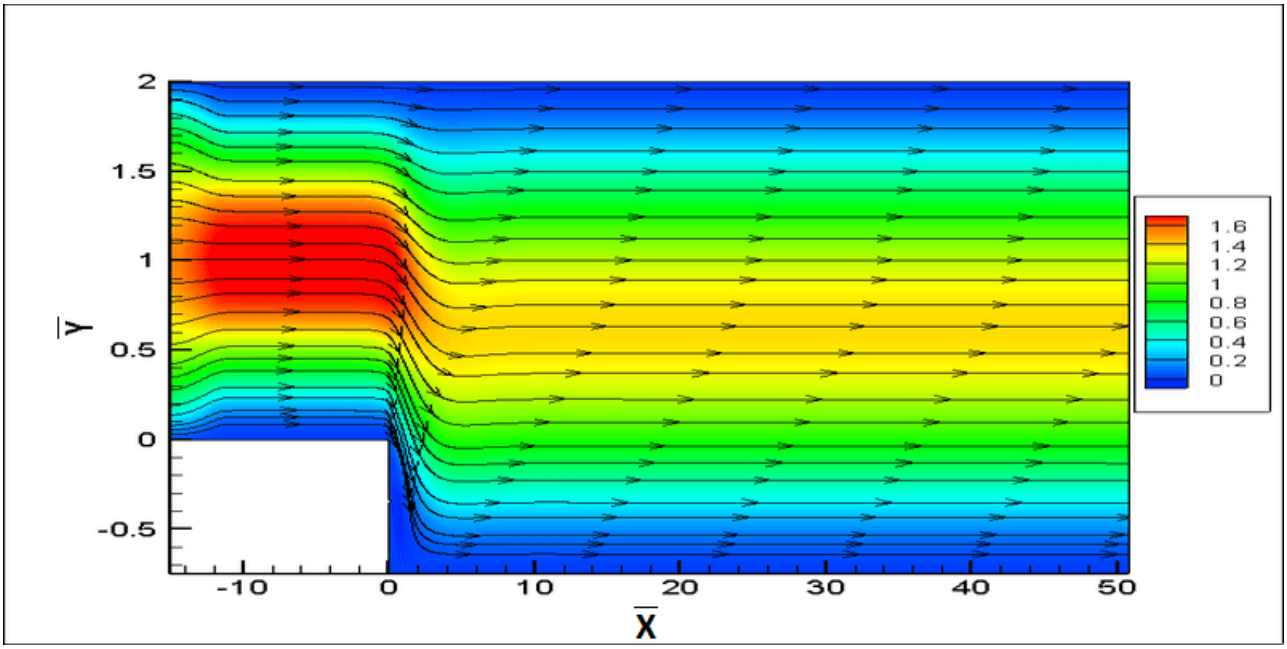

Figure 3.70: Streamline contour plots for $^{m}\eta$ = 0.001 ; ER = 2.75 : 2

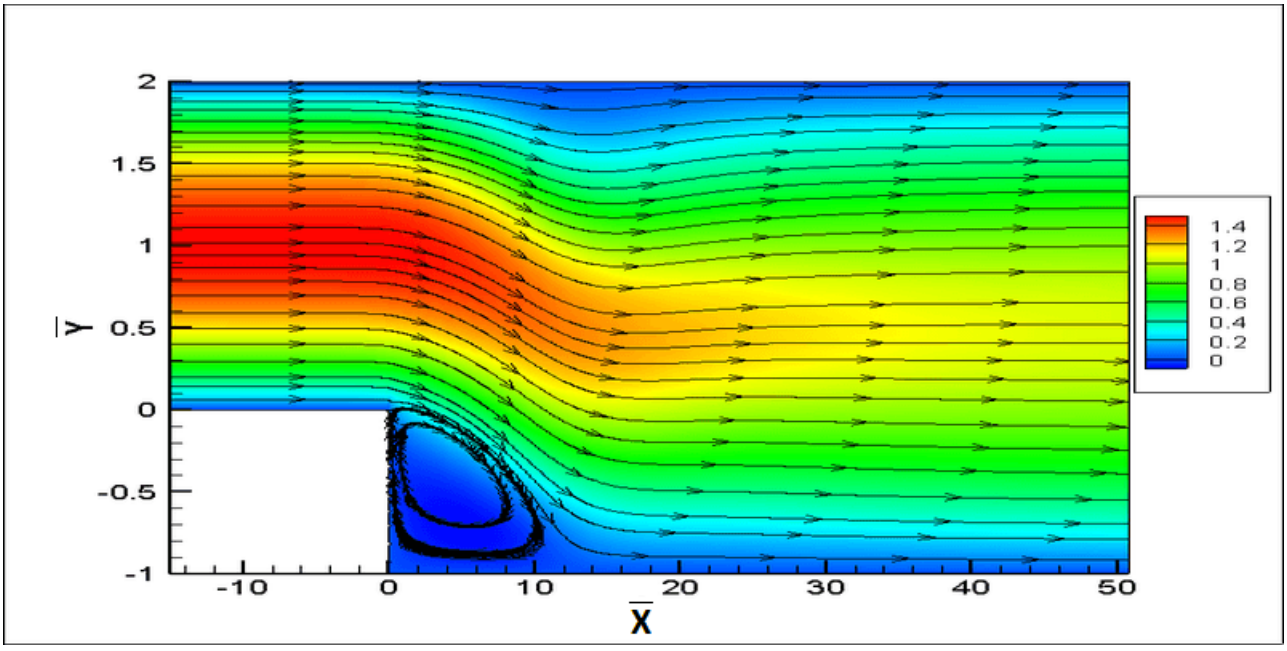

Figure 3.71: Streamline contour plots for $^{m}\eta$ = 0.0 ; ER = 3 : 2

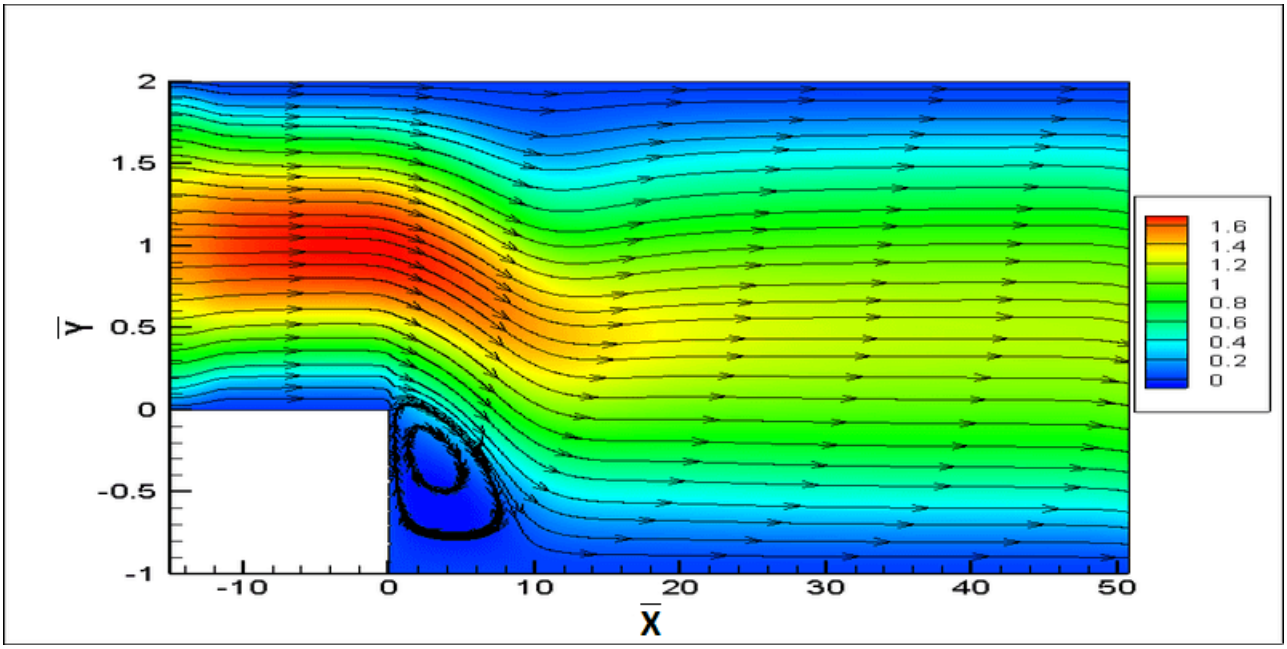

Figure 3.72: Streamline contour plots for ${}^{m}\eta$ = 0.00005 ; ER = 3 : 2

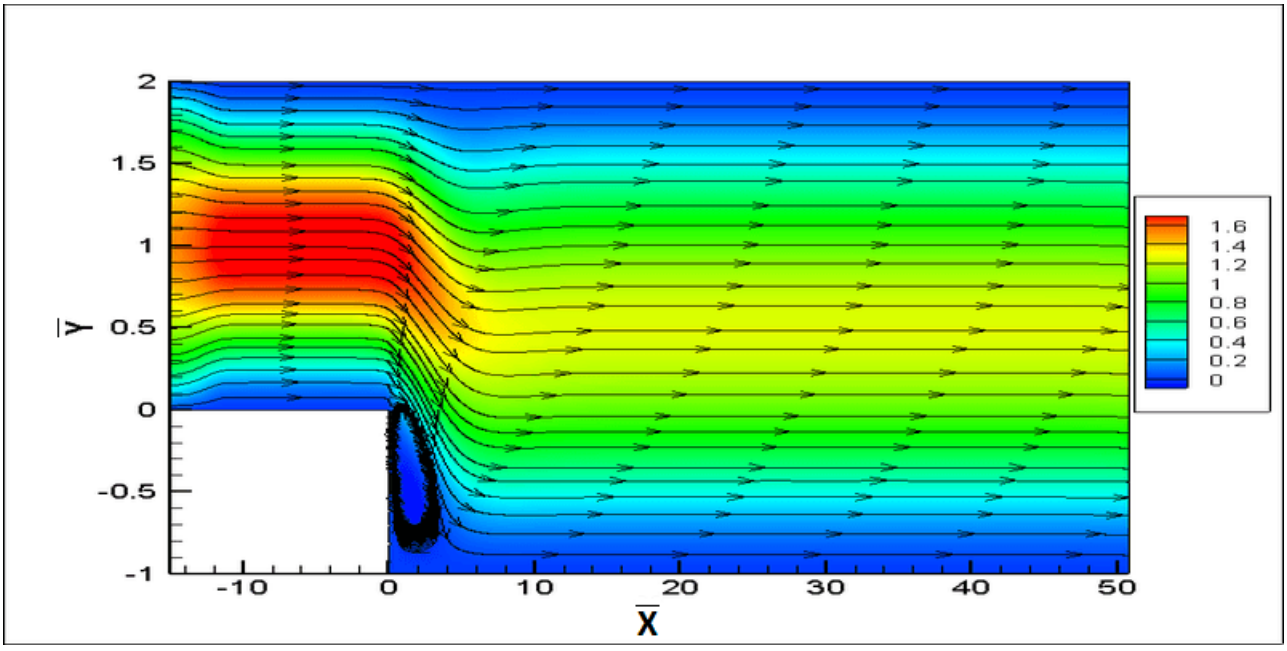

Figure 3.73: Streamline contour plots for ${}^{m}\eta$ = 0.0005 ; ER = 3 : 2

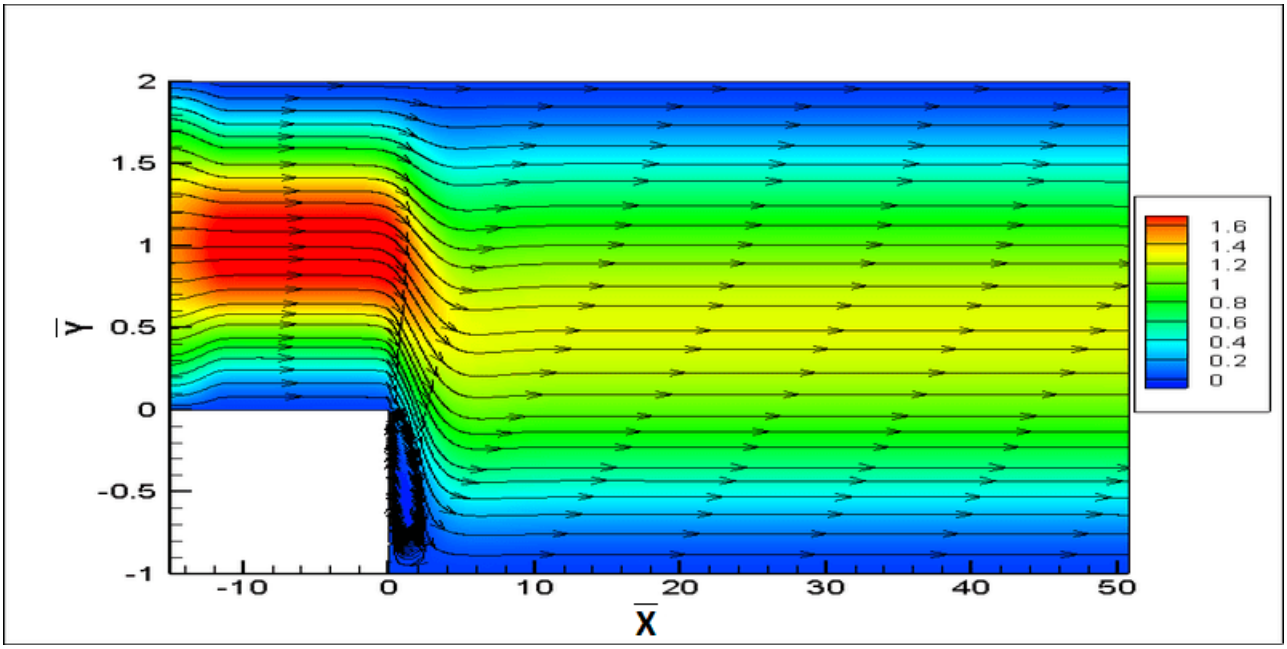

Figure 3.74: Streamline contour plots for ${}^{m}\eta$ = 0.001 ; ER = 3 : 2

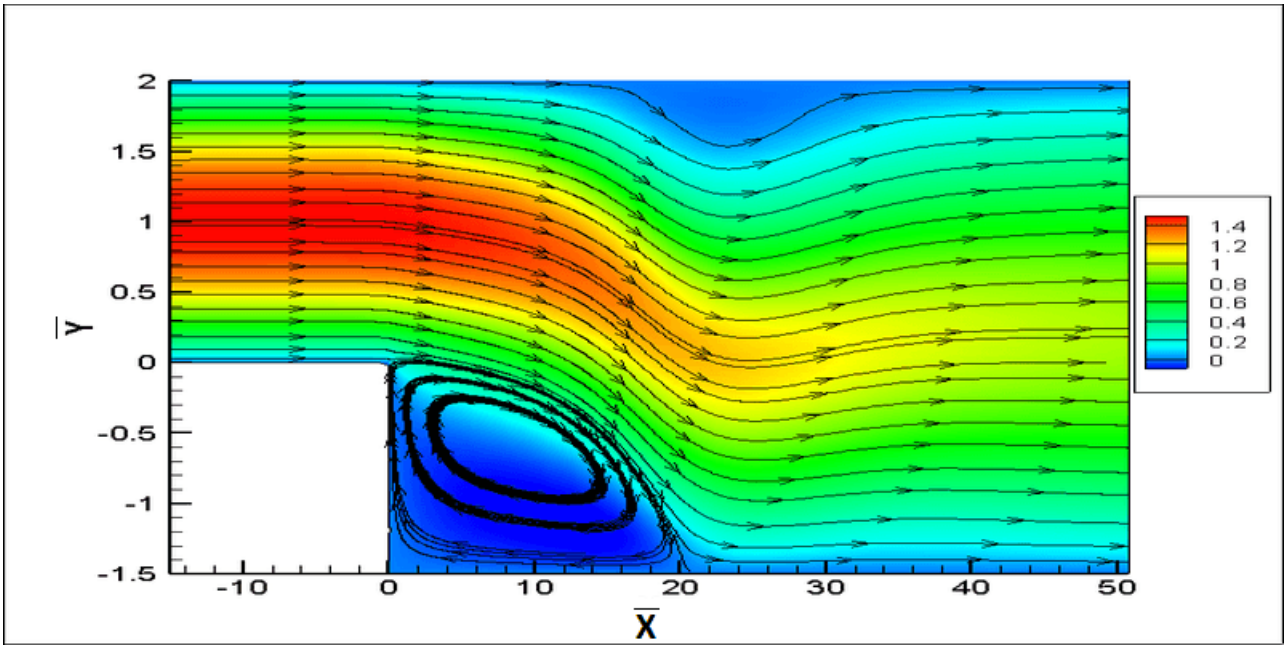

Figure 3.75: Streamline contour plots for ${}^{m}\eta$ = 0.0 ; ER = 3.5 : 2

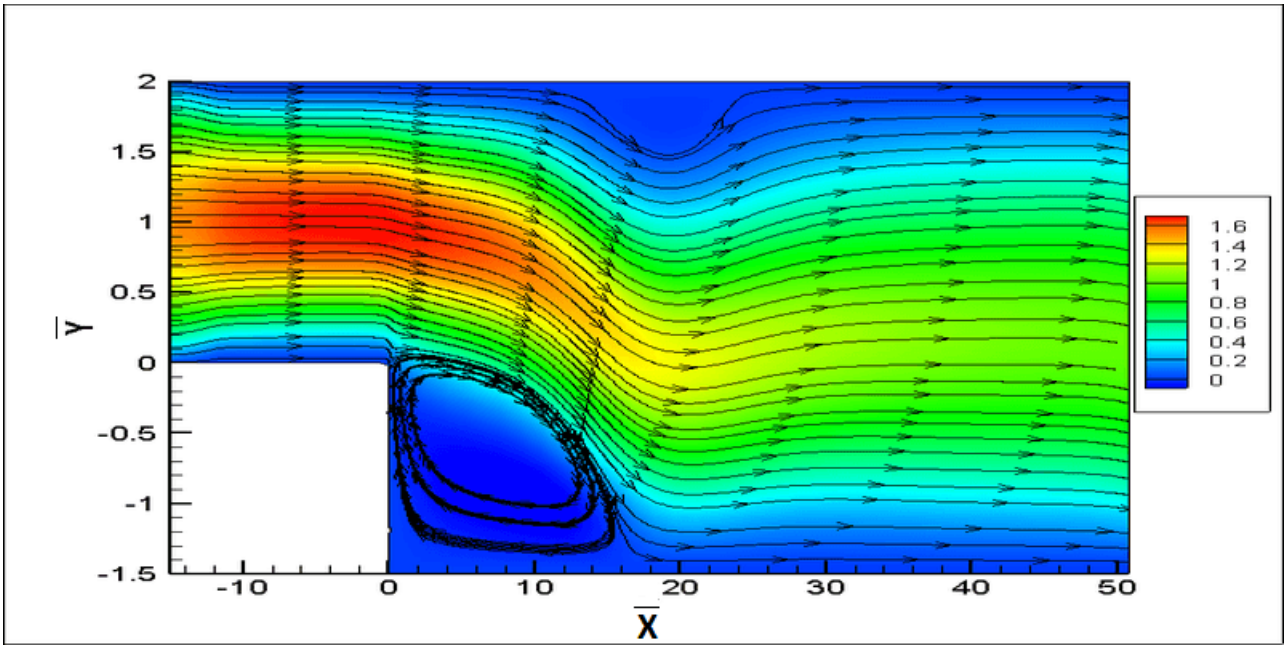

Figure 3.76: Streamline contour plots for ${}^{m}\eta$ = 0.00005 ; ER = 3.5 : 2

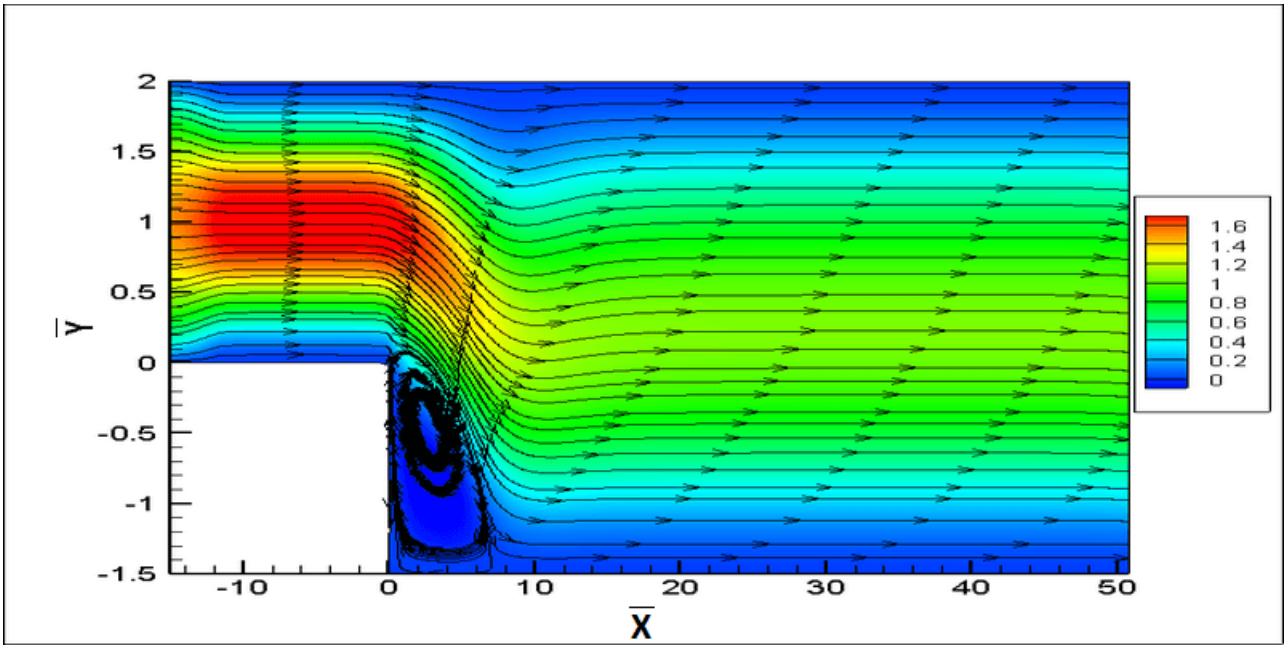

Figure 3.77: Streamline contour plots for ${}^{m}\eta$ = 0.0005 ; ER = 3.5 : 2

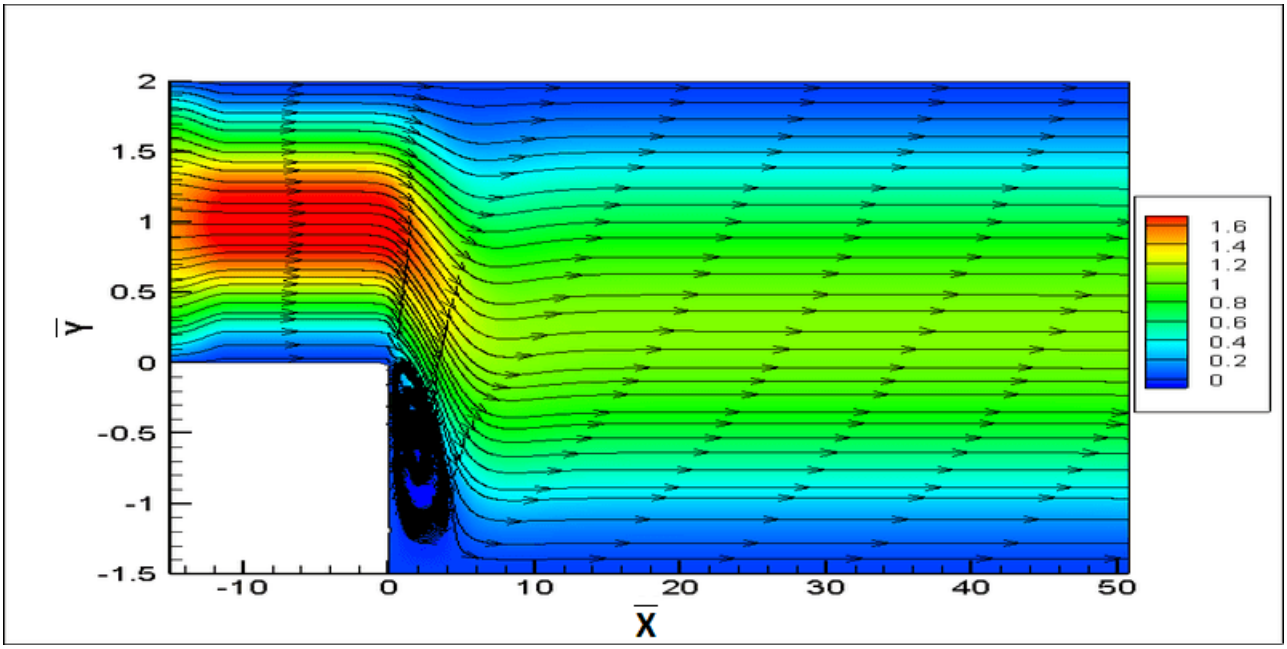

Figure 3.78: Streamline contour plots for ${}^{m}\eta$ = 0.001 ; ER = 3.5 : 2

3.4 Model problem III : Lid Driven Cavity

We consider a square and a rectangular lid driven cavity. The square cavity is 3 $cm \times 3$ cm. The dimensionless square cavity is 1×1 and the rectangular cavity is 1×2. Fluid properties and the reference quantities are given in the following.

$$\hat{\overline{\rho}} = 998.2\ kg/m^3 \quad , \quad \hat{\eta} = 1.002 \times 10^{-3}\ Pa$$

$$\rho_0 = 998.2\ kg/m^3 \quad , \quad \eta_0 = 1.002 \times 10^{-3}\ Pa$$

$$L_0 = 0.03\ m \quad , \quad u_0 = 0.03346\ m/s$$

which results in

$$\overline{\rho} = 1 \quad , \quad \eta = 1 \quad , \quad Re = \frac{\rho_0 L_0 u_0}{\eta_0} = 1000$$

3.4.1 Square Cavity

Fig 3.79 (a) shows a schematic of the 1×1 square cavity. Boundary conditions are shown in figure 3.79 (b). A 256 element graded discretization shown in figure 3.80, $\overline{h}_d$ of 0.0025 was arrived by starting with a coarse mesh of 36 element model and then systematically refining the mesh based on the values of the mean square error (MSE). At each stage, p-convergence of the mesh was examined and refinement was made in the areas containing elements with relatively high values of MSE. Accurate solutions were obtained using the 256 element mesh and increasing the number of elements beyond 256 did not significantly improve the results, hence provided sufficiently close approximation of constant lid velocity with $\overline{h}_d$ of 0.0025. Nine node p-version hierarchical finite elements are used in the discretization.

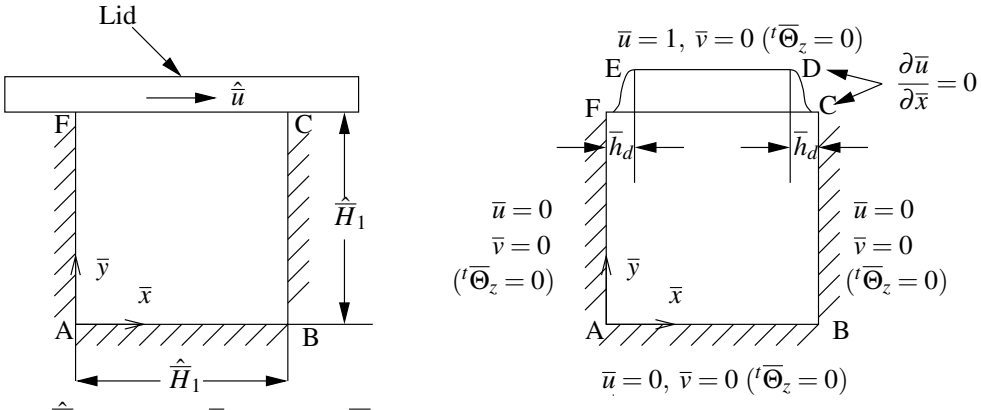

(a) Schematic of lid driven cavity

(b) Idealization of Lid Driven Cavity in (a), computational domain and boundary conditions

Figure 3.79: Schematic representation and computational domain of a square lid driven cavity

The p-level of 7 and k = 2 are used in all calculations. For this choice of k the integrals over $\overline{\Omega}^T$ are Riemann and the I values integrated sum of the squares of residuals over $\overline{\Omega}^T$ are of the order of $0(10^{-6})$ for the entire $\overline{\Omega}^T$. We present results at the vertical centerline ($\overline{x} = 0.5$) and at the horizontal centerline ($\overline{y} = 0.5$) of the cavity.

Figure 3.81 shows plots of $\overline{u}$ versus $\overline{y}$ at $\overline{x}$ = 0.5 for ${}^m\eta$ = 0.0 the Newtonian fluid, the calculated solution matches with [18]. Also for ${}^m\eta$ = 10^{-7} the deviation from Newtonian fluid is almost insignificant. When ${}^m\eta$ = 0.00001 or higher the boundary layer at the lid no longer exists,

which results in sudden change in the velocity $\overline{u}$. Progressively increasing values of ${}^{m}\eta$ offers progressively increasing resistance to the flow as a consequence the velocity $\overline{u}$ continues to reduce in magnitude along the entire length $0 \leq \overline{y} \leq 1$.

Side	Element Lengths						
$\overrightarrow{AF}$	0.0025	0.005	0.01	0.02	0.04	0.08	0.16
	0.1825	0.1825	0.16	0.08	0.04	0.02	0.01
	0.005	0.0025					
$\overrightarrow{AB}$	0.0025	0.005	0.01	0.02	0.04	0.08	0.16
	0.1825	0.1825	0.16	0.08	0.04	0.02	0.01
	0.005	0.0025					

Figure 3.80: 256 element discretization with $\overline{h}_d = 0.0025$ of a square lid driven cavity

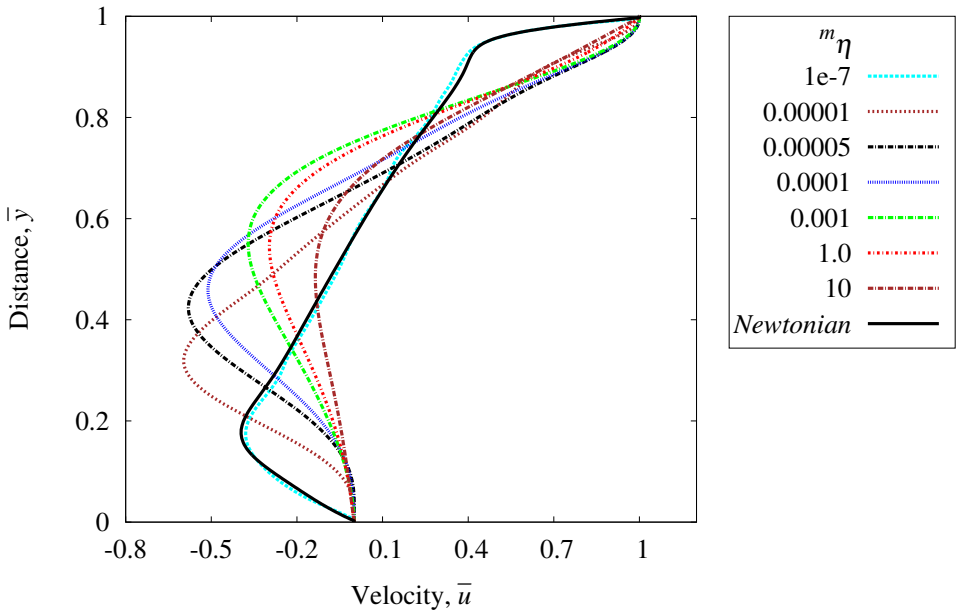

Figure 3.81: Velocity $\overline{u}$ versus distance $\overline{y}$ at $\overline{x} = 0.5$ of a square lid driven cavity

Figure 3.82 shows plots of $\overline{u}$ versus $\overline{x}$ at $\overline{y} = 0.5$ for progressively increasing values of ${}^{m}\eta$. Velocities $\overline{u}$ for ${}^{m}\eta = 0$ and ${}^{m}\eta = 10^{-7}$ are close to each other but for ${}^{m}\eta = 0.00001$ the boundary

layer no longer exists, hence a sudden change in $\overline{u}$. Thereafter the behavior of $\overline{u}$ at $\overline{y} = 0.5$ follows that of $\overline{u}$ at $\overline{x} = 0.5$. Graphs of $\overline{v}$ versus $\overline{y}$ at $\overline{x} = 0.5$ and $\overline{v}$ versus $\overline{x}$ at $\overline{y} = 0.5$ for various values of ${}^{m}\eta$ are shown in figures 3.83 and 3.84. We observe increasing resistance offered by the fluid for increasing values of ${}^{m}\eta$ resulting in progressively reduced velocity. Figures 3.85 and 3.86 show graphs of $\overline{m}_{zx}$ versus $\overline{y}$ at $\overline{x} = 0.5$ and $\overline{m}_{zx}$ versus $\overline{x}$ at $\overline{y} = 0.5$. Similar plots of $\overline{m}_{zy}$ are shown in figures 3.87 and 3.88. We clearly observe increasing magnitudes of $\overline{m}_{zx}$ and $\overline{m}_{zy}$ with increasing ${}^{m}\eta$ due to increased resistance offered by the fluid. Figures 3.89 and 3.90 show plots of ${}^{t}\overline{\Theta}_{z}$ versus $\overline{y}$ at $\overline{x} = 0.5$ and ${}^{t}\overline{\Theta}_{z}$ versus $\overline{x}$ at $\overline{y} = 0.5$. From figure 3.89 (a) we observe increasing magnitudes of ${}^{t}\overline{\Theta}_{z}$ in the active part of the cavity (top position) for smaller values of ${}^{m}\eta$ whereas in figure 3.89 (b) for larger values of ${}^{m}\eta$ we observe decreasing magnitudes of ${}^{t}\overline{\Theta}_{z}$ with increasing ${}^{m}\eta$ due to the fact for larger values of ${}^{m}\eta$ major fraction of the work input get utilized in the near vicinity of the lid which reduces the energy transfer to the lower portion of the cavity and thus resulting in progressively reduced ${}^{t}\overline{\Theta}_{z}$ for increasing ${}^{m}\eta$. In figure 3.90 ${}^{t}\overline{\Theta}_{z}$ versus $\overline{x}$ at $\overline{y} = 0.5$ ${}^{t}\overline{\Theta}_{z}$ continues to decrease with increasing ${}^{m}\eta$ due to progressively lower activity in the cavity far below the lid.

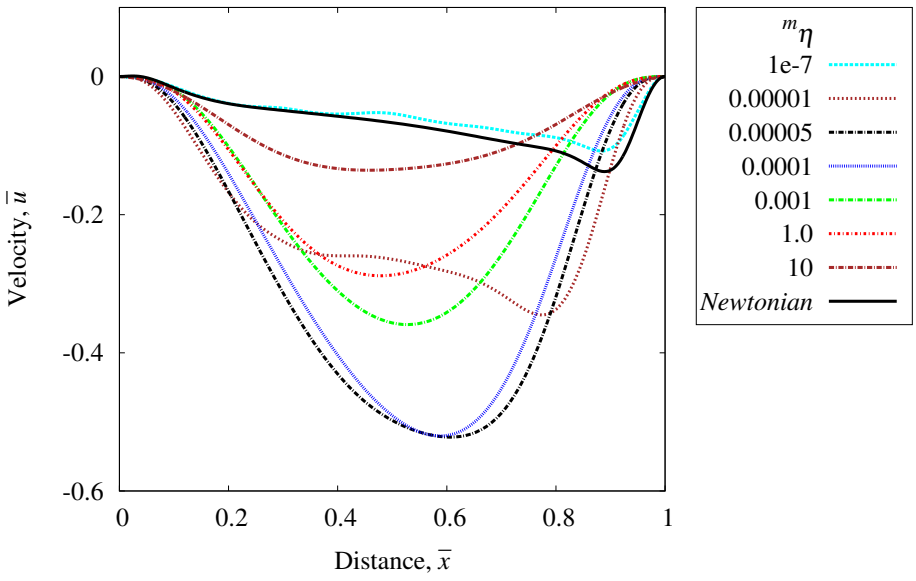

Figure 3.82: Velocity $\overline{u}$ versus distance $\overline{x}$ at $\overline{y} = 0.5$ of a square lid driven cavity

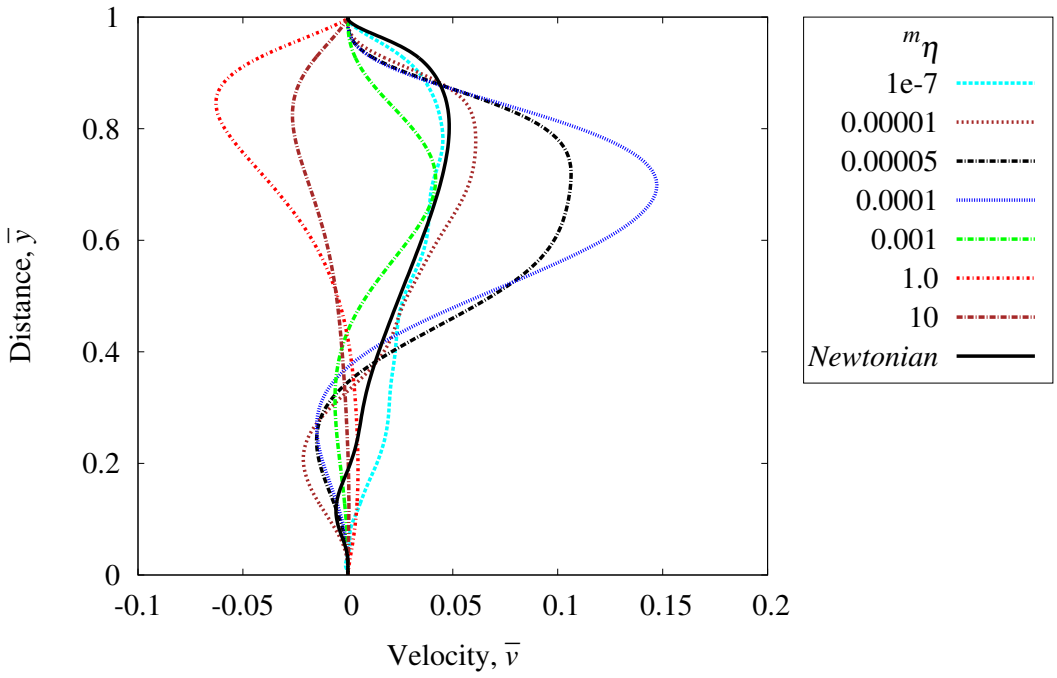

Figure 3.83: Velocity $\overline{v}$ versus distance $\overline{y}$ at $\overline{x} = 0.5$ of a square lid driven cavity

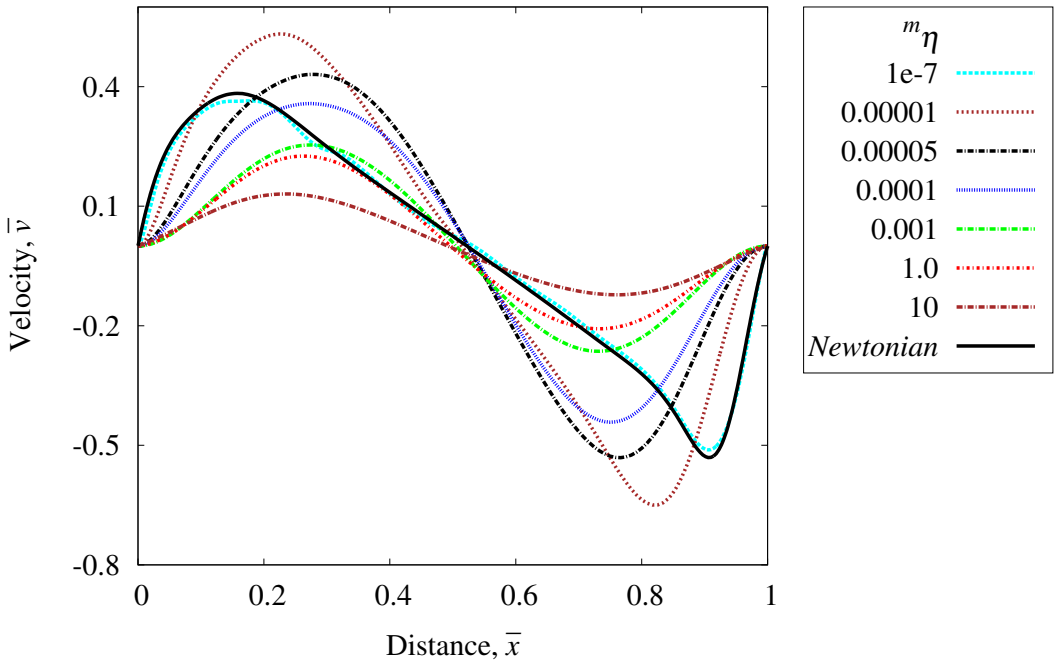

Figure 3.84: Velocity $\overline{v}$ versus distance $\overline{x}$ at $\overline{y} = 0.5$ of a square lid driven cavity

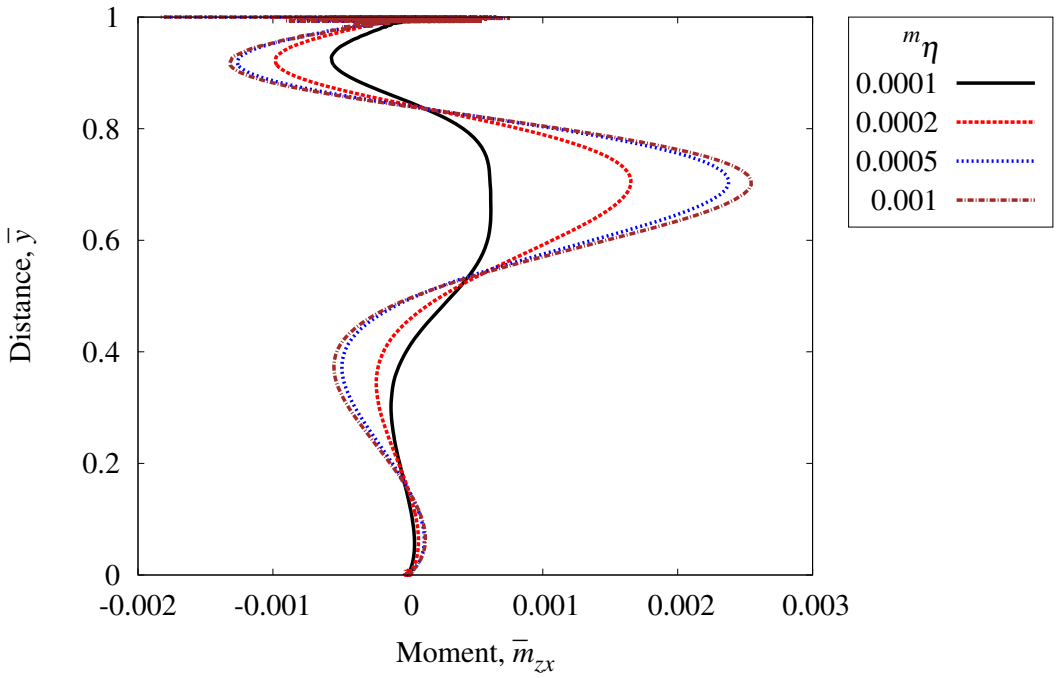

(a) Cauchy moment $\bar{m}_{zx}$, lower values of $^{m}\eta$

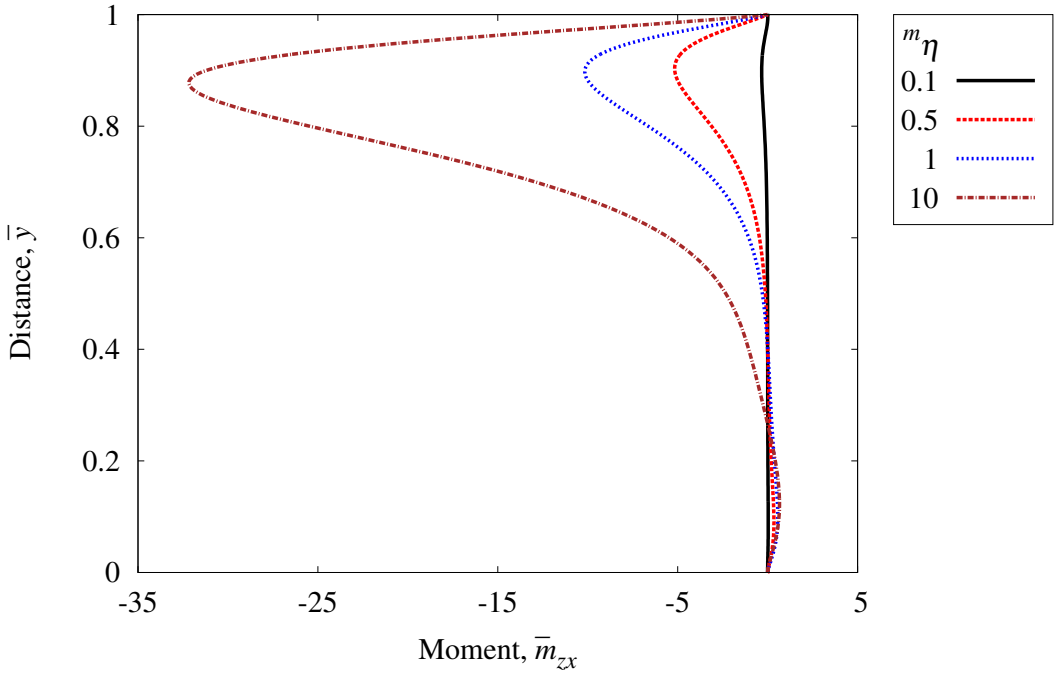

(b) Cauchy moment $\bar{m}_{zx}$, higher values of $^{m}\eta$

Figure 3.85: Cauchy moment $\bar{m}_{zx}$ versus distance $\bar{y}$ at $\bar{x} = 0.5$ of a square lid driven cavity

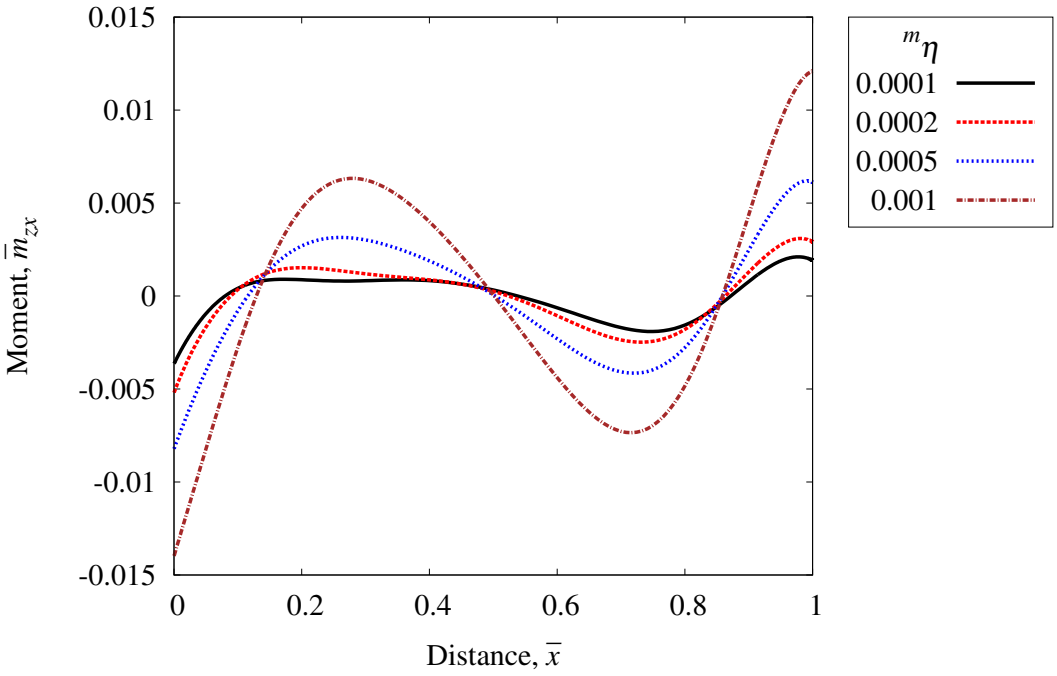

(a) Cauchy moment $\overline{m}_{zx}$, lower values of $^{m}\eta$

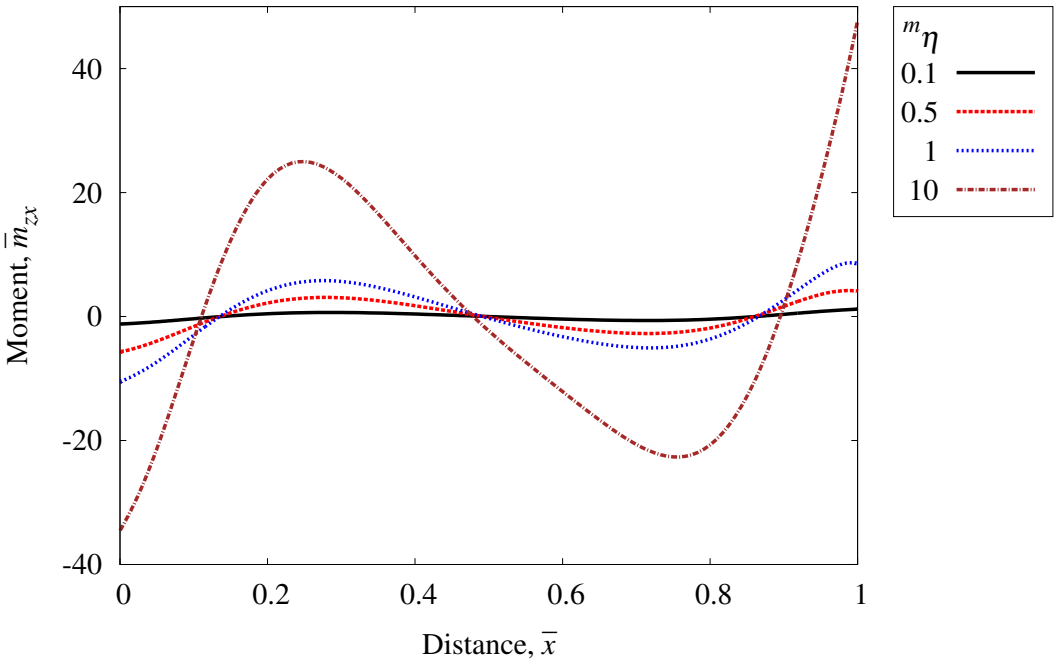

(b) Cauchy moment $\overline{m}_{zx}$, higher values of $^{m}\eta$

Figure 3.86: Cauchy moment $\overline{m}_{zx}$ versus distance $\overline{x}$ at $\overline{y} = 0.5$ of a square lid driven cavity

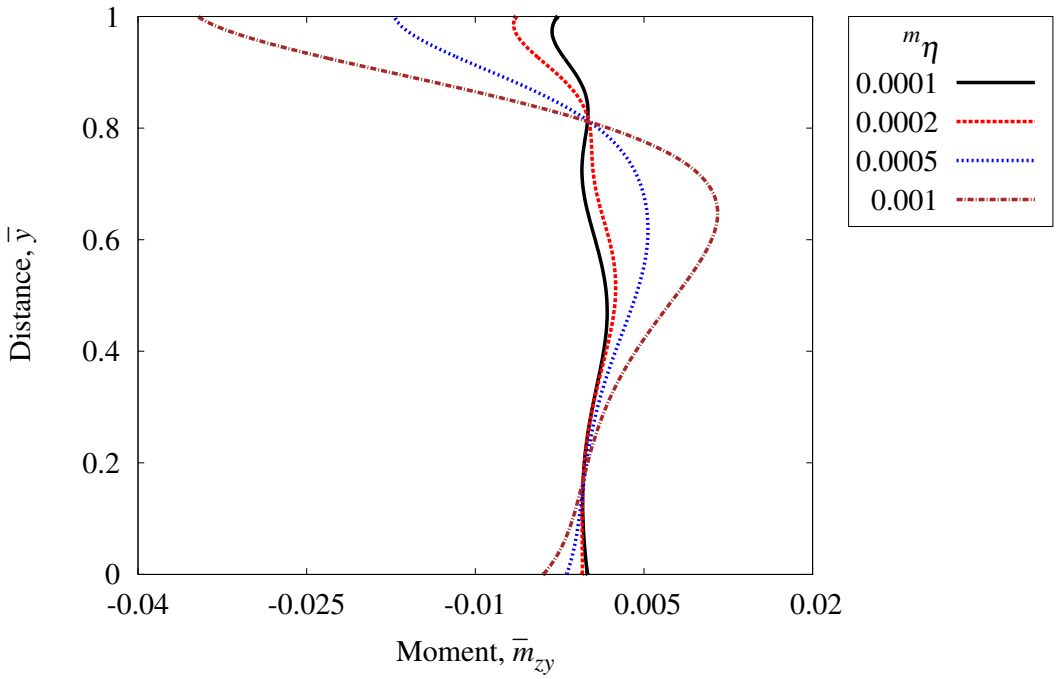

(a) Cauchy moment $\overline{m}_{zy}$, lower values of $^{m}\eta$

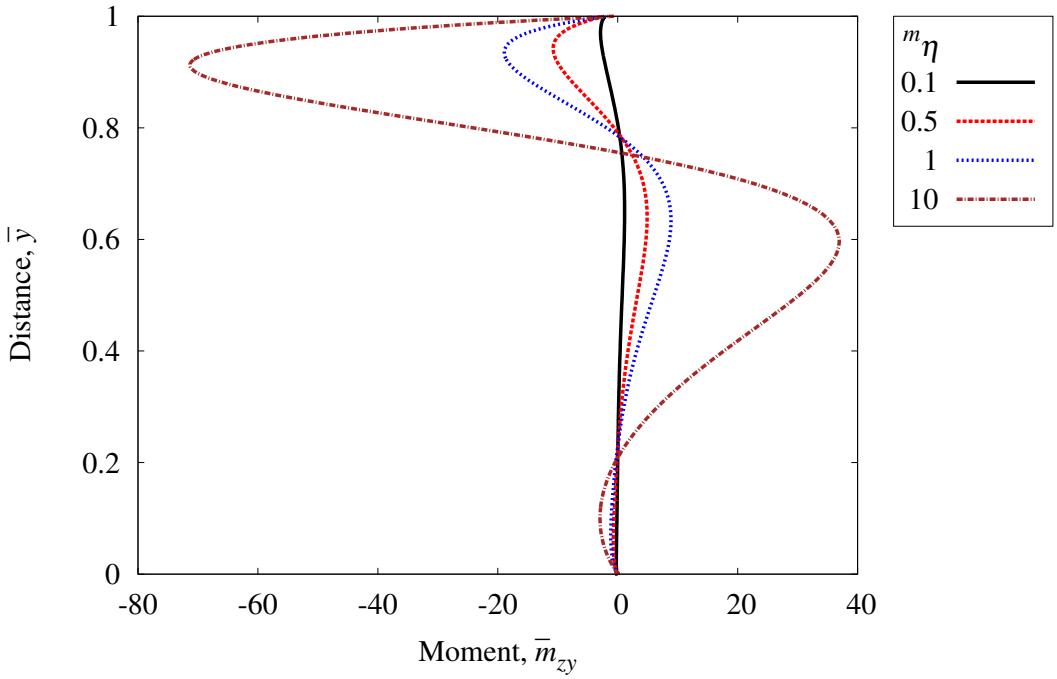

(b) Cauchy moment $\overline{m}_{zy}$, higher values of $^{m}\eta$

Figure 3.87: Cauchy moment $\overline{m}_{zy}$ versus distance $\overline{y}$ at $\overline{x} = 0.5$ of a square lid driven cavity

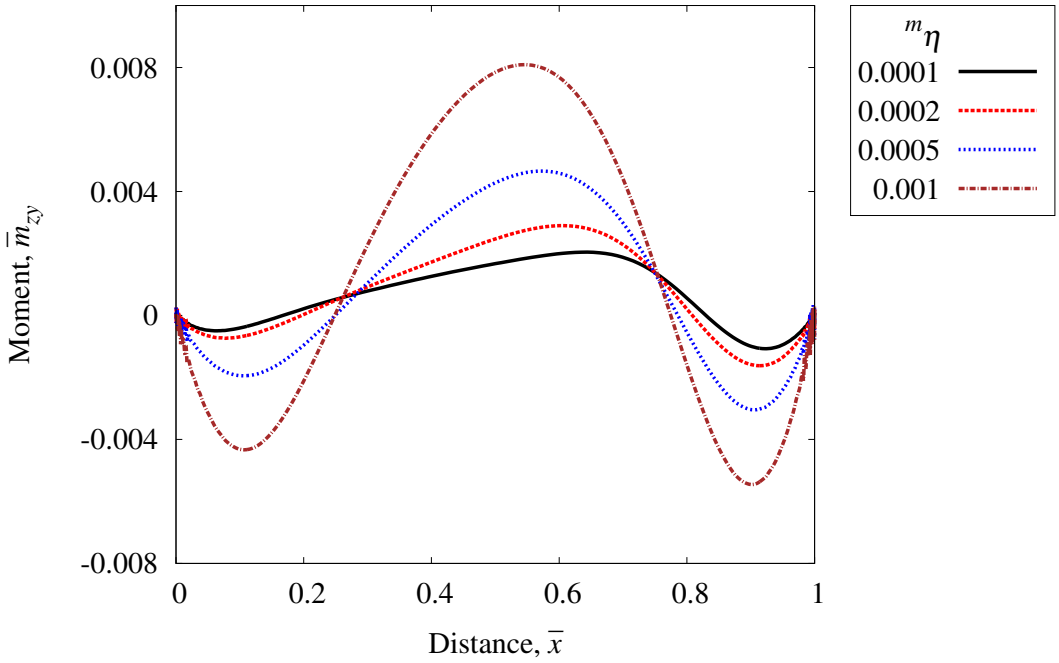

(a) Cauchy moment $\overline{m}_{zy}$, lower values of $^{m}\eta$

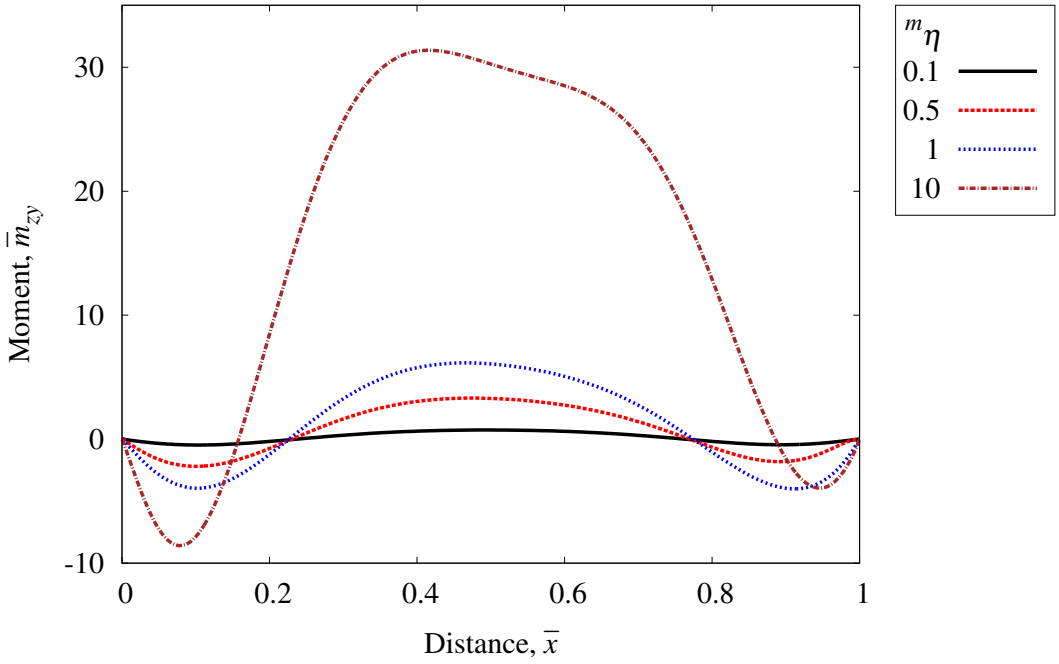

(b) Cauchy moment $\overline{m}_{zy}$, higher values of $^{m}\eta$

Figure 3.88: Cauchy moment $\overline{m}_{zy}$ versus distance $\overline{x}$ at $\overline{y} = 0.5$ of a square lid driven cavity

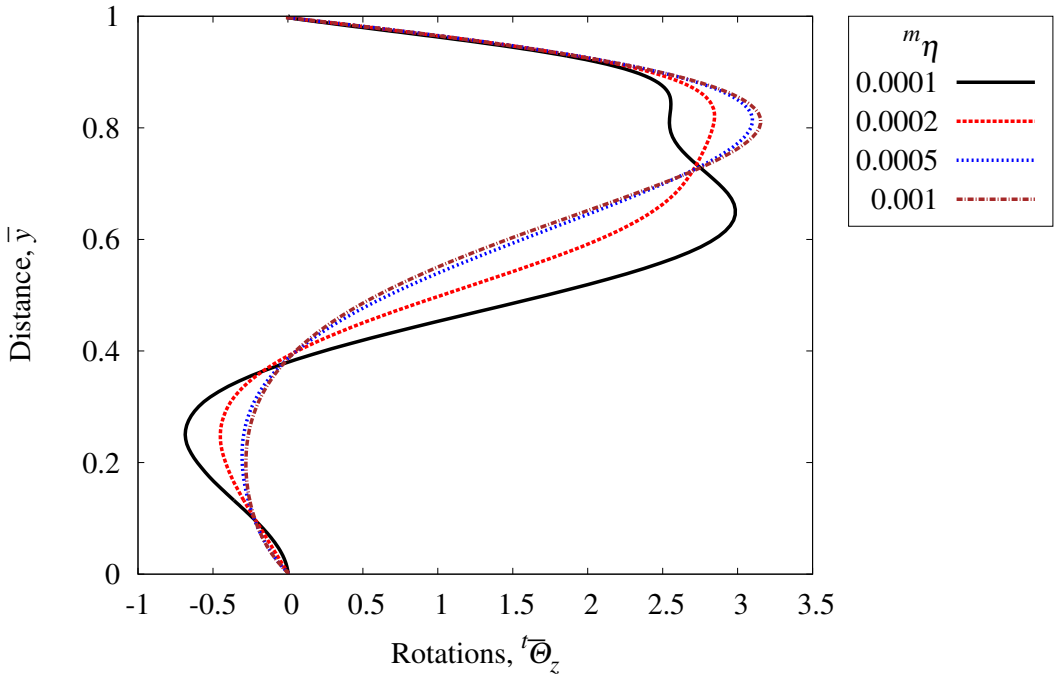

(a) Rotation rate ${}^{t}\overline{\Theta}_z$, lower values of ${}^{m}\eta$

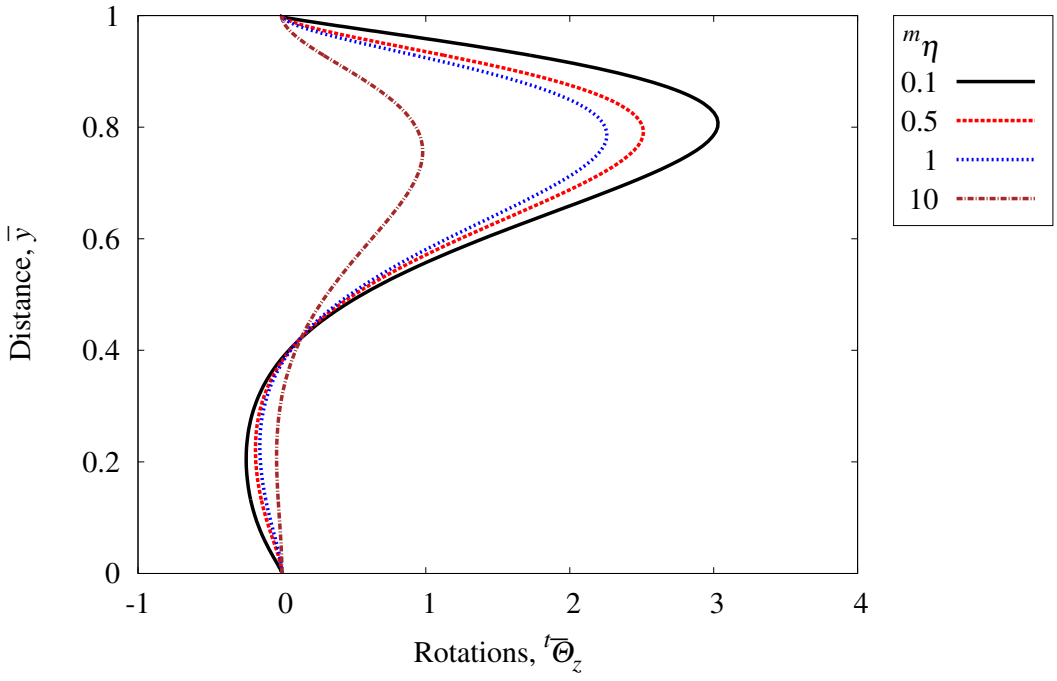

(b) Rotation rate ${}^{t}\overline{\Theta}_z$, higher values of ${}^{m}\eta$

Figure 3.89: Rotation rate ${}^{t}\overline{\Theta}_z$ versus distance $\overline{y}$ at $\overline{x} = 0.5$ of a square lid driven cavity

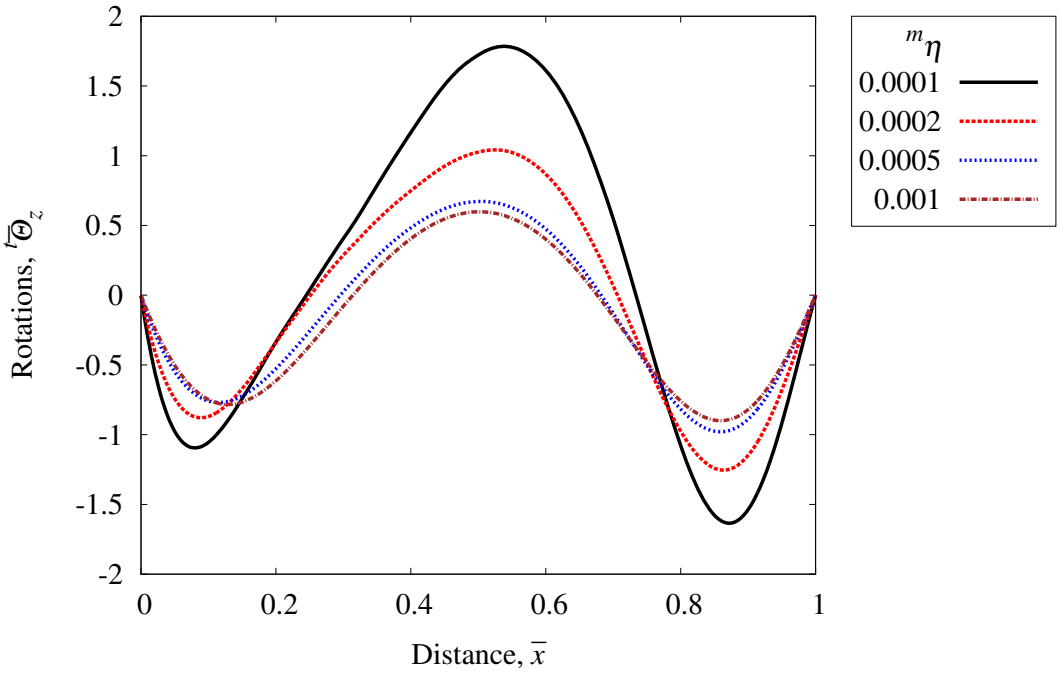

(a) Rotation rate ${}^{t}\overline{\Theta}_z$, lower values of ${}^{m}\eta$

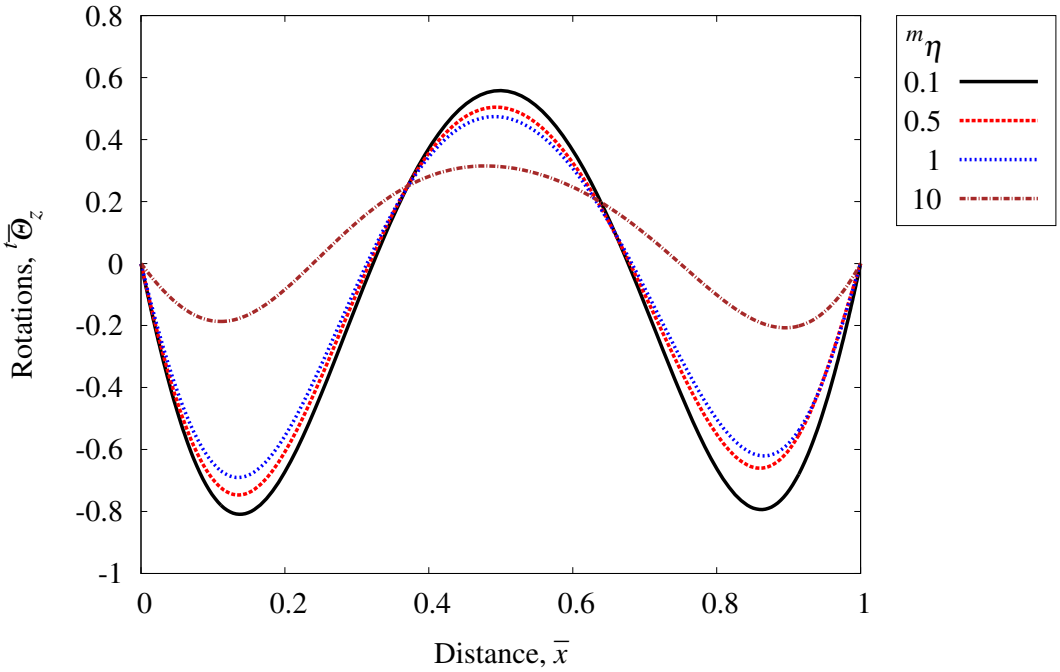

(b) Rotation rate ${}^{t}\overline{\Theta}_z$, higher values of ${}^{m}\eta$

Figure 3.90: Rotation rate ${}^{t}\overline{\Theta}_z$ versus distance $\overline{x}$ at $\overline{y} = 0.5$ of a square lid driven cavity

Figures 3.91 (a) - (f) show stream line contours for Newtonian and $^{m}\eta$ values 0.1, 0.5, 1, 10, and 50. Progressively increasing red zone with increasing $^{m}\eta$ indicates pronounced velocity values near the lid as opposed to virtually no red zone for $^{m}\eta = 0.1$. This of course reduces the energy available for lower portion of the cavity as $^{m}\eta$ increases. Progressively weaker circulation in the cavity is observed with increasing $^{m}\eta$.

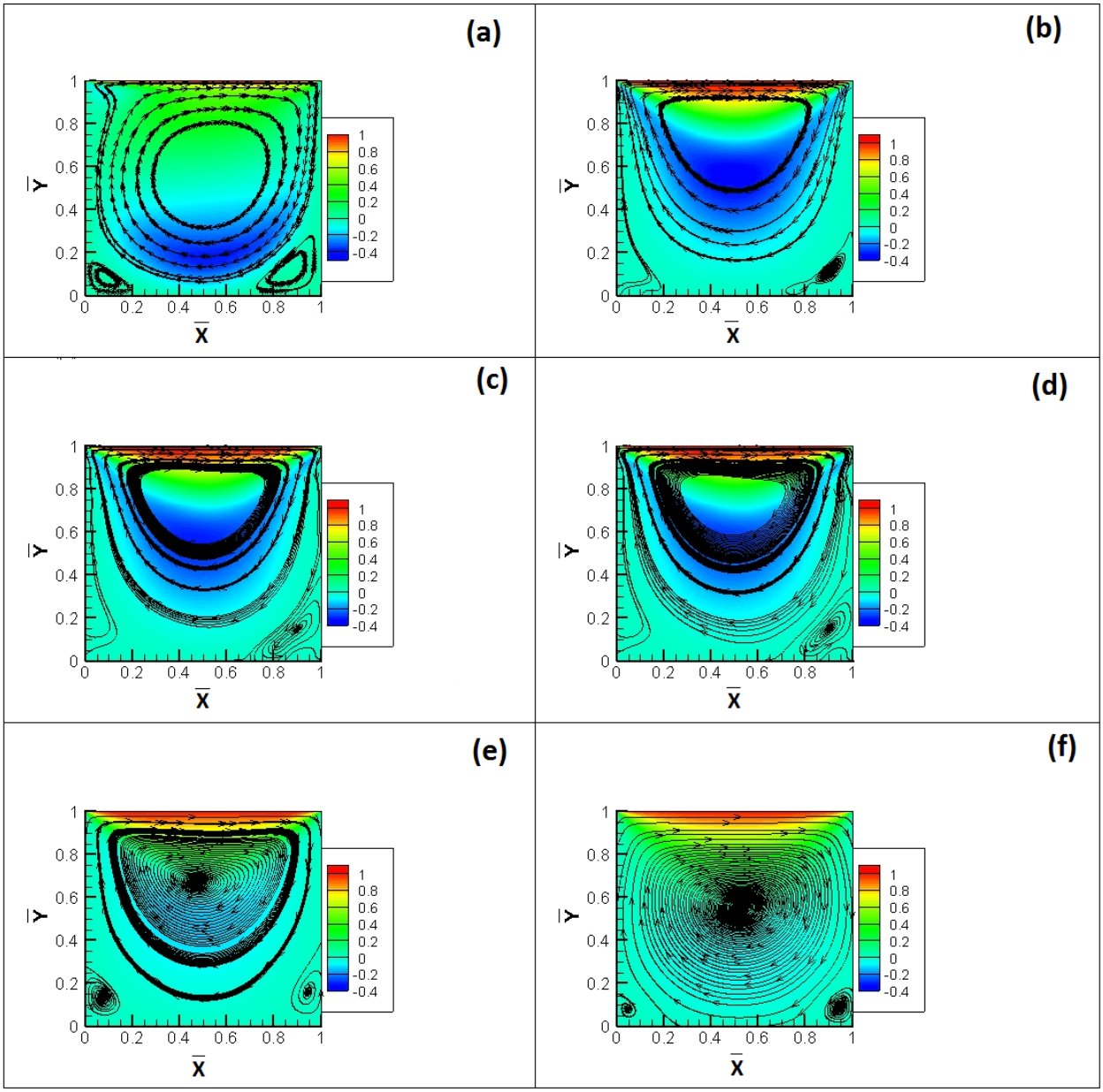

Figure 3.91: Streamline contours plot for (a) Newtonian, (b) $^{m}\eta = 0.1$, (c) $^{m}\eta = 0.5$, (d) $^{m}\eta = 1.0$, (e) $^{m}\eta = 10$, (f) $^{m}\eta = 50$ of a square lid driven cavity

3.4.2 Rectangular Cavity

In this study we consider a 1×2 rectangular cavity. Schematic of the cavity and the boundary conditions are shown in figures 3.92 (a) and (b). The cavity is discretized using 256 nine node p-version elements (figure 3.93) with $\overline{h}_d$ = 0.0025 (same as in case if square cavity). The p-level of 7 and k = 2 are used in the computations. These choices yield similar values of I as in case of square cavity.

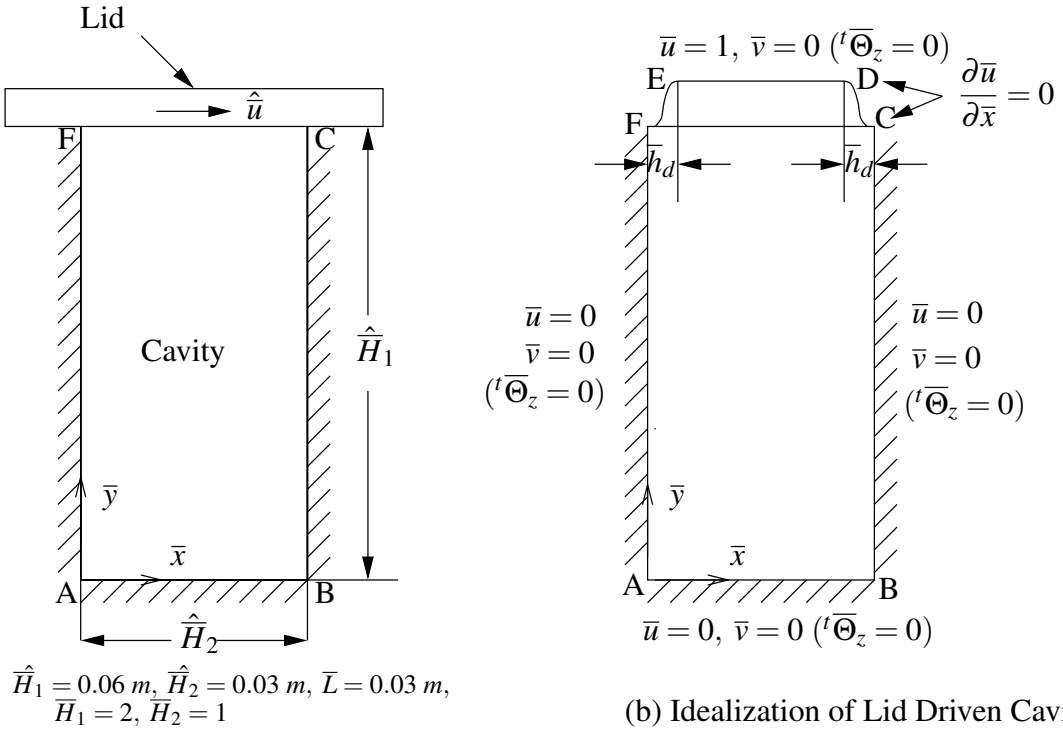

$\hat{\overline{H}}_1 = 0.06\ m,\ \hat{\overline{H}}_2 = 0.03\ m,\ \overline{L} = 0.03\ m,$
$\overline{H}_1 = 2,\ \overline{H}_2 = 1$

(a) Schematic of lid driven cavity

(b) Idealization of Lid Driven Cavity in (a), computational domain and boundary conditions

Figure 3.92: Schematic representation and computational domain of a rectangular lid driven cavity

Figure 3.94 shows plots of $\overline{u}$ versus $\overline{y}$ at $\overline{x}$ = 0.5. An expanded view of $\overline{u}$ versus $\overline{y}$ for $0 \leq \overline{y} \leq 1$ is shown in figure 3.95. Since the lower half of the cavity is relatively inactive specially for larger values of ${}^m\eta$, $\overline{u}$ values in figure 3.95 are an order of magnitude lower than those for $\overline{y}$ > 1.0 (figure 3.94). Plots of $\overline{u}$ versus $\overline{x}$ at $\overline{y}$ = 1.0 is shown in figure 3.96. Plots of $\overline{v}$ versus $\overline{y}$ at $\overline{x}$ = 0.5 and $\overline{v}$ versus $\overline{x}$ at $\overline{y}$ = 1.0 are shown in figures 3.97 and 3.98. For larger values of ${}^m\eta$, $\overline{v}$ is practically zero.

Side	Element Lengths						
$\overrightarrow{AF}$	0.005	0.01	0.02	0.04	0.08	0.16	0.32
	0.365	0.365	0.32	0.16	0.08	0.04	0.02
	0.01	0.005					
$\overrightarrow{AB}$	0.0025	0.005	0.01	0.02	0.04	0.08	0.16
	0.1825	0.1825	0.16	0.08	0.04	0.02	0.01
	0.005	0.0025					

Figure 3.93: 256 element discretization with $\overline{h}_d = 0.0025$ of a rectangular lid driven cavity

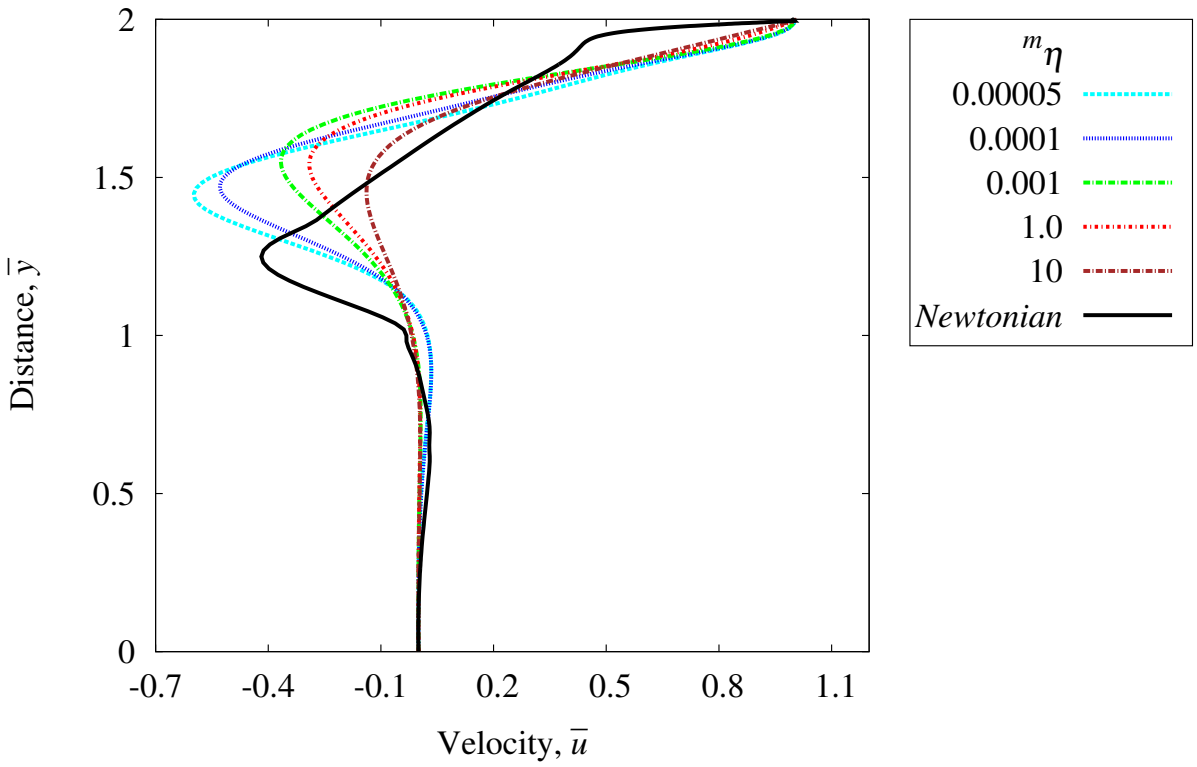

Figure 3.94: Velocity $\overline{u}$ versus distance $\overline{y}$ at $\overline{x} = 0.5$ of a rectangular lid driven cavity

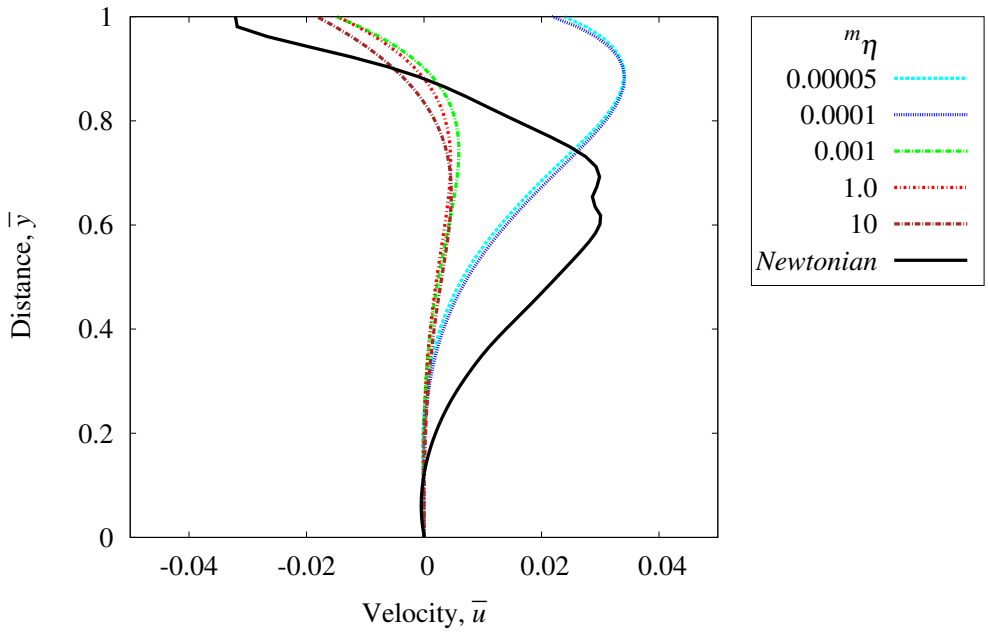

Figure 3.95: Expanded view of velocity $\overline{u}$ versus distance $\overline{y}$ at $\overline{x} = 0.5$ of a rectangular lid driven cavity

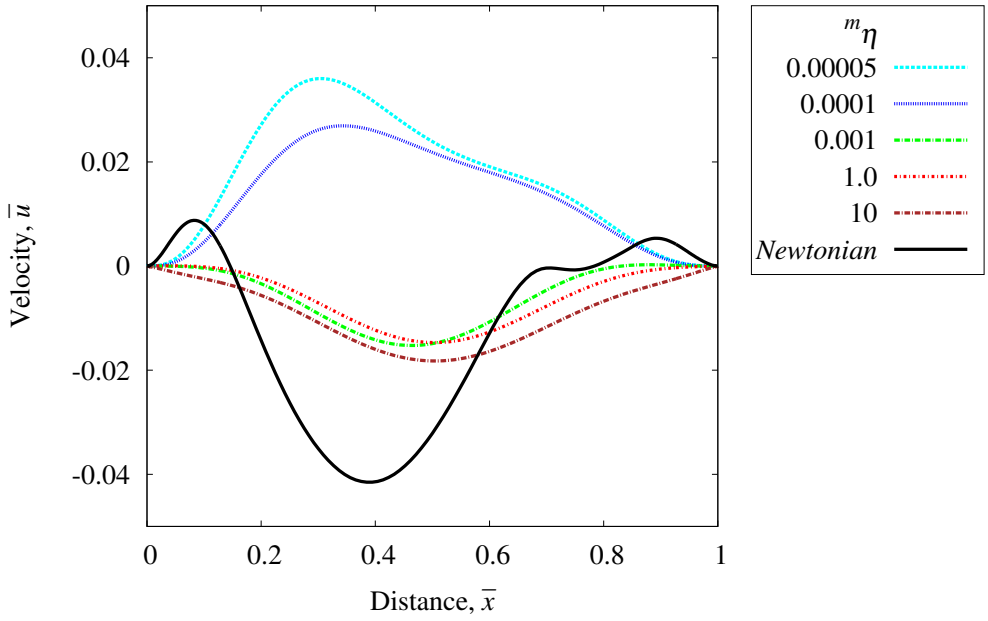

Figure 3.96: Velocity $\overline{u}$ versus distance $\overline{x}$ at $\overline{y} = 1.0$ of a rectangular lid driven cavity

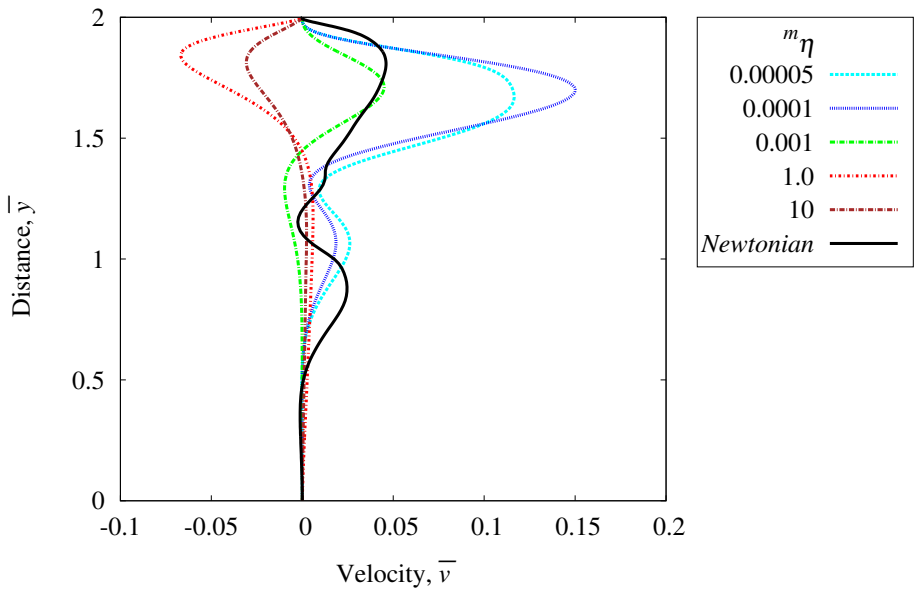

Figure 3.97: Velocity $\overline{v}$ versus distance $\overline{y}$ at $\overline{x} = 0.5$ of a rectangular lid driven cavity

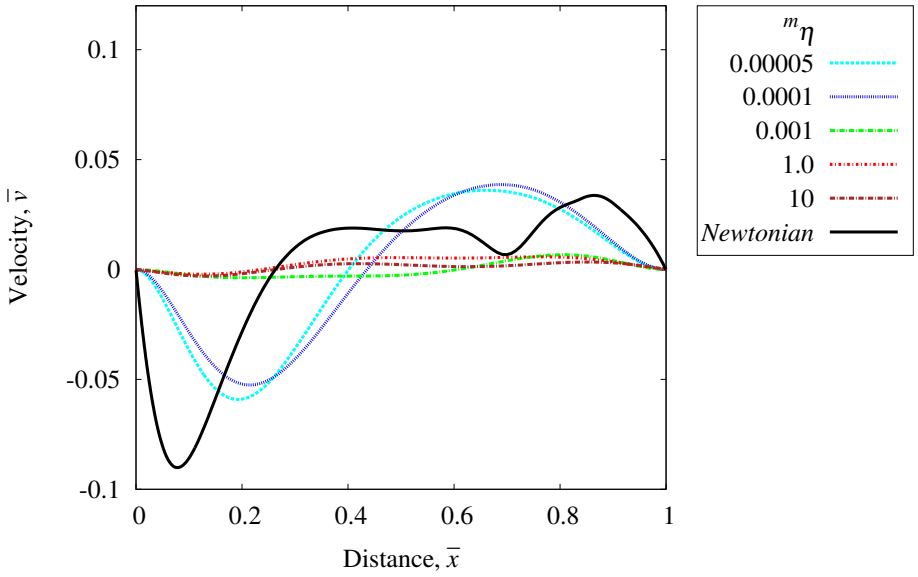

Figure 3.98: Velocity $\overline{v}$ versus distance $\overline{x}$ at $\overline{y} = 1.0$ of a rectangular lid driven cavity

Plots of $\overline{m}_{zx}$ versus $\overline{y}$ at $\overline{x} = 0.5$ in figure 3.99, $\overline{m}_{zy}$ versus $\overline{y}$ at $\overline{x} = 0.5$ in figure 3.100, ${}^{t}\overline{\Theta}_{z}$ versus $\overline{y}$ in figure 3.101 and an exploded view in figure 3.102, and ${}^{t}\overline{\Theta}_{z}$ versus $\overline{x}$ at $\overline{y} = 1.0$ in figure 3.103 all confirm: (1) Lower part of the cavity $0 \leq \overline{y} \leq 1$ becomes almost totally inactive for larger values

of ${}^{m}\eta$. Increased resistance to motion for increasing values of ${}^{m}\eta$ is quite clear from figures 3.99, 3.100, 3.101 and 3.102. Decreasing values of ${}^{t}\overline{\Theta}_{z}$ for increasing ${}^{m}\eta$ in figure 3.103 (at $\bar{y} = 1.0$) is due to progressively less active cavity in that region for larger values of ${}^{m}\eta$.

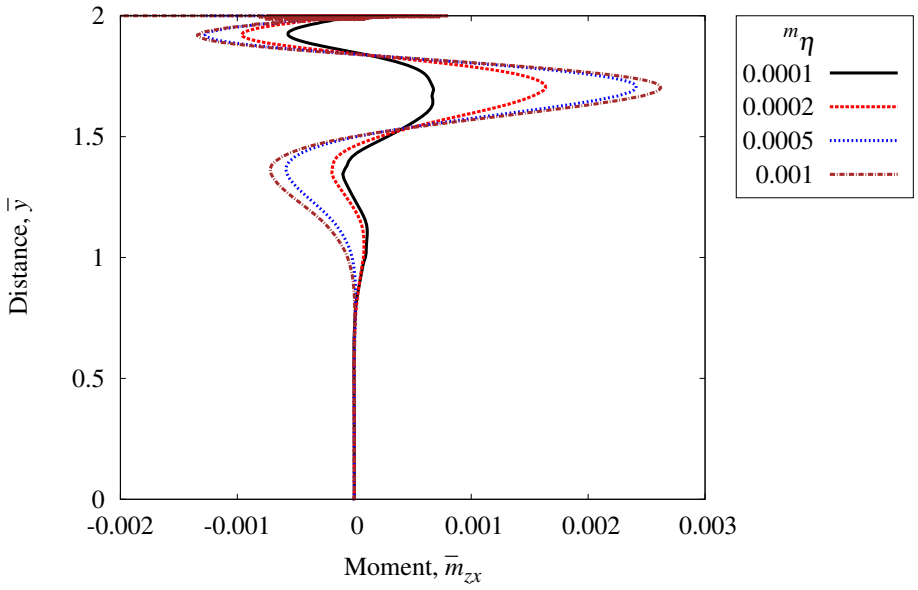

(a) Cauchy moment $\overline{m}_{zx}$, lower values of ${}^{m}\eta$

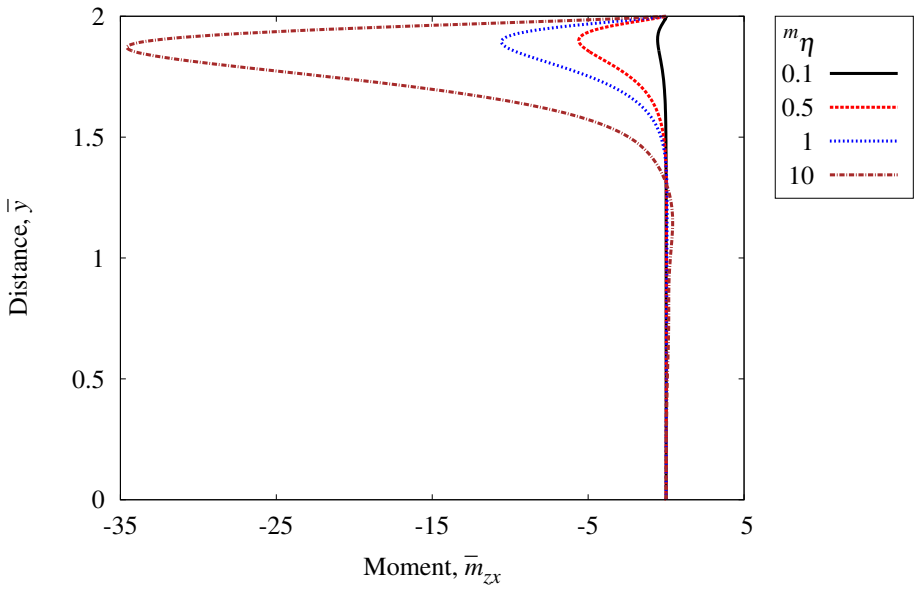

(b) Cauchy moment $\overline{m}_{zx}$, higher values of ${}^{m}\eta$

Figure 3.99: Cauchy moment $\overline{m}_{zx}$ versus distance $\bar{y}$ at $\bar{x} = 0.5$ of a rectangular lid driven cavity

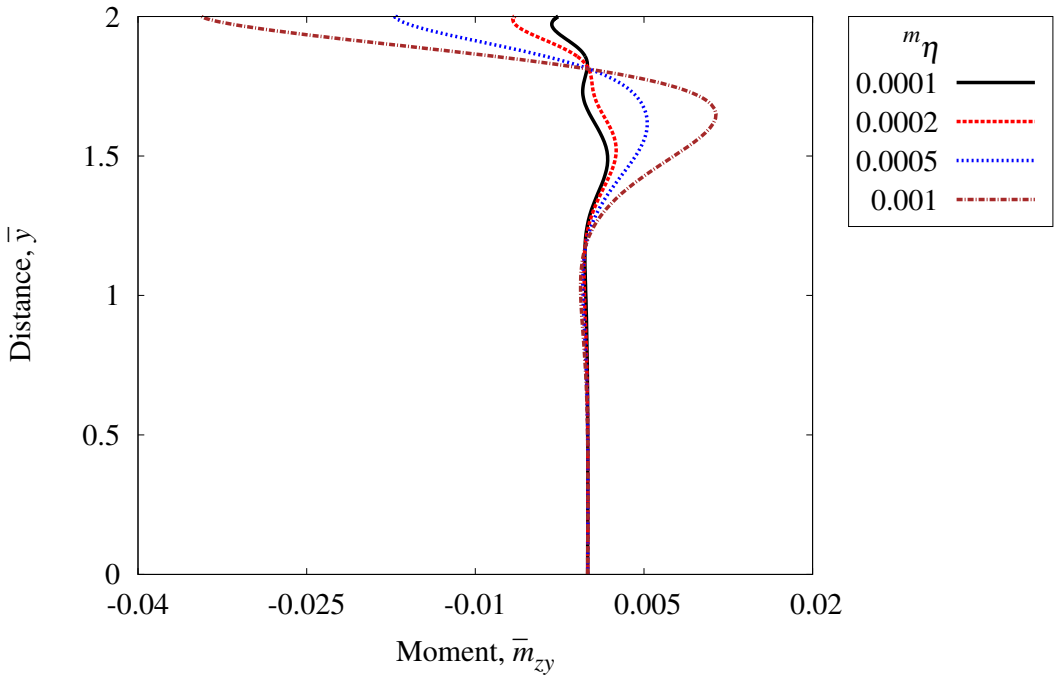

(a) Cauchy moment $\overline{m}_{zy}$, lower values of $^{m}\eta$

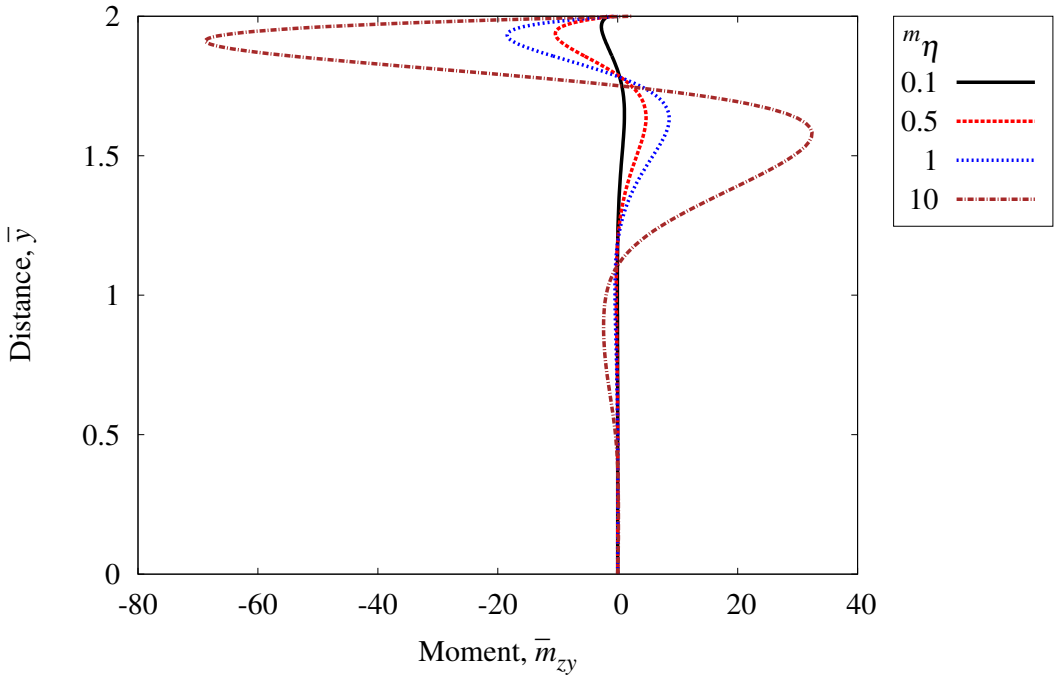

(b) Cauchy moment $\overline{m}_{zy}$, higher values of $^{m}\eta$

Figure 3.100: Cauchy moment $\overline{m}_{zy}$ versus distance $\overline{y}$ at $\overline{x} = 0.5$ of a rectangular lid driven cavity

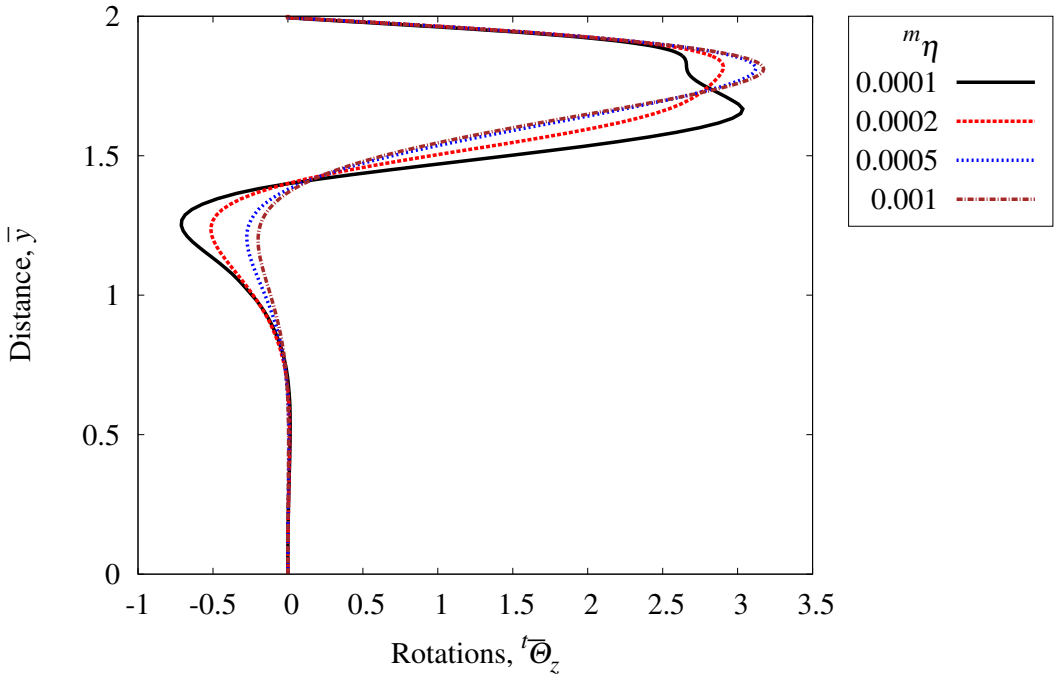

(a) Rotation rate ${}^{t}\overline{\Theta}_z$, lower values of ${}^{m}\eta$

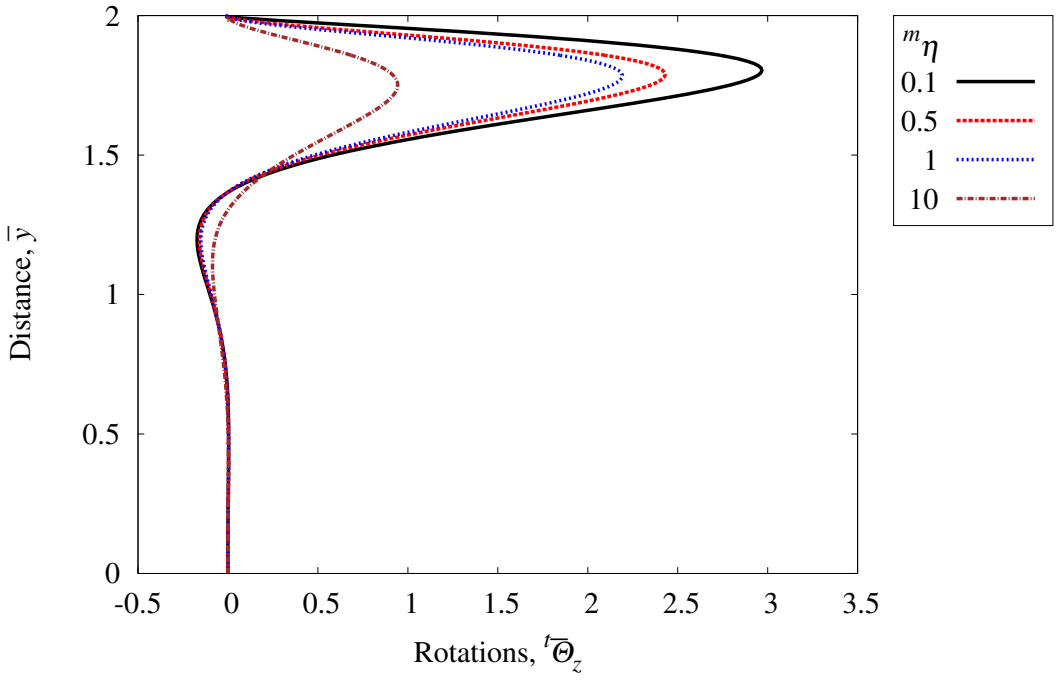

(b) Rotation rate ${}^{t}\overline{\Theta}_z$, higher values of ${}^{m}\eta$

Figure 3.101: Rotation rate ${}^{t}\overline{\Theta}_z$ versus distance $\overline{y}$ at $\overline{x} = 0.5$ of a rectangular lid driven cavity

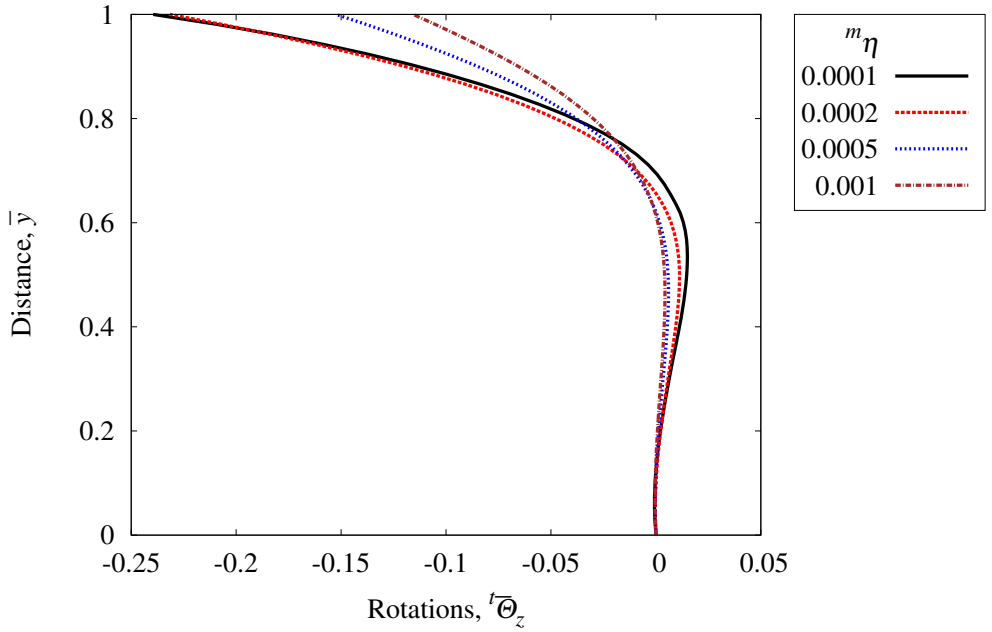

Figure 3.102: Exploded view of rotation rate ${}^{t}\overline{\Theta}_z$ versus distance $\overline{y}$ at $\overline{x}$ = 0.5 of a rectangular lid driven cavity

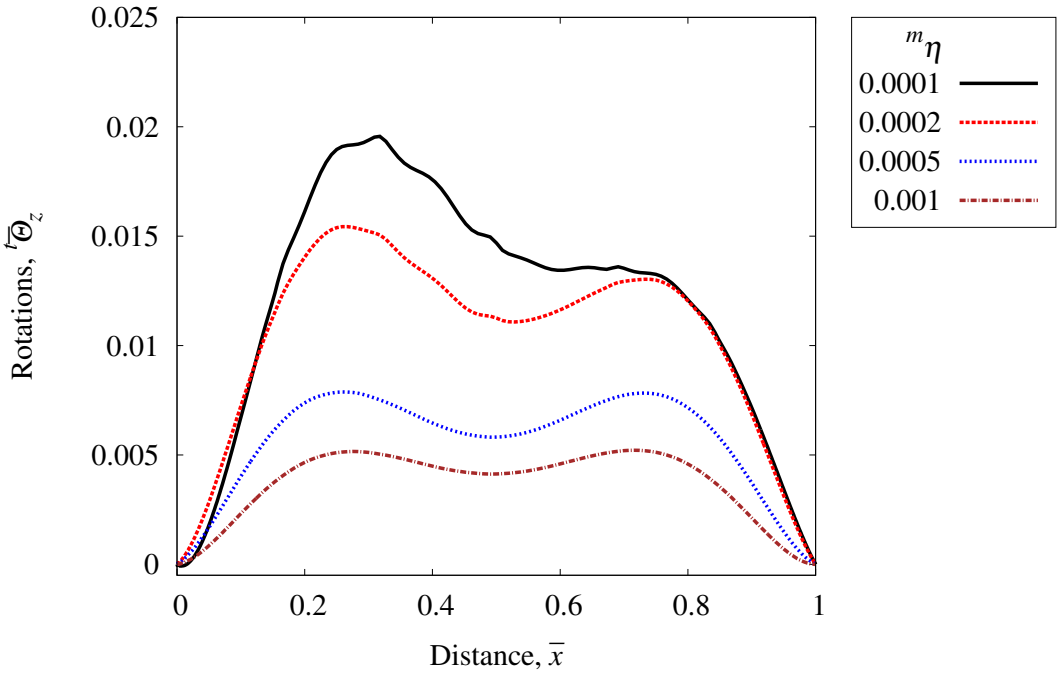

Figure 3.103: Rotation rate ${}^{t}\overline{\Theta}_z$ versus distance $\overline{x}$ at $\overline{y}$ = 1.0 of a rectangular lid driven cavity

Streamline contour plots are shown in figure 3.104. For progressively increasing ${}^{m}\eta$ progressively large fraction of applied work input is absorbed in the near vicinity of the lid, as a consequence the lower part of the cavity becomes progressively inactive. At ${}^{m}\eta = 10$ and 50 the portion of the cavity $0 \leq \bar{y} \leq 1$ is not active at all.

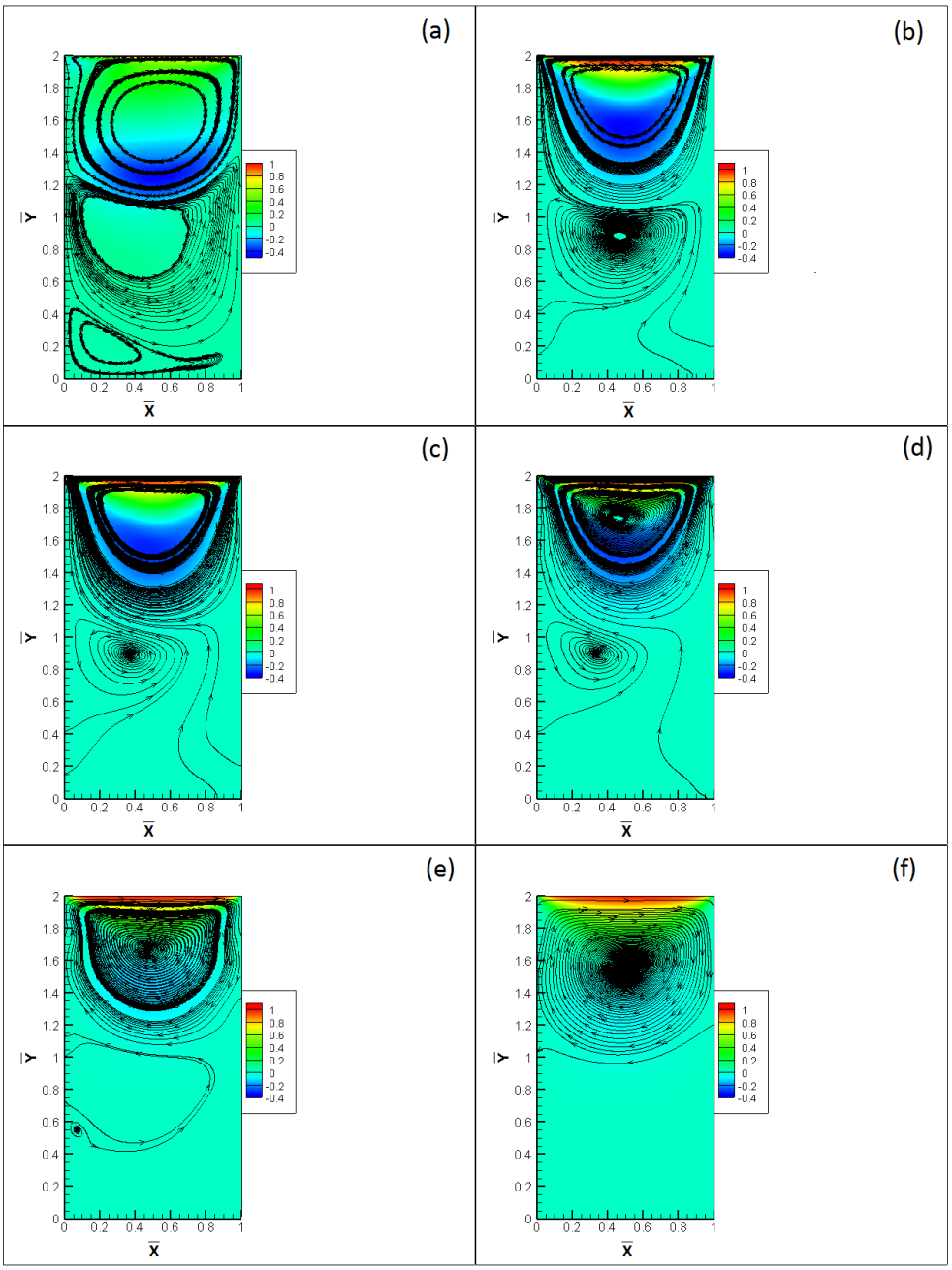

Figure 3.104: Streamline contours plot for (a) Newtonian, (b) ${}^{m}\eta = 0.1$, (c) ${}^{m}\eta = 0.5$, (d) ${}^{m}\eta = 1.0$, (e) ${}^{m}\eta = 10$, (f) ${}^{m}\eta = 50$ of a rectangular lid driven cavity

Chapter 4

Summary and Conclusions

In this thesis mathematical models based on internal polar non-classical continuum theory [1,2,8] are considered for isotropic, homogeneous incompressible viscous fluids to present numerical studies for three model problems : fully developed flow between parallel plates, asymmetric sudden expansion with expansion ratios of 2.75 : 2, 3 : 2 and 3.5 : 2, and square, rectangular lid driven cavities. Numerical solutions are also computed using mathematical models based on classical continuum theory and the results are compared with those obtained using internal polar non-classical models. In both cases, the numerical solution of the associated boundary value problems are calculated using p-version least squares finite element processes based on residual functional in which the local approximations are considered in higher order scalar product Hilbert spaces $H^{k,p}(\overline{\Omega}^e)$. Since the mathematical model consist of first order partial differential equations, for $k = 2$ the integrals in the entire computational processes remain Riemann over the discretization $\overline{\Omega}^T$. Computations are performed at $p = 7$ for lid driven cavity and at $p = 9$ for fully developed flow between parallel plates and asymmetric sudden expansion. In all studies residual functional I is of the order $0(10^{-6})$ indicating good accuracy of the computed solutions.

Numerical studies confirm that in the mathematical models based on internal polar non-classical theory the fluid offers additional resistance to the flow compared the mathematical models based on classical continuum theory. This resistance increases with increasing values of the material

coefficient ${}^m\eta$. A dramatic illustration is in the flow between parallel plates. We have shown that for a fixed pressure gradient, the flow rate decreases with progressively increasing values of ${}^m\eta$ and in fact eventually becomes zero. In this model problem for a chosen pressure gradient, there is a value of ${}^m\eta$ for which the flow rate will become zero. In case of lid driven cavity the sharp boundary layer at the lid disappears resulting in significant rate of work in the vicinity of the lid which eventually reduces the circulation strength below the lid. For 1×2 cavity, with progressively increasing values of ${}^m\eta$ the lower half of the cavity progressively becomes inactive.

In case of asymmetric expansion, for a fixed expansion ratio the recirculation zone reduces with increasing ${}^m\eta$. In case of $2.75 : 2$ expansion the recirculation region is almost nonexistent. All three model problems illustrate the influence of internal polar physics in terms of added resistance to the flow. In the model problems considered here the material coefficient ${}^m\eta$ is considered to be a fraction of η. Actual values of ${}^m\eta$ require calibration of the constitutive model using experiments.

Bibliography

[1] K.S. Surana, J.N. Reddy, and M. Powell. A polar continuum theory for fluent continua. *International J. of Engg. Research and Indu. Appls.*, 8(2):107–146, 2015.

[2] K.S. Surana, J.N. Reddy, and M. Powell. Ordered rate constitutive theories for internal polar thermofluids. *International J. of Math. Science & Engg. Appls.*, 9(3):51–116, 2015.

[3] K.S. Surana and J.N. Reddy. *Mathematics of computations and finite element method for boundary value problems*. Book manuscript in progress, 2016.

[4] Daniel Winterscheidt and Karan S Surana. p-version least-squares finite element formulation of burgers' equation. *International journal for numerical methods in engineering*, 36(21):3629–3646, 1993.

[5] Brent C Bell and Karan S Surana. p-version least squares finite element formulation for two-dimensional, incompressible, non-newtonian isothermal and non-isothermal fluid flow. *International journal for numerical methods in fluids*, 18(2):127–162, 1994.

[6] Nathan B Edgar and Karan S Surana. p-version least squares finite element formulation for axisymmetric incompressible non-newtonian fluid flow. *Computer methods in applied mechanics and engineering*, 113(3):271–300, 1994.

[7] Karan S Surana. *Advanced mechanics of continua*. CRC Press, 2016.

[8] K.S. Surana, J.N. Reddy, D. Nunez, and M. Powell. A polar continuum theory for solid continua. *International J. of Engg. Research and Indu. Appls.*, 8(2):77–106, 2015.

[9] J. N. Reddy. *An Introduction to the Finite Element Method*. 3rd ed., McGraw-Hill, New York, 2006.

[10] Richard H Pletcher, John C Tannehill, and Dale Anderson. *Computational fluid mechanics and heat transfer*. CRC Press, 2012.

[11] Thomas J R Hughes, Leopoldo P. Franca, and Gregory M. Hulbert. A new finite element formulation for computational fluid dynamics: Viii. the galerkin/least-squares method for advective-diffusive equations. *Computer Methods in Applied Mechanics and Engineering*, 73(2):173–189, 1989.

[12] Karan S Surana, Ali R Ahmadi, and JN Reddy. The k-version of finite element method for self-adjoint operators in bvp. *International Journal of Computational Engineering Science*, 3(02):155–218, 2002.

[13] Karan S Surana, Ali R Ahmadi, and JN Reddy. The k-version of finite element method for non-self-adjoint operators in bvp. *International journal of computational engineering science*, 4(04):737–812, 2003.

[14] Karan S Surana, Ali R Ahmadi, and JN Reddy. The k-version of finite element method for nonlinear operators in bvp. *International journal of computational engineering science*, 5(01):133–207, 2004.

[15] Daniel Winterscheidt and Karan S Surana. p-version least squares finite element formulation for two-dimensional, incompressible fluid flow. *International journal for numerical methods in fluids*, 18(1):43–69, 1994.

[16] Brent C Bell and Karan S Surana. A space–time coupled p-version least-squares finite element formulation for unsteady fluid dynamics problems. *International journal for numerical methods in engineering*, 37(20):3545–3569, 1994.

[17] Brent C Bell and Karan S Surana. A space-time coupled p-version least squares finite element formulation for unsteady two-dimensional navier–stokes equations. *International journal for numerical methods in engineering*, 39(15):2593–2618, 1996.

[18] UKNG Ghia, Kirti N Ghia, and CT Shin. High-re solutions for incompressible flow using the navier-stokes equations and a multigrid method. *Journal of computational physics*, 48(3):387–411, 1982.